AFRL-VS-TR-2001-1578

VALIDATION REPORT FOR THE CELESTIAL BACKGROUND SCENE DESCRIPTOR (CBSD) ZODIACAL EMISSION MODEL CBZODY6

Dr. Paul V. Noah
Ms. Meg A. Noah

Mission Research Corporation
589 West Hollis Street, Suite 201
Nashua, NH 03062-1323

February 2001

Scientific Report No. 8

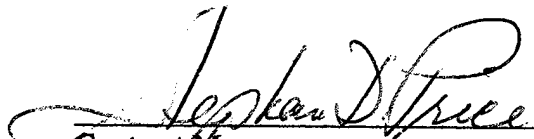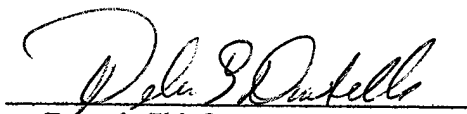**AIR FORCE RESEARCH LABORATORY**
Space Vehicles Directorate
29 Randolph Rd
AIR FORCE MATERIEL COMMAND
Hanscom AFB, MA 01731-3010

20031126 110

This technical report has been reviewed and is approved for publication.

Signature   _Signature_

Contract Manager   Branch Chief

REPORT DOCUMENTATION PAGE	*Form Approved*
	OMB NO. 0704.0188

Public reporting burden for this collection of information is estimated to average 1 hour per response, including the time for reviewing instructions, searching existing data sources, gathering and maintaining the data needed, and completing and reviewing the collection of information. Send comments regarding this burden estimate or any other aspect of the collection of information, including suggestions for reducing this burden, to Washington Headquarters Services, Directorate for Information Operations and Reports, 1215 Jefferson Davis Highway, suite 1204, Arlington, VA 22202-4302, and to the Office of Management and Budget, Paperwork Reduction Project (0704-0188), Washington, DC 20503.

1. AGENCY USE ONLY *(Leave Blank)*	2. REPORT DATE February 2001	3. REPORT TYPE AND DATES COVERED Scientific, Interim, 1 Apr 99 – 31 Mar 2000

4. TITLE AND SUBTITLE	5. FUNDING NUMBERS
Validation Report for the Celestial Background Scene Descriptor (CBSD) Zodiacal Emission Model CBZODY6	Contract: F19628-93-C-0028 PE: 63215C
6. AUTHOR(s) Paul Noah Meg Noah Mission Research Corp. – Nashua, NH 03062	PR: S321 TA: GG WU: AA

7. PERFORMING ORGANIZATION NAME(S) AND ADDRESS(ES)	8. PERFORMING ORGANIZATION REPORT NUMBER
Mission Research Corporation P.O. Drawer 719 Santa Barbara, CA 93102-0719	

9. SPONSORING/MONITORING AGENCY NAME(S) AND ADDRESS(ES)	10. SPONSORING/MONITORING AGENCY REPORT NUMBER
Air Force Research Laboratory 29 Randolph Road Hanscom AFB, MA 01731 Contract Manager: Dr. Steven Price	AFRL/VS-TR-2001-1578

11. SUPPLEMENTARY NOTES

12a. DISTRIBUTION/AVAILABILITY STATEMENT	12b. DISTRIBUTION CODE
Approved for public release; distribution unlimited.	

ABSTRACT *(Maximum 200 words)*

This report provides detailed information on the evolving improvements and verification of the AFRL/HRS Celestial Background Scene Descriptor (CBSD) Zodiacal Emission code (CBZODY). The CBZODY model predicts the flux from the solar system dust cloud for a given line-of-sight or field-of-view that would be detected by optical and infrared sensor systems. CBZODY is currently in use by the MDA as a component of the SSGM simulation package and as part of the AFRL PLEXUS R3V2 atmospheric effects modeling suite.

14. SUBJECT TERMS			15. NUMBER OF PAGES 84
Celestial, Infrared, Visible, Modeling, Zodiacal			16. PRICE CODE

17. SECURITY CLASSIFICATION OF REPORT UNCLASSIFIED	18. SECURITY CLASSIFICATION OF THIS PAGE UNCLASSIFIED	19. SECURITY CLASSIFICATION OF ABSTRACT UNCLASSIFIED	20. LIMITATION OF ABSTRACT None

Standard Form 298 (Rev. 2-89)
Prescribed by ANSI Std. 239-18
298-102

TABLE OF CONTENTS

LIST OF FIGURES

LIST OF TABLES

1. CBZODY6 Validation Summary

1.1 Introduction

This report provides detailed information on the evolving improvements and verification of the AFRL Celestial Background Scene Descriptor (CBSD) Zodiacal Emission code (CBZODY).

The CBZODY model predicts the flux from the solar system dust cloud for a given line-of-sight or field-of-view that would be detected by optical and infrared sensor systems. CBZODY is currently in use by the MDA as a component of the SSGM simulation package and as part of the AFRL PLEXUS R3V2 atmospheric effects modeling suite.

The intent of the report is to document the quality and fidelity of this component in its application to the design, simulation, and operation of MDA electro-optic sensors having to discriminate targets against zodiacal light and dust band emission sources. This report provides insight into the goodness of the CBZODY model relative to actual observations of the zodiacal background light/emission sources. This report captures the base-line that should ensure system, designers, developers, and operators that CBZODY gives fast, reliable, and realistic representation of the effects of Zodiacal emission sources on E-O systems.

1.1.1 Goals of the CBZODY Program

The CBSD CBZODY program has the stated goal of reproducing the zodiacal contribution to the celestial background with both a high spectral and spatial fidelity. Spectrally the code must have what we call "dial-a-wavelength" capability over a range of 0.2 to $35\mu m$. This means that the code accepts any spectral filter function in that range. The CBZODY code, by use of the external volume emissivity database, can produce high spectral resolution spectra from 0.2 to $30\mu m$ at $0.01\mu m$ resolution. It can also reach $300\mu m$ with a spectral resolution of $0.1\mu m$.

More importantly, the dial-a-wavelength capability requires the code to be predictive. It does not merely mimic the best-fit results of a certain instrument database.

The second goal is to allow model simulations down to the 2 arc-second level. The CBZODY model is capable of producing such simulations. We do caution however that we can not quote an accuracy for this level of observations. The primary reason is that there are no large-scale observations of zodiacal light at a 2 arc-second resolution. This is inherently difficult because of the nature of the zodiacal emission. The zodiacal light is an all-sky phenomenon. The observed brightness in a sensor IFOV is dependent on the IFOV of the sensing element, i.e. the pixel size. The surface brightness of the zodiacal emission is much lower by orders of magnitude than the surface brightness of any star. However, unlike stars, which are mere points, the zodiacal emission completely fills the IFOV. Larger pixels means that more area is sampled and the total, or integrated brightness, can exceed not merely stars but the plane of the galaxy itself.

1.1.2 About Zodiacal Light.

The solar system, or zodiacal, dust cloud, is seen in thermal emission from 4μm to $35+\mu$m and by scattered sunlight at $\lambda < 4\mu$m. This background has two large-scale components: a broad component whose brightness fills the sky around the Earth; and a narrower band structure confined to within a few tens of degrees of the ecliptic plane (Sykes 1988, 1990). It is theorized that a toroidal dust cloud, composed of debris from asteroid collisions and comets, encircles the Sun (Dermott et al., 1984). The Earth is located inside this cloud and hence the cloud is visible over the entire sky.

The band structure, discovered by IRAS (Low et al. 1984, Hauser et al. 1984), consists of several pairs of faint bands of emission close to the plane of the ecliptic associated with the remnants of the breakup of individual asteroid families (Sykes et al., 1989, Dermott et al. 1985, 1986). The CBSD zodiacal light model, CBZODY, models both the broad and band contributions, including thermal emission and scattered light, and is capable of producing spectra, line-of-sight radiance, and two-dimensional images.

Over the course of its development, CBZODY has been continuously improved through the comparison of the model to observational data of the zodiacal emissions by some of the premier DoD and astronomical research community research programs. Along with improvements to the realism of its simulated results, CBZODY has also been improved with regard to computational speed, thus making it a candidate for application in complex wargaming and operations research simulations for ballistic missile defense.

1.2 CBZODY: A Zodiacal Light Model.

We have developed a detailed model of the zodiacal emission. The code is called CBZODY6 and was developed for the Air Force's CBSD program whose goal is to provide realistic simulations of the celestial sphere to be used in sensor simulation and development. Following the method of Leinert (1975), the zodiacal dust cloud is separated into two components, a radial dust density function and a latitudinal, or out-of-plane, dust density component. The cloud is assumed symmetric longitudinally (l), in the dust cloud symmetry plane, which is close to but not coincident with the ecliptic. Formally, the number density function is defined in heliocentric ecliptic coordinates as:

$$N(d,z) = f(d) \cdot f(z)$$

d = heliocentric distance, in-plane

z = out of plane vertical distance

The in-plane or radial function is simply:

$$f(d) = d^{-\nu}$$

On theoretical grounds, the power law index, ν, should be ≥ 1 (Briggs 1962). This is light drag due to the Poynting-Robertson effect. The model uses a Lorentzian-like function for the out-of-plane, latitudinal distribution (Clark et al. 1993) of the form:

$$f(z) = \left(\frac{\Gamma^2}{\Gamma^2 + z^2} \right)$$

2

where Γ is the half-width-at-half-maximum (HWHM) of the cloud, also known as the scale height measured in AU.

The Lorentzian function was used after studying the IRAS survey scan data. Figure 1 is a scan from the IRAS mission (solid line) plus a model run (dashed line) using a Lorentzian profile. There are three things to note about this image:

1. Between ecliptic latitudes of $-30°$ to $-60°$ there is a weak contribution to overall signal from the galaxy

2. Between $-20°$ and $20°$ there is an excess not modeled by the Lorentzian; these are the zodiacal bands first observed by IRAS in 1983 (Low et al. 1984, Hauser et al. 1984)

3. The Lorentzian produces an excellent fit to the remaining observed flux.

SOP 179 Obs 009
Band 1
Best Fit
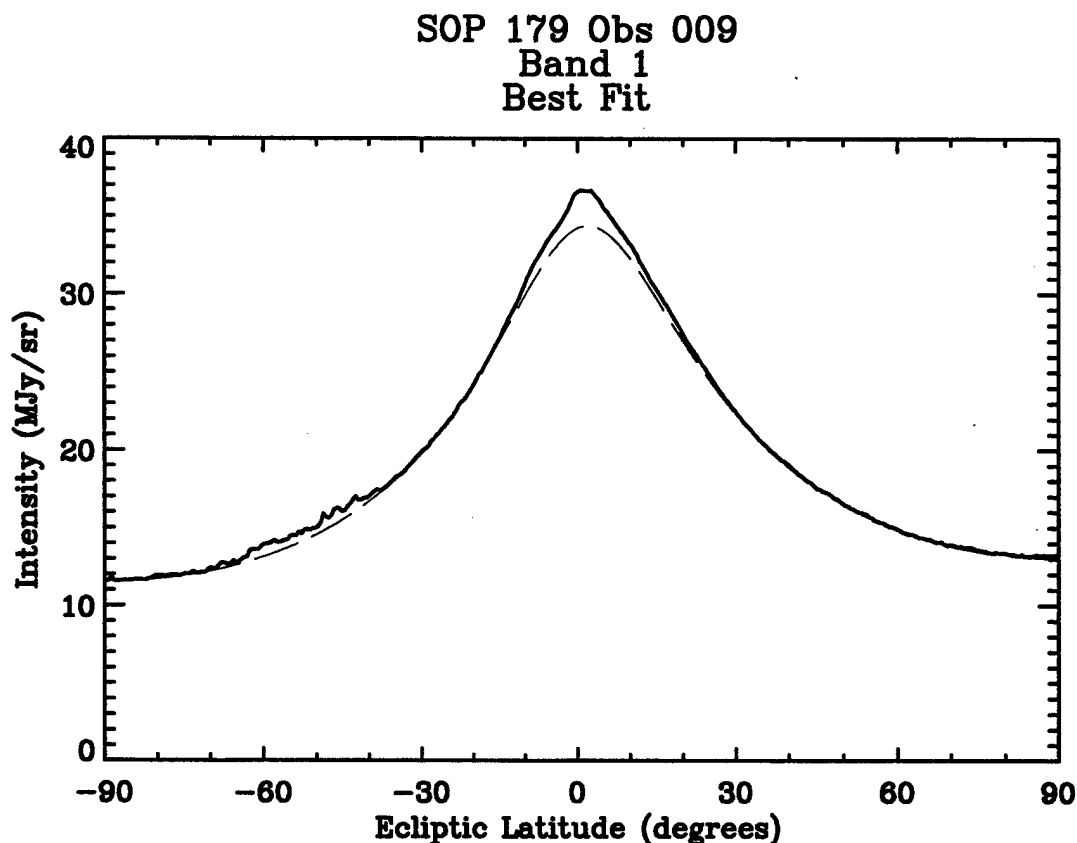
Figure 1: IRAS data and the Lorentzian fit. The IRAS data are presented as a solid line while the Lorentzian model is the dashed line. The match between the data and model is excellent once the galactic and band contributions are ignored.

1.3 Dust Composition and Volume Emissivity

The spatial modeling of the CBZODY model relies on the separation of variables and produces an in-plane, radial dust density distribution, and an out-of-plane, Lorentzian dust density; however, there is another equally important component that must be accounted for as an important factor in the spectral modeling of the Zodiacal light, namely the emissive properties of the dust material. This is accounted for by the volume emissivity.

The volume emissivity, ε_ν, is defined as the amount of energy that a unit volume of material emits per second per unit solid angle in the frequency range ν to $\nu + d\nu$ (Lang 1980, p. 27). The total intensity along a line of sight is:

$$I_\nu = \int_0^l \varepsilon_\nu \cdot e^{-\alpha_\nu x} dx$$

where:

l = the line of sight distance to the dust cloud outer limit, and

α_ν = the absorption coefficient per unit length.

The absorption coefficient can also be considered an extinction coefficient and is the combination of the amount of energy absorbed by the dust and the energy scattered out of the line of sight (Gray 1976, p. 106). For the zodiacal light calculations, the absorption is essentially zero and is taken to be identically zero. The volume emissivity of an ensemble of particles is calculated by integrating over the size distribution and summing over all constituents (Reach 1988):

$$\varepsilon_\nu = \sum_i \int da \frac{dn^{(i)}}{da} B_\nu(T^{(i)}(a)) Q_{abs}^{(i)}(a,\nu)$$

where the size distribution, $da \frac{dn^{(i)}}{da}$, is the number density of particles composed of material i with radius between a and $a+da$. The solution for the temperature T is found from the condition of radiative equilibrium

$$T = 278°K \left[\frac{\overline{Q}_{Sun}}{\overline{Q}(T)} \right]^{\frac{1}{4}} D^{-\frac{1}{2}}$$

where $\overline{Q}_{Sun}$ is the absorption efficiency averaged over the solar spectrum, $\overline{Q}(T)$ is the absorption efficiency averaged over a blackbody spectrum at temperature T, and D is the distance of the grain from the Sun in AU. The solution for the temperature is usually done by iteration. The absorption efficiency, Q_{abs}, is defined such that the cross section for absorption of a photon of wavelength λ by a spherical particle of radius a is $\pi a^2 Q_{abs}^{(i)}(a,\lambda)$. The solution for Q_{abs} is based on Mie theory (Van de Hulst 1957, Kerker 1969, and Bohren and Huffman 1983).

The model of Reach (1988) has a variety of materials that can be used. The volume emissivity used in CBZODY consists of mixtures of astronomical silicates and graphite. Figure

2 gives the temperature distribution for astronomical silicate as a function of particle size for 3 distances from the Sun: 0.05 AU; 1.00 AU; and 3.30 AU.

The volume emissivity used in CBZODY6 is a mixture of 65% astronomical silicate and 35% graphite and is in a pre-computed external file. Figure 3 gives the volume emissivity spectra used in CBZODY for three heliocentric distances, 0.05 AU, 1.00 AU, and 3.30 AU. The peak shifts to longer wavelength for increased distance following the temperature profile.
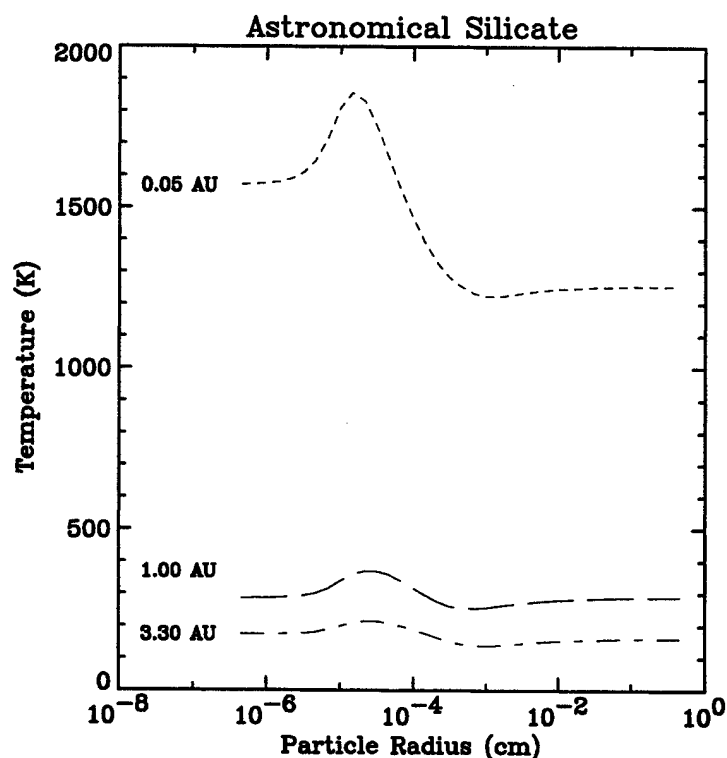
Figure 2: Temperature profiles for astronomical silicate at three different distances from the Sun as a function of particle size.
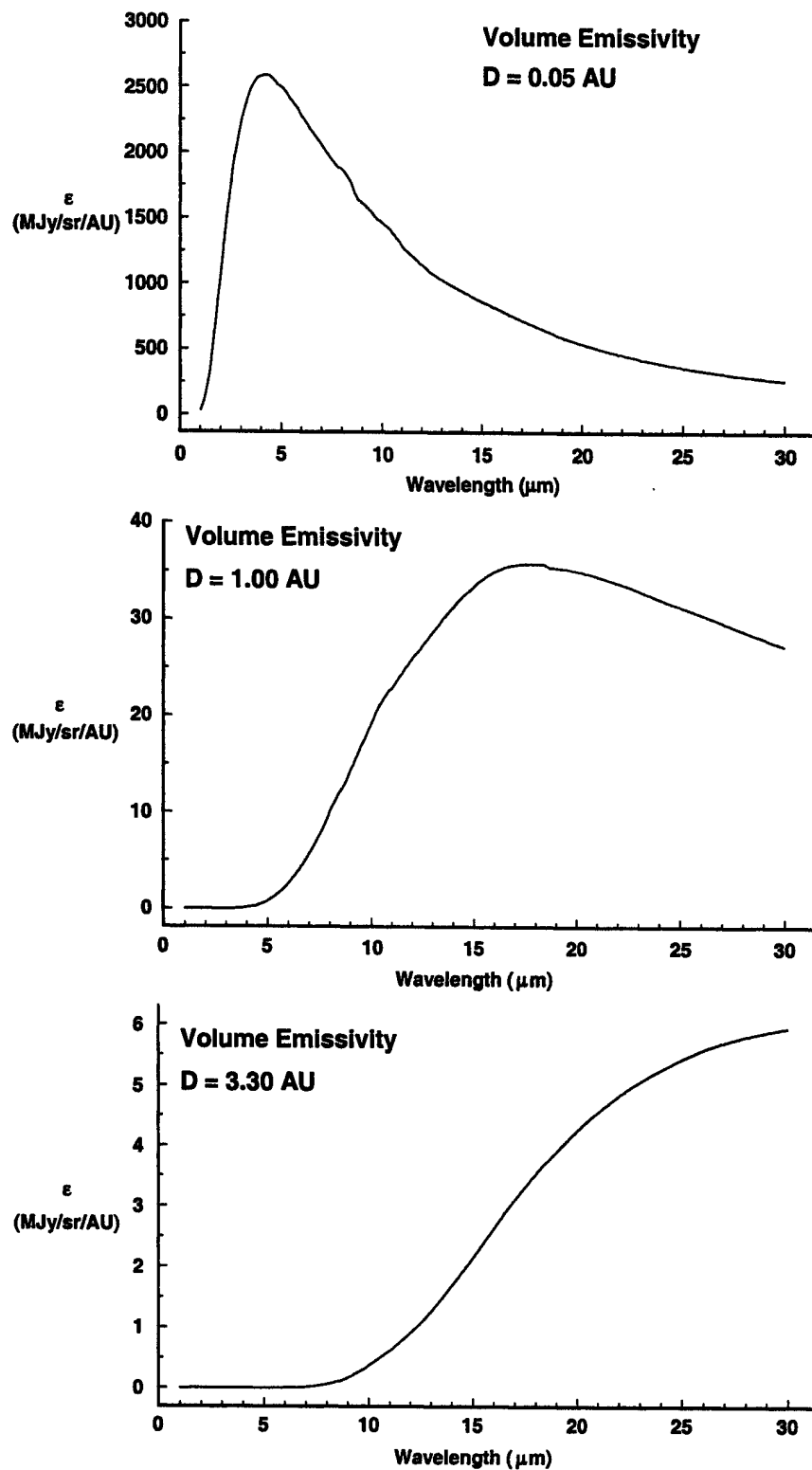
Figure 3: Volume emissivity. Astronomical silicate spectra for three different heliocentric distances: top, 0.05 AU; middle, 1.00 AU; and bottom, 3.30 AU.

2. History of CBZODY Improvements and Verification Efforts

Initial validation of the CBZODY code was performed against the Infrared Astronomical Satellite (IRAS) Zodiacal Observation History Files (ZOHF). Launched in 1983, IRAS surveyed most of the sky in four IR bands (12, 25, 60, and 100μm) during its 286-day mission (IRAS Exp. Supp.). Later in the program, CBSD validation was performed against the Cosmic Background Explorer (COBE) Diffuse Infrared Background Experiment (DIRBE) instrument with ten IR bands at 1.25, 2.2, 3.5, 4.9, 12, 25, 60, 100, 140, and 240μm.

The model has been developed with a set of parameters that are fit to the data by use of a non-linear least squares fitting routine. The total number of possible parameters is 90. However, as will be shown, some have been found to have negligible effect on the results, reducing the total number of parameters used to 11 not including the band model parameters. A listing of all parameters is given in Tables 1 through 4. Table 1 lists the parameters used for the physical dust cloud, which is the primary contributor to the measured radiance. Table 2 parameters are only used for IRAS data. Table 3 is for a solar system ring similar to Reach et al. (1995). Table 4 parameters are used with Reach et al.'s (1997) migrating band model.

Table 1: List of parameters for the physical dust cloud.

v	Power law index, taken to be 1
HWHM1	Half-width-at-half-maximum of plane 1
Znode1	Ascending node of plane 1
Zinc1	Orbital inclination of plane 1
NOthm1	Dust density at 1AU normalization in units of 10^{-17} particles/cm^3 of the dust cloud for plane 1
NObnd1	Dust density at 1AU normalization in units of 10^{-17} particles/cm^3 of the dust bands for plane 1
Break1	Breakpoint between planes (heliocentric distance of the warp) A breakpoint is deduced around Earth's orbit, we use 1.02 AU
HWHM2	Half-width-at-half-maximum of plane 2
Znode2	Ascending node of plane 2
Zinc2	Orbital inclination of plane 2
NOthm2	Dust density at 1AU normalization in units of 10^{-17} particles/cm^3 of the dust cloud for plane 2
NObnd2	Dust density at 1AU normalization in units of 10^{-17} particles/cm^3 of the dust bands for plane 2
Break2	Breakpoint between planes (heliocentric distance of the warp) If another breakpoint or warp exists in the dust cloud it would occur around the orbit of Mars. No such break has yet been observed so the Break2 value is set for the cloud maximum distance of 4 AU
HWHM3	Half-width-at-half-maximum of plane 3 (no evidence of existence)
Znode3	Ascending node of plane 3 (no evidence of existence)
Zinc3	Orbital inclination of plane 3 (no evidence of existence)
NOthm3	Dust density at 1AU normalization in units of 10^{-17} particles/cm^3 of the dust cloud for plane 3 (no evidence of existence)
NObnd3	Dust density at 1AU normalization in units of 10^{-17} particles/cm^3 of the dust bands for plane 3 (no evidence of existence)
NOa2	Dust scattering normalization always taken as 0.012
Albedo	Dust albedo always taken as 0.3

Table 2: List of parameters for IRAS gain function. *Only used to correct IRAS data instrument problems.*

Offset	DC offset
sigma	Time constant
fscale	Scale factor
again	Zero point gain

Table 3: List of parameters for the solar ring. *The solar ring model is not directly used but is a consequence of the warped dust cloud.*

Ring_nrm (x2)	leading and trailing ring Normalization density
Ring_ang (x2)	leading and trailing ring-earth separation (deg)
Ring_wl (x3)	leading ring characteristic widths (AU)
Ring_wt (x3)	trailing ring characteristic widths (AU)

Table 4: Migrating band model parameters. *Parameters used in CBZODY taken from Reach et al. (1996).*

$i_{latitudinal}$ (x7)	The latitudinal inclination is the observed displacement from the ecliptic plane in the sky.
$i_{orbital}$ (x7)	The orbital inclination is the orbit's tilt
n_0(x7)	Dust family relative strengths
δ_ζ (x7)	Dust family characteristic width
v_i(x7)	Density scale (adjusts central density)
p_i(x7)	Power law, always taken to be 4 (adjusts sharpness of latitude peaks)
R_0 (x7)	Dust band minimum heliocentric distance. Always set to 3 AU.
Ω (x7)	Ascending node of dust band. Always taken to be the same as the dust cloud.

2.1 Improving CBZODY Fit to IRAS Data and Removing Extraneous Flux from Other Sources.

Most of the work on validating CBZODY has been the generation of a consistent set of parameters that work with all observational data sets. While working with the IRAS data, inconsistencies arose in the parameter fitting that could not be explained by varying the parameters. This suggested that the data could be contaminated by other, non-interplanetary, sources. We investigated sources of contamination and attempted to remove the extraneous flux to improve the fit validity. Figures 4 and 5 show two plots of the results of finding the best-fit parameter set using a non-linear least squares routine using IRAS data. Figure 4 shows the particle number density. Here, the results look promising. Both the Ascending and Descending scans show similar patterns with a decrease in density as we cross the plane of the Earth's orbit. Figure 5 shows the dust cloud inclination calculated at the same time. The story is very different here. No consistent dust cloud inclination can be found, although a large cluster is seen around 2°. This leads to the possibility that the parameter set determined is incorrect due to contamination from additional sources.

8

We have attempted to remove the largest source of contamination from the scans, the galaxy. Figure 6 shows a typical IRAS scan (pole-to-pole) which crosses the galaxy at -35° on this scan. We have come up with a methodology to remove the contribution of the galaxy. Briefly, the steps are:

1. Run the Zodiacal model for the scan at 100μm (least amount of solar system dust).

2. Subtract the model from the IRAS 100μm data set.

3. Scale the model-reduced scans by a color factor of 0.03845 (the 12μm/100μm color ratio derived empirically). And,

4. Subtract the scaled, reduced image from the 12μm data.

The results are shown in Figure 7. Now the residuals from the Galaxy appear as a small "ringing" around -35°. After performing the non-linear least square fit the results are indistinguishable from those seen in Figures 4 and 5. Since we found that the galaxy is not the major contributor of contamination to the IRAS scans, we were at a loss to explain the discrepancies in the data.

Figure 4: Results of NLS fitting to the IRAS dataset. All results fall within a particle density of 2.0 and $2.5 \cdot 10^{-17}$ particles/cm3.	Figure 5: Results of NLS fitting to the IRAS datasets. Although the results cluster around 2.0° significant scatter is seen in the results.

Figure 6: Typical IRAS scan. The plane of the galaxy is clearly visible around –45°.

Figure 7: Results of removing the galactic component. The contribution from the galaxy is seen as a small ringing around –45°.

2.2 Replacing the CBZODY Solar 5770°K Blackbody Approximation with the ATLAS8 Solar Spectrum Model.

Two of the CBSD codes, CBAMP (the asteroids, Moon, and planets simulation) and CBZODY (the zodiacal light simulation), require a solar spectrum. Early versions of these codes used a blackbody function that sufficed for the infrared portions of the spectrum; however, this is inadequate for visible and shorter wavelengths. The current requirement of CBSD is to have a short wavelength limit of 0.1μm. To demonstrate the need for an adequate solar spectrum, Figure 8 shows a Blackbody spectrum (dashed line) compared to our adopted solar model, ATLAS8 (solid line). Above 0.5μm, the two curves are nearly indistinguishable. Below 0.5μm, many line absorption features are visible along with a rapid decline of the solar spectrum to Lyman-α. Thus, the blackbody spectrum is inadequate below 0.5μm because of the absorption lines.

The CBSD adopted solar spectrum is a model run of a stellar atmosphere program called ATLAS8. The ATLAS code is an ongoing development effort of Dr. Robert Kurucz at the Harvard-Smithsonian Center for Astrophysics in Cambridge, Massachusetts (Kurucz 1970, 1979). We have chosen the ATLAS code because it is an accepted standard in the astronomical community for stellar atmosphere modeling.

We have chosen not to use observed spectra due to the limited availability of data, their own calibration history, or the extent of atmospheric contamination. A series of satellites have observed the Sun's spectral irradiance since 1969. However, these are generally UV observations below 0.4μm. It is also considered out of the scope of the CBSD program to reconcile the different observations.

The ATLAS code is a general-purpose stellar atmosphere program producing temperature, pressure, and number densities versus depth into a stellar atmosphere. The code has

been verified over many stellar spectral classes and is generally accepted in the astronomical community as the standard of stellar atmospheres. For the CBSD codes, we used the ATLAS8 version of the code. The Sun was modeled with an effective temperature of 5770K and a gravity of

$$\log g = 4.44 \, cm/s^2$$

By using the resulting model, the spectrum was computed at 342 grid points from 0.023 to 100μm. Figures 9 and 10 compare the ATLAS solar spectrum to the solar spectrum used in the MODTRAN atmospheric code. While the MODTRAN spectrum has a higher resolution than the ATLAS run, this was not seen as an advantage to the CBSD program. The higher resolution is not required by the CBSD project and will slow the execution speed of the CBSD codes. More importantly, the MODTRAN spectrum does not go below 0.2μm, which is inadequate for CBSD.
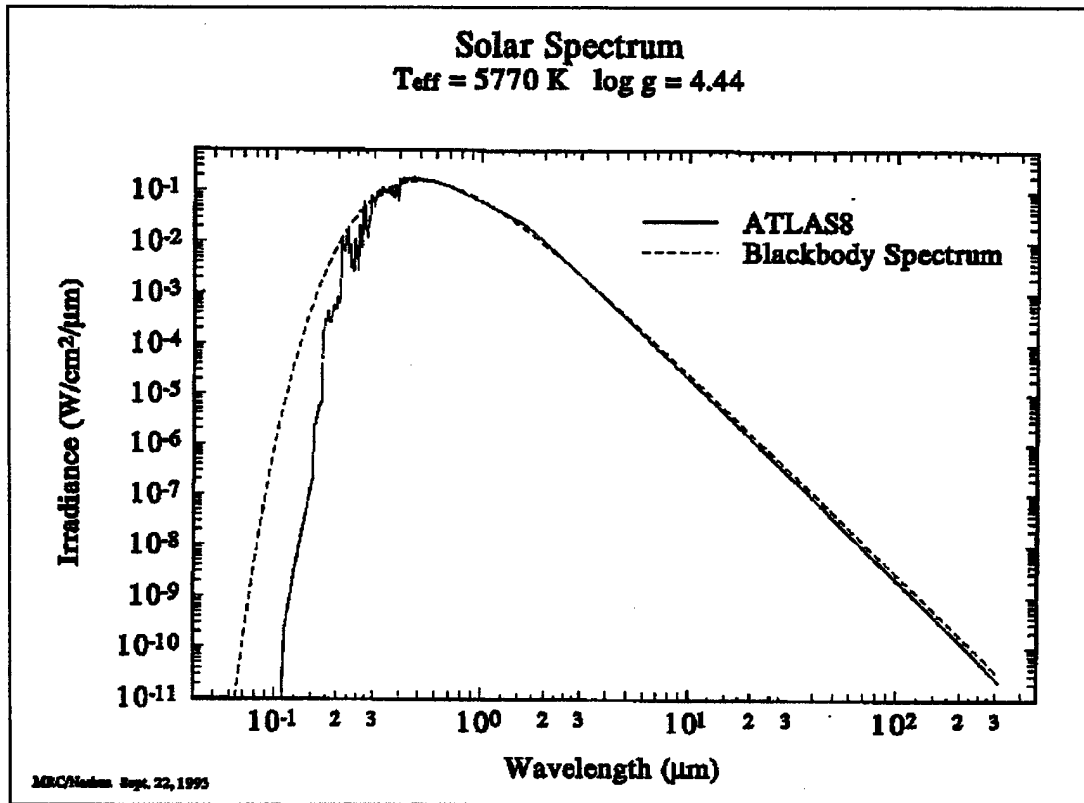
Figure 8: Blackbody, ATLAS8 comparison. The graph shows the comparison between the ATLAS8 spectrum and a 5770K blackbody curve. The blackbody overestimates the solar spectrum at wavelengths below 0.5μm.

Solar Spectrum

$T_{eff} = 5770 \text{ K} \quad \log g = 4.44$
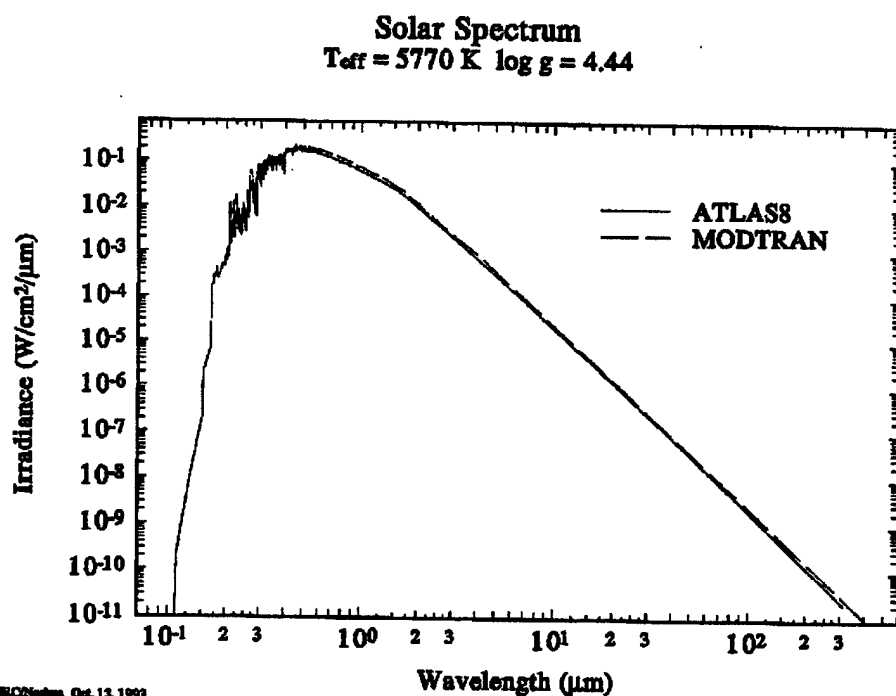
Figure 9: Comparison of ATLAS8 to MODTRAN. The MODTRAN atmospheric modeling code uses a measured solar spectrum from 1 to 50000 cm^{-1}. This plot compares the ATLAS8 model to the MODTRAN measure data.

Solar Spectrum

$T_{eff} = 5770 \text{ K} \quad \log g = 4.44$
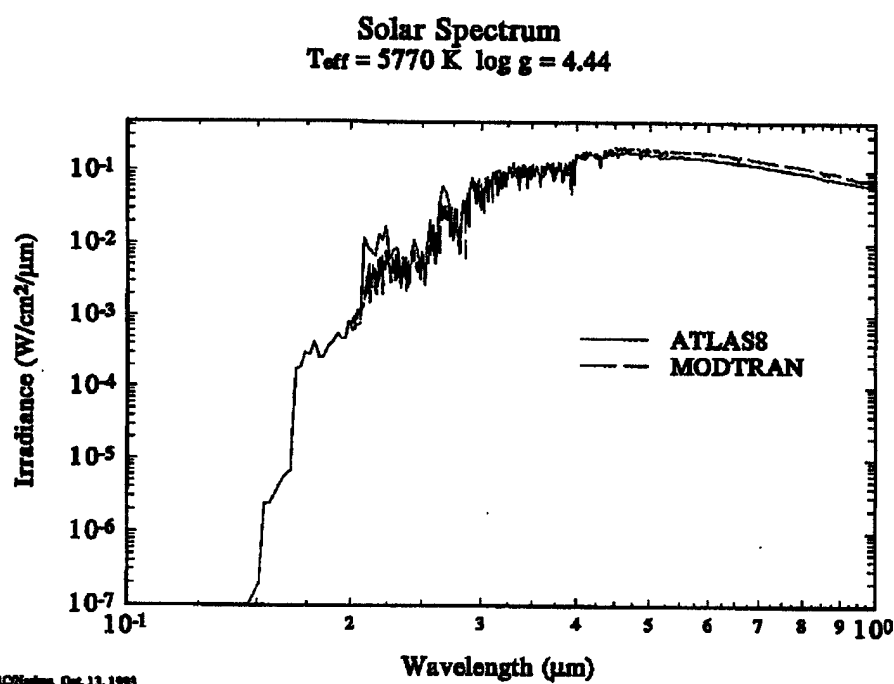
Figure 10: Comparison of ATLAS8 and MODTRAN between 0.1 and 1μm. The agreement between model and measurement is quite good in this region.

12

2.3 COBE South Ecliptic Pole (SEP).

In 1992, early COBE observations of the South Ecliptic Pole (SEP) were made available (Bennett et al. 1992). CBZODY was then modified to allow a spectral response out to $300\mu m$ for comparison against all COBE/DIRBE bands. Figure 11 shows the observations of the SEP compared to CBZODY. The fit is good at the 12, 25, 60, and $100\mu m$ bands, but underestimated at all other bands. Figure 12 shows a comparison of CBZODY versus COBE with the addition of two other models. The short wavelength end is covered by the SKY model of Martin Cohen (1993). The long wavelength end is covered by the inclusion of galactic dust. The galactic dust is simply modeled by the sum of two blackbodies at 20K and 5K (Wright 1992). The fit is now acceptable over the entire wavelength range.
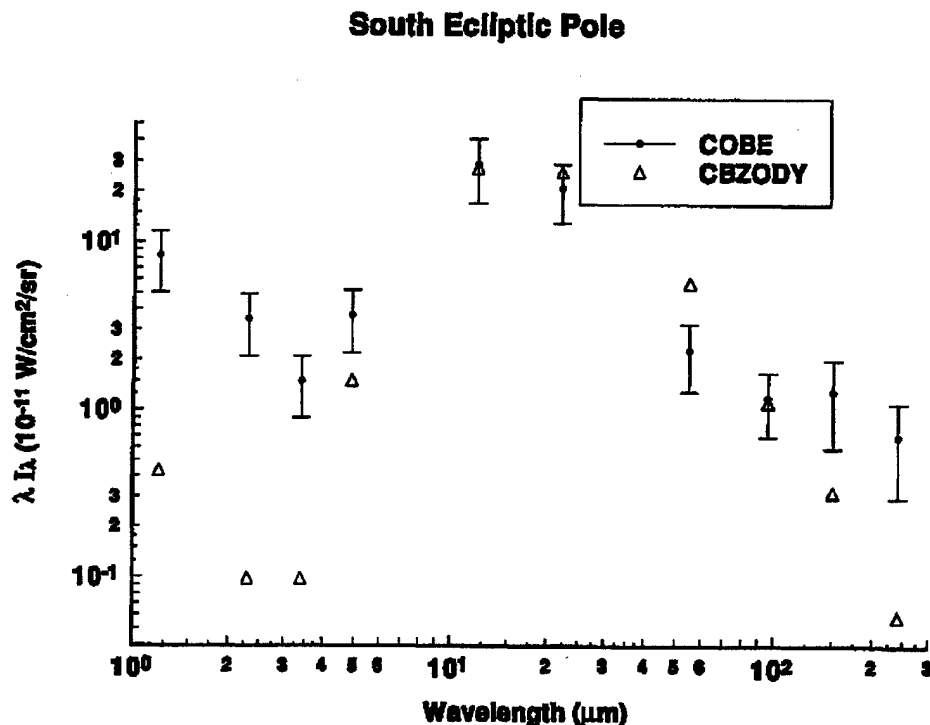
Figure 11: COBE SEP observations and CBZODY model comparison. The CBZODY model is compared to the SEP observations obtained by COBE. The fit is acceptable at the IRAS comparable bands of 12, 25, 60, and $100\mu m$. At the other 6 bands the model underestimates the SEP observations.

13

South Ecliptic Pole
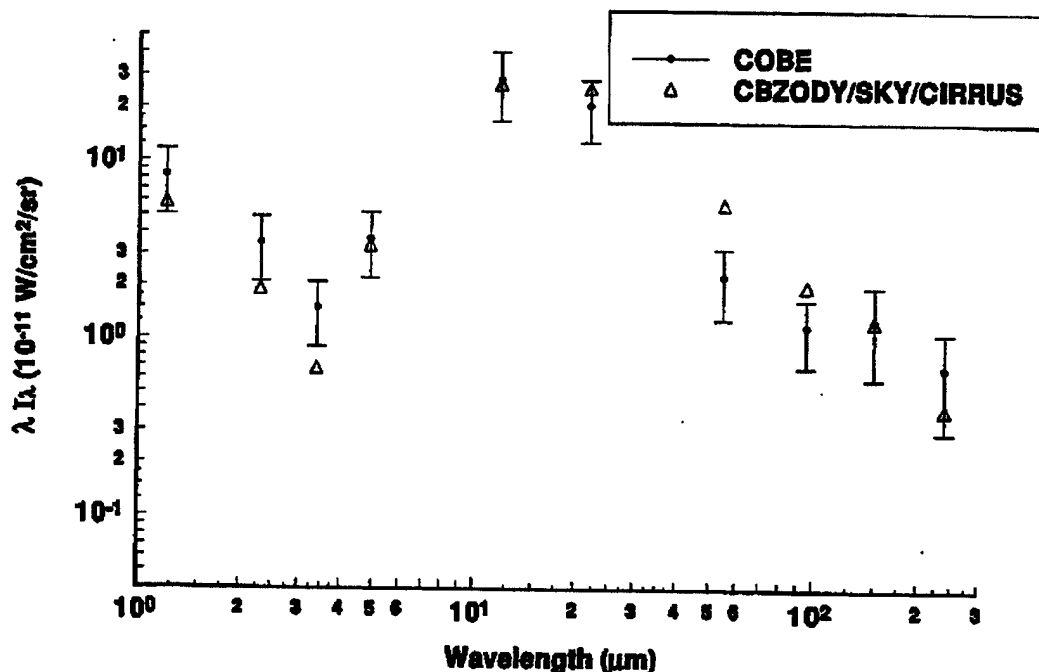
Figure 12: COBE SEP observations versus three models. By including the contribution of two additional models, SKY (Cohen 1993) and an elementary cirrus model (Wright 1992) the entire SEP flux is explainable.

2.4 Non-linear Least Squares Comparisons of the CBZODY Generalized Parameter Set to the IRAS Zodiacal Observation History Files (ZOHF).

The goal of the CBZODY model has been to describe the interplanetary dust cloud in such a way that the model successfully reproduces the observed dust radiance in visible and infrared, with a minimal set of parameters. The parameters can be broken down into two categories: geometric properties and dust properties.

The orbital properties are the inclination of the dust symmetry plane, ascending node of the symmetry plane, scale height, and the in-plane dust density distribution. The scale height is the out of plane dust distribution usually denoted as a half-width-half-maximum (HWHM) value. A dust density distribution of $1/r^v$ with $v=1$ is predicted on theoretical grounds from Poynting-Robertson drag on the particles (Briggs 1962). The dust properties are albedo, and composition.

Initial work with the CBZODY model was initiated with the IRAS Zodiacal Observation History Files (ZOHF). We analyzed a set of 226 pole-to-pole scans with a non-linear least square fitting routine. This set represents all pole-to-pole scans reaching North of +85° ecliptic latitude and south of -85° degrees ecliptic latitude. We allowed four parameters to vary during the NLS run, the inclination (i), the density at 1 AU (N_o), the ascending node (Ω), and the scale height (Γ).

14

Error analysis of the 226 scans yields a mean error for the entire set of 1.0%. Typical maximum (single pixel) errors are 5.3%. The largest single pixel error is 70%, for the scans crossing the ρ Oph complex. When calculating errors we have excluded the plane of the galaxy from our error analysis since this region is not included in our model. Figure 13 gives a typical NLS fit to the data.

From the 226 scans, we defined a generalized parameter set (Table 5). The mean error for the entire set of 226 scans using the generalized parameter set is 6.4%. The largest, instantaneous error is 69.3% again due to the ρ Oph complex. In addition, the largest mean error for a scan is 10.0%. Typical, maximum errors (single pixel) are 11.3%. Figure 14 gives a typical fit to an IRAS scan using the generalized parameter set.

The composition was found to be best represented by astronomical silicate. Obsidian has also been tried as a dust material but fails to represent the observed dataset. The albedo of the dust has been set to 0.3. The dust density exponent has been taken as $\nu = 1$.

Table 5: Set of Parameters used for all IRAS ZOHF datasets.

ν	Power Index	1.0
Γ	HWHM	0.25
Ω	Ascending Node	90.0°
i	Inclination	1.40°
N_o	Normalization Density	2.35
a	Dust Albedo	0.3

SOP 117 Obs 20
Band 1
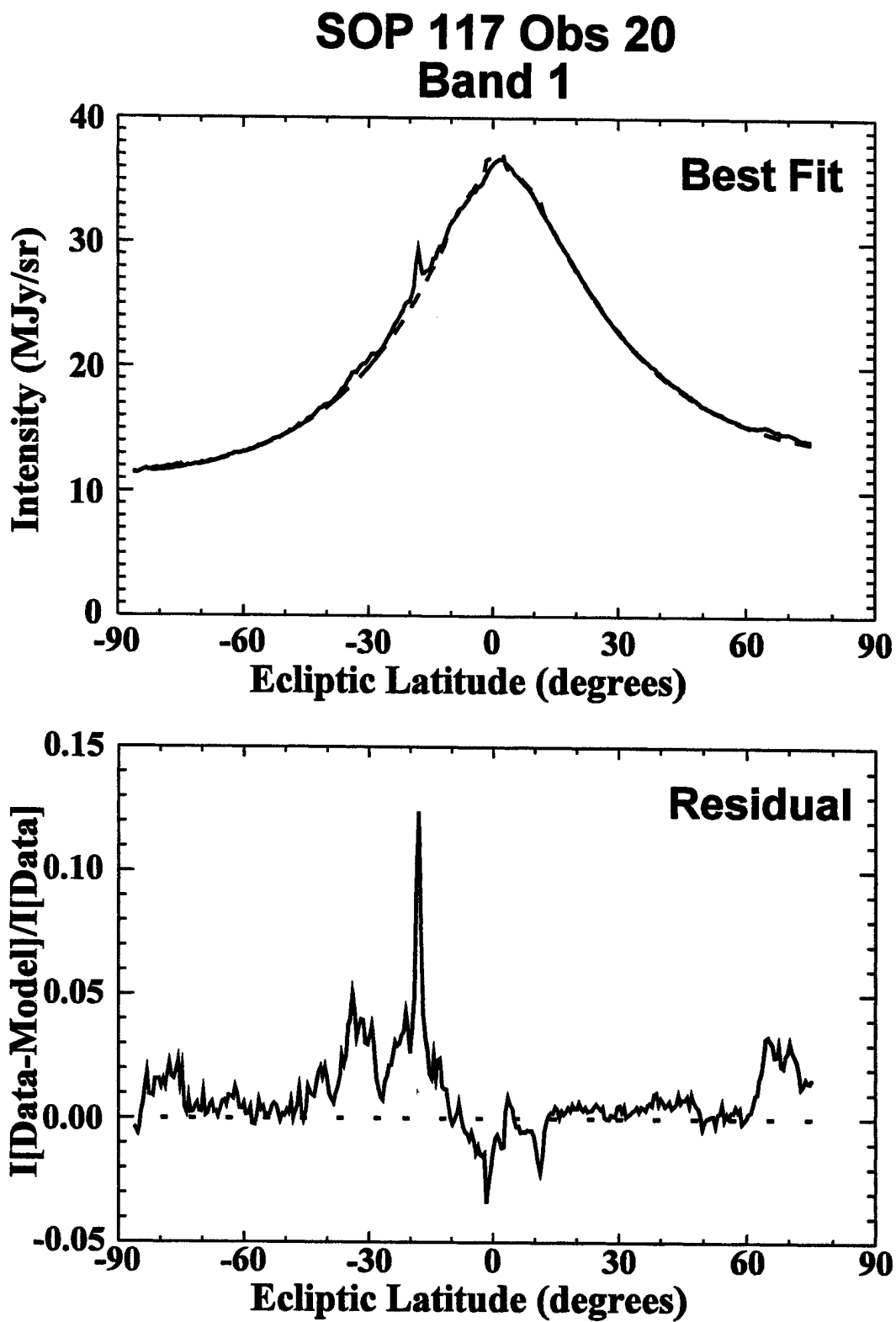
Figure 13: NLS fit to an IRAS scan. This fit is typical of the NLS fits to the IRAS data. Top, the solid line shows the IRAS observations and the dashed line is the CBZODY fit. Bottom, the residual in the sense IRAS-CBZODY (solid line) with a 0 MJy/sr reference line (dashed).
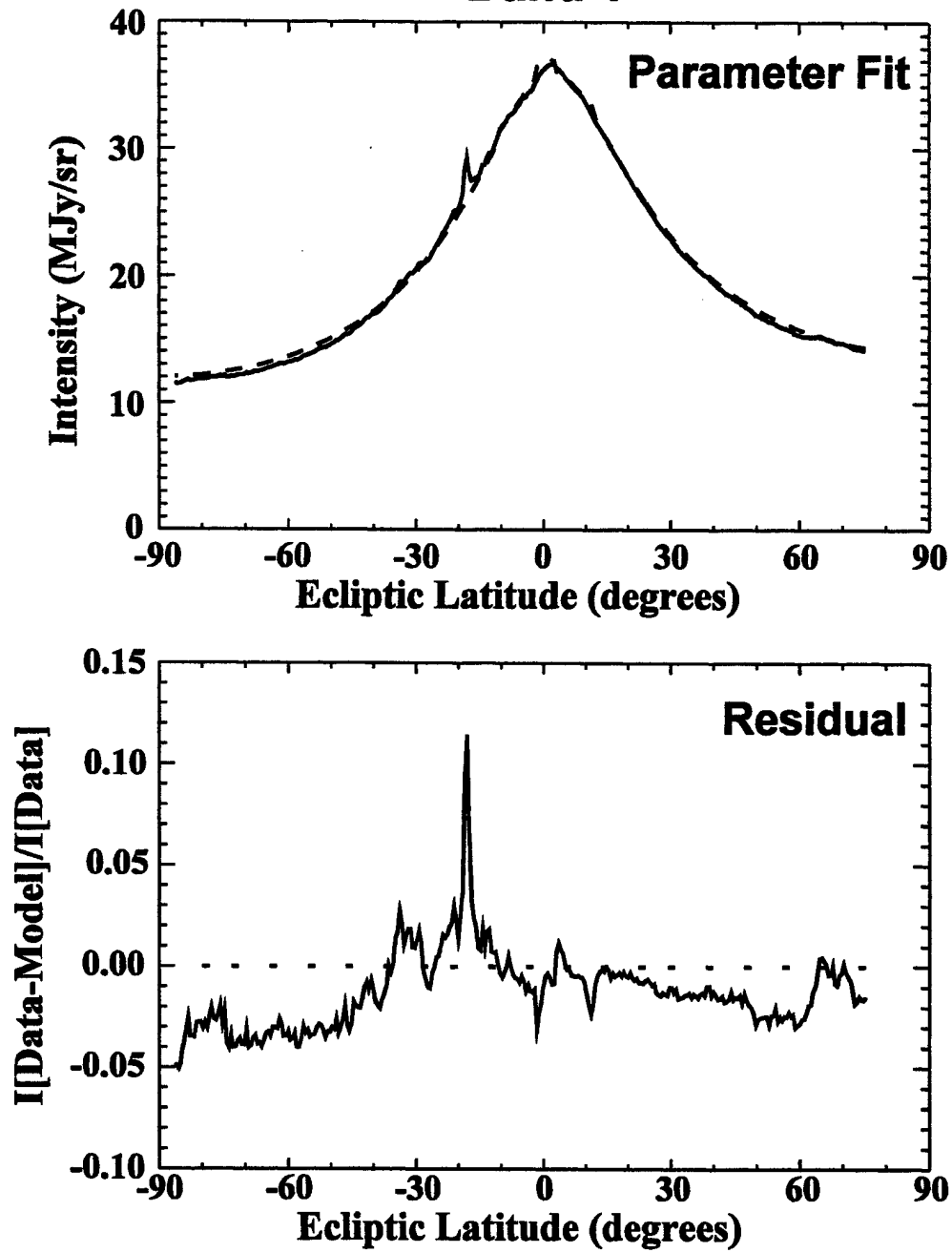
Figure 14: Fit to an IRAS scan using the generalized parameter set. Like figure 13, this fit is typical of the generalized parameter set fits to the IRAS data.

2.5 Comparison to COBE: IRAS Calibration Data at 12μm.

When early results from COBE were made available a calibration problem between IRAS and COBE was discovered (Beicman and Wheelock 1993). To compensate, gain and offset corrections were applied to the IRAS to match COBE (Beichman and Wheelock 1993). Table 6 shows the values of the corrections to be applied to the IRAS dataset to match the COBE observations. The resulting plot is Figure 15. The sense of the correction was:

$$I_{corrected} = gI_{IRAS} + f$$

Table 6: Beichman and Wheelock's (1993) IRAS to COBE calibration constants.

IRAS Band	g Gain	f Offset (MJy/sr)
1	1.06±0.02	-0.48±0.43
2	1.01±0.02	-1.32±0.74
3	0.87±0.06	+0.13±0.65
4	0.72±0.07	-1.47±0.88
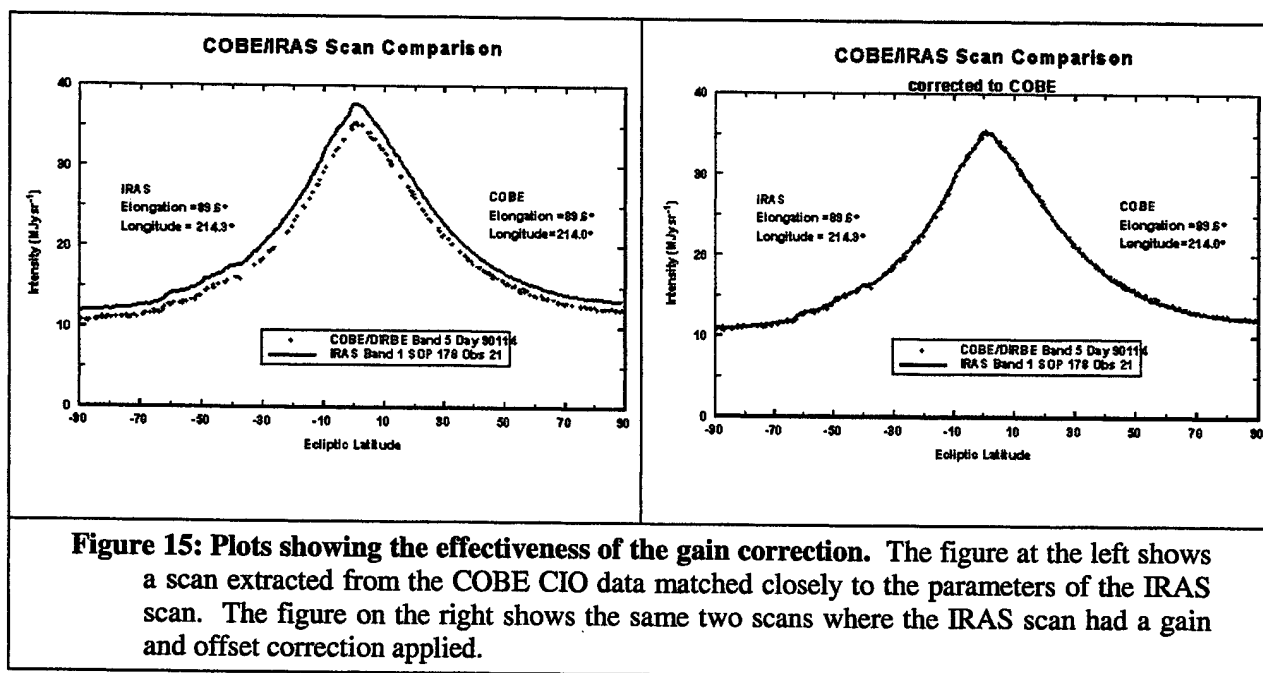
Figure 15: Plots showing the effectiveness of the gain correction. The figure at the left shows a scan extracted from the COBE CIO data matched closely to the parameters of the IRAS scan. The figure on the right shows the same two scans where the IRAS scan had a gain and offset correction applied.

2.6 CBZODY Sensitivity Analysis.

Duel and Walker (1989) presented evidence that the IRAS observations contained an uncorrected photon induced responsivity enhancement (PIRE) effect that manifests itself as a time variable gain function. They produced a model gain function for 60 and 100μm.

The development of detector models at 100 μm and, to a lesser extent, 60 μm, has been facilitated by the observation of the galaxy. The galaxy is, over the lifetime of the IRAS mission, an unchanging, very bright source. The galaxy dominates the sky at 60 and 100 μm. This is not the case at 12 and 25 μm. Here the zodiacal light is the dominant source and exceeds

18

the brightness of the galaxy in all regions except the galactic center. The zodiacal light has a time varying component. For this reason, no quantitative model of the non-linear detector responses has been created at 12 and 25 μm. In this section, we describe a methodology using a numerical model of the zodiacal light to define a model of the detector non-linearities.

At 100 μm, two sources can contribute to detector uncertainties. These are the hysteresis effect and the photon induced responsivity enhancement (PIRE) changes. The hysteresis tends to produce an overall baseline variation and is responsible for the tails seen in IRAS scans after passing over a point source. The hysteresis effect is not considered here since the averaging of the ZOHF obliterates some of this effect and the time constant of this effect is short (on the order of tens of seconds). The effect of the PIRE is to produce a time varying gain. The detector has a memory of previous exposure to light.

Following the paper by Duel and Walker (1989, *A&A*, **81**, 207) we constructed a time variable gain function:

$$g(t) = A \cdot \left(1 + f \sum_{t'=t-2\sigma}^{t} F_{12}^{IRAS}(t')e^{-\left(t-t'/\sigma\right)}\right)$$

Where:

A = Zero point gain

f = Scale factor

$F_{12}^{IRAS}(t)$ = IRAS observed flux at 12 μm

t = Time of observation (seconds since 1 Jan 1981)

σ = Decay time

The flux at the focal plane is then:

$$F_{12}^{0}(t) = g(t)F_{12}^{Model}(t)$$

with:

$F_{12}^{Model}(t)$ = CBZODY prediction of flux

A sensitivity analysis was performed varying the hypothesized decay time and scale factor of the time varying gain. We then performed the NLS parameter fit to the list of scans given in Table 7.

The ZOHF is a collection of all IRAS survey scans. However, the data have been resampled to 0.5°x0.5° equivalent pixel sizes. All detectors cross-scan were averaged together along with average 8 seconds worth of data in-scan (IRAS ES). Two components were left out of the ZOHF, these are the Additional Observations (AOs) which are a set of pointed observations, and the calibration reference sources (the stim flashes). The result is that the ZOHF do not constitute a complete history of energy falling on the detector. A subset of data was chosen from the ZOHF only choosing the contiguous scans. In addition, the stim flashes were added back into the data set using two flashes before and two flashes after each stim flash. The value of the stim flash was taken to be a single 0.5°x0.5° spike with an intensity of 17 MJy/sr.

The final sample consisted of 32 scans, which are listed in Table 7, along with their elongation and the ecliptic longitude of the pointing as the scan crossed the ecliptic. Table 7 also indicates if the scan were ascending or descending, that is, if the scan crosses the ecliptic south to north or north to south. Additionally, the data set has no gaps due to the avoidance strategy and data dropouts.

Table 7: Candidate scans for use of time variable gain. All scans are contiguous, no data gaps, and extend pole-to-pole.

SOP	Obs	Elongation	Ecliptic Longitude	Scan Direction
67	5	86.09	64.70	Descending
71	5	88.34	68.97	Descending
106	22	94.19	264.21	Ascending
117	20	92.70	96.53	Descending
119	5	93.18	97.72	Descending
145	26	92.91	110.59	Descending
174	22	93.40	298.47	Ascending
174	26	87.45	119.42	Descending
178	20	91.08	302.74	Ascending
178	24	89.76	123.69	Descending
209	26	92.44	141.30	Descending
212	14	94.84	315.37	Ascending
238	26	94.83	327.99	Ascending
241	25	93.49	330.84	Ascending
244	26	91.31	334.40	Ascending
331	4	92.42	199.40	Descending
333	6	93.60	201.54	Descending
357	39	86.42	206.10	Descending
359	32	87.59	208.23	Descending
359	37	94.64	26.10	Ascending
361	37	93.47	28.23	Ascending
362	12	92.96	28.94	Ascending
363	35	92.29	30.37	Ascending
365	34	91.11	32.50	Ascending
365	41	90.94	32.74	Ascending
368	20	89.08	35.83	Ascending
395	8	92.56	230.11	Descending
526	33	82.42	284.18	Descending
527	38	94.86	107.35	Ascending
562	30	89.02	130.60	Ascending
564	30	88.36	132.26	Ascending

Each of the 32 scans, given in Table 7, were fit using the NLS fitting routine. For each pair of Scale and Decay Time the standard deviation of the five parameters were computed. From this, we found the minimum standard deviation for the Scale/Decay Time pair.

Figure 16 shows the results for the ascending node. A clear minimum was found with $f_{scale} = 0.00009$ MJy^{-1} and $\sigma = 348$ s. For the test set of 32 scans (mixed ascending and descending scans) this changed the Ascending Node from a best fit value of 76.8° and a standard deviation of 13.4° for the scans without using the gain function to 77.3° and a standard deviation of 7.6° when the gain function is used. It was also found that the other four parameters (Offset, Inclination, Scale Height, and Density) are not sensitive to varying the gain, showing less than 10% variation in <u>standard deviation</u> from the normal to the gain varying fits.
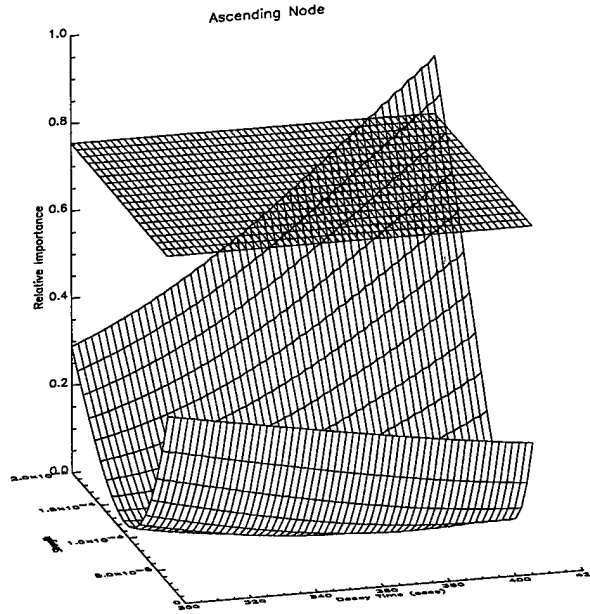
Figure 16: Sensitivity analysis results. The sensitivity analysis revealed a clear tendency to improve the fit when using a time variable gain.

Table 8 gives a comparison of the "old" and "new" values of the CBZODY parameter set. Note that the offset found in the "old" set is within the error limits found on the COBE/IRAS calibration for 12μm.

Table 8: Summary of results. The time variable gain shows the fit parameters are affected by its inclusion.

	Without Gain Function	With Gain Function
Offset (MJy)	0.365	1.22
Ascending Node	76.8°	77.3°
Inclination	2.06°	2.36°
Scale Height, HWHM (AU)	0.241	0.243
Density (10^{-17} particles cm^3)	2.35	2.08

For an additional part of the study, we compared the effect of the gain function on two closely matched, but opposite direction IRAS scans.

Figures 17 through 20 give two pairs of scans taken six months apart with an ecliptic longitude of 323°. These figures give the original IRAS data, the model fit, the residual, and the parameter set used to generate the model. For these, we used the following values:

$f = 0.00002$

$A = 1$

$\sigma = 250$ s

21

Figure 17 compares the scan paths in ecliptic coordinates. Figure 18 shows the uncorrected residuals for the two scans. Figure 16 shows the use of the gain function. Figure 19 a) shows the original data, the model fit and the residual. The model fits seems poor since we have not included the contribution due to the band structure. Part of this exercise was to show the band residual and the derived band model could change with the inclusion of a variable gain function. Figure 19 b) shows the gain functions. Note that SOP 181 Obs 26 has a small data gap around –60° and hence was not included in Table 7. Figure 20 now compares the two residuals after applying a time varying gain. Comparing Figures 18 and 20 shows a marked difference in the perceived band structure. Because of the gain function, deriving band information can be a formidable task.

IRAS Scan Paths
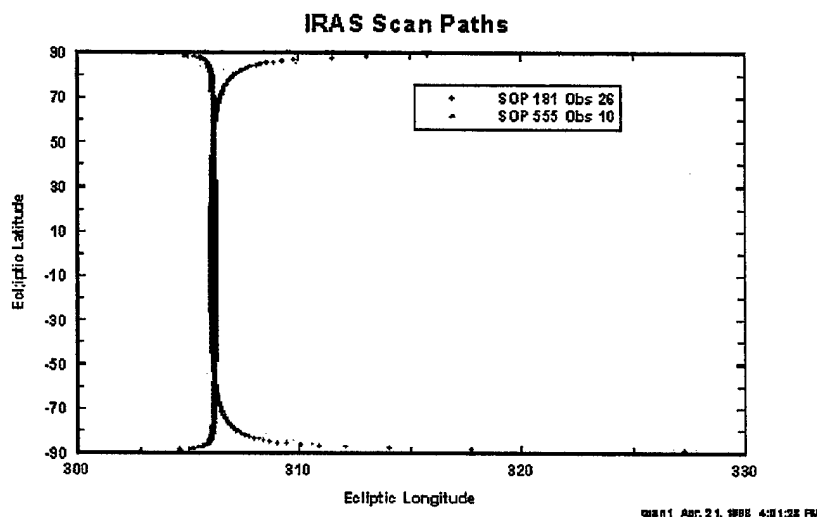
Figure 17: Scan sky locations. The map shows the location in the sky of the two candidate scans. They cover nearly the identical region of the sky.

IRAS scan pairs
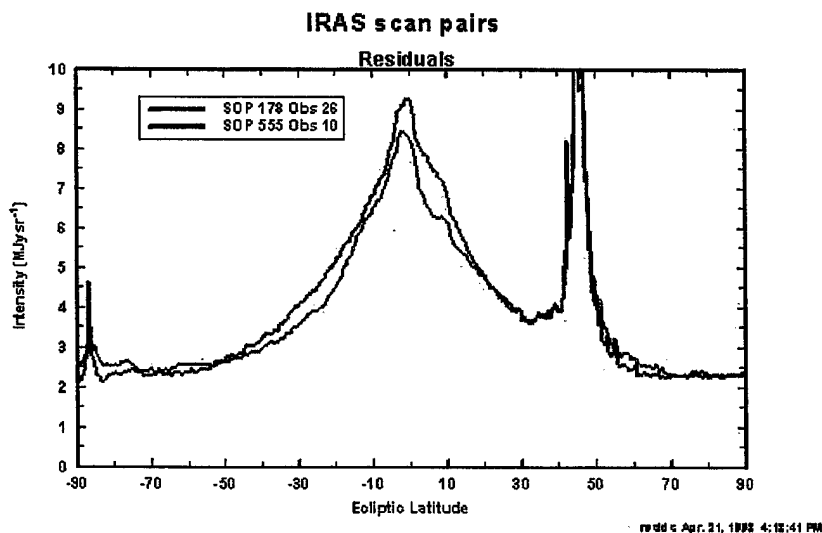
Figure 18: The uncorrected residuals. The residual plots are shown but the band model has not been included in the model fit. The residuals then represent the contribution to the zodiacal light from the bands.
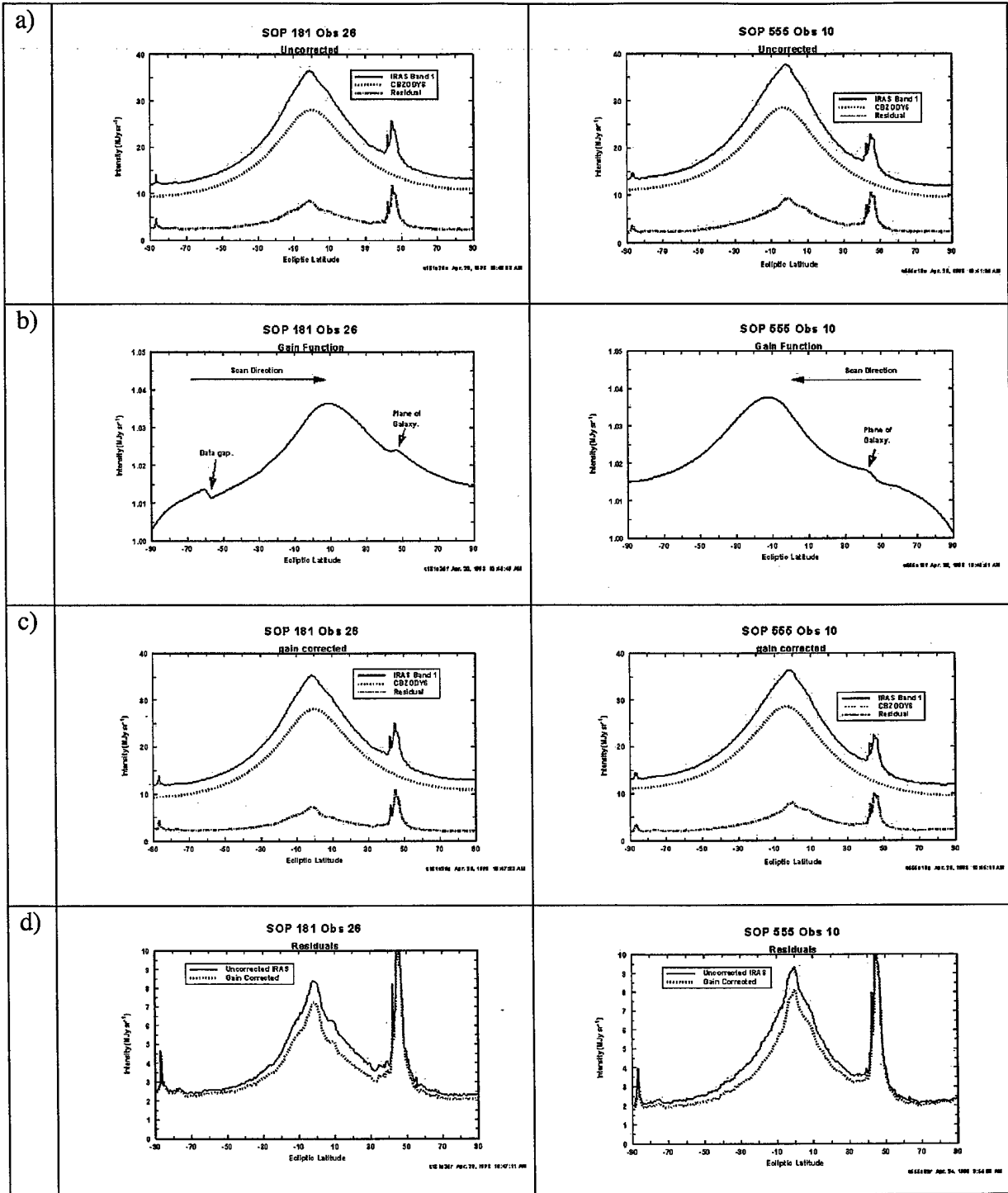
Figure 19: Results of using the time variable gain model. Figure 19a shows the original data, the model (without bands), and the residual (band component) for the two scans. Figure 19b shows the gain function and the scan direction. Figure 19c shows the original data the model and the residual when the gain function has been included. Figure 19d compares the residual with and without the gain function for the two scans.

IRAS scan pairs

Residuals - Gain corrected
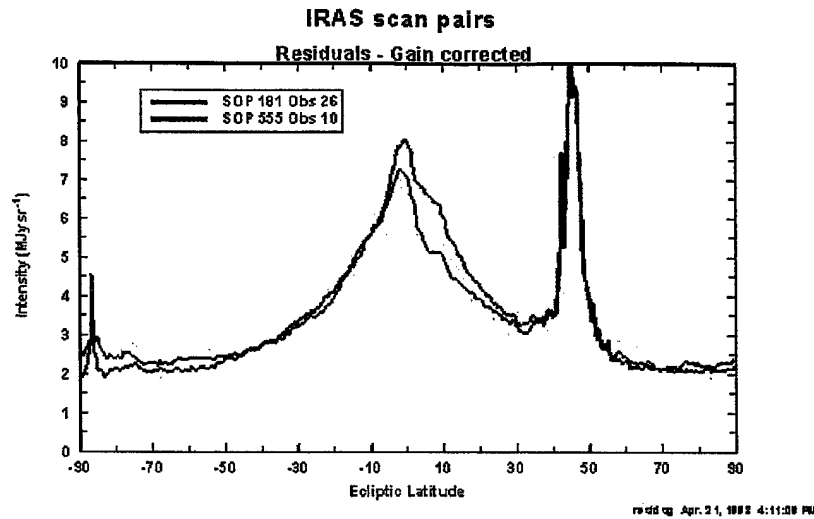
Figure 20: Residual comparison with gain function. This figure shows the two residuals from the two scans with the gain function included. Compare the results to Figure 18. The gain function has changed the shape of the band residuals and would affect any band model derived from residuals of Figure 18.

2.7 Use of COBE/DIRBE Weekly Averaged Skymaps

Analysis of IRAS data leads to considerable inconsistencies in the definition of the generalized parameter set. Coupled with the time variable gain and the realization that it was not a simple task to recalibrate the IRAS data, we began looking for other data sources. In October 1994 the COBE mission produced a data product known as the weekly averaged skymaps. These data are a weekly average of all scans taken during that week and binned by ecliptic longitude and latitude. Figure 21 shows the results of using a weekly skymap to validate CBZODY. The satellite collected data only between the elongations of 64° and 124°. The two large circular voids represent regions were no data was taken, either less than 64° or greater than 124°. In Figure 21, the larger circle, on the left, is the location of the Sun. Notice that the immediately to the right and left of that circle are dark rings. Figure 22 is an in-plane slice near the Sun from the same weekly skymap. There is a large discrepancy between the model and data for ecliptic longitudes 5 – 15°.

24
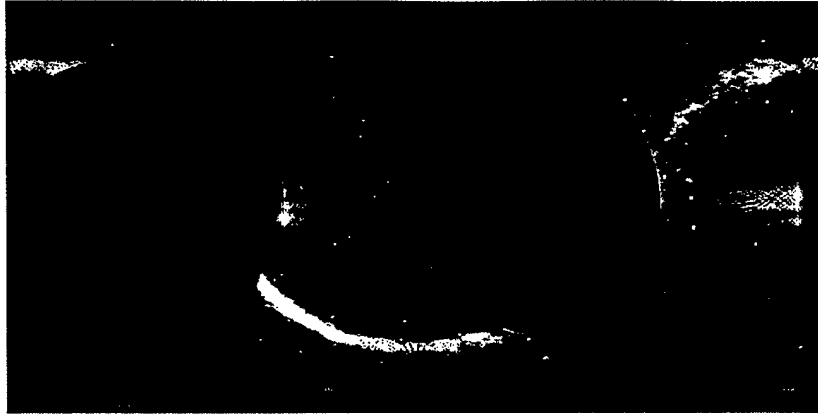
Figure 21: Weekly skymap residual image. The weekly skymap residual image shows a dark ring around the solar location (largest void) when using an average elongation for the model run, indicating a problem with the model. White >5 MJy/sr and black < -5 MJy/sr.
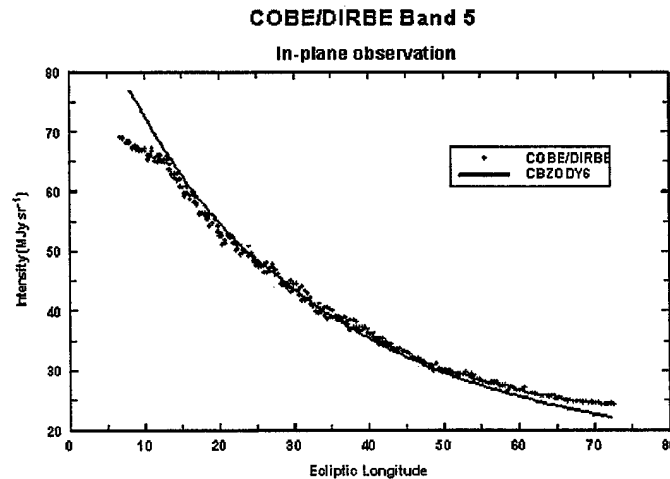
Figure 22: Ecliptic longitude plot of weekly skymaps. This figure shows the in-plane data from a COBE weekly skymap plotted versus ecliptic longitude. Notice the data's marked downturn below 10° compared to the model.

We explain this discrepancy by noting that the data are binned by ecliptic longitude over a seven-day interval. Over those seven days the Sun moves some 7°. This means that the elongation sampled at a particular ecliptic longitude changes. Figure 23 shows seven distinct days, each separated by 1 day, produced with the CBZODY model. The solid curve in Figure 23 shows the average of those seven days worth of data

Figure 24 shows the COBE weekly sky map data overlaid with a weekly averaged CBZODY model. While the model is a better representation of the data, the weekly sky maps do not contain enough information to allow a model to properly represent the span of days. The data taken are not necessarily exactly one day apart. It is also not possible to tell if a sample is 7 samples or more or less. The weekly skymap data are then useless in defining a set of parameters for the CBZODY model.

25

CBZODY6 Model

In-plane
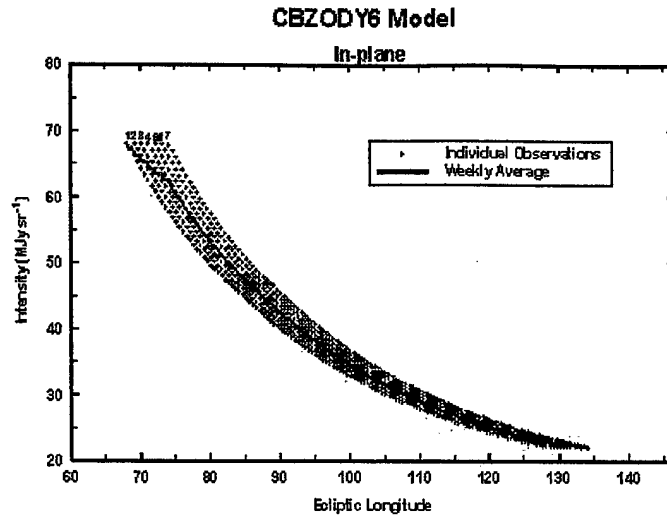
Figure 23: Weekly skymap model. Seven scans obtained from the model are shown along with the average versus ecliptic longitude. Each scan however, has a different elongation.

COBE/DIRBE Band 5

In-plane observation
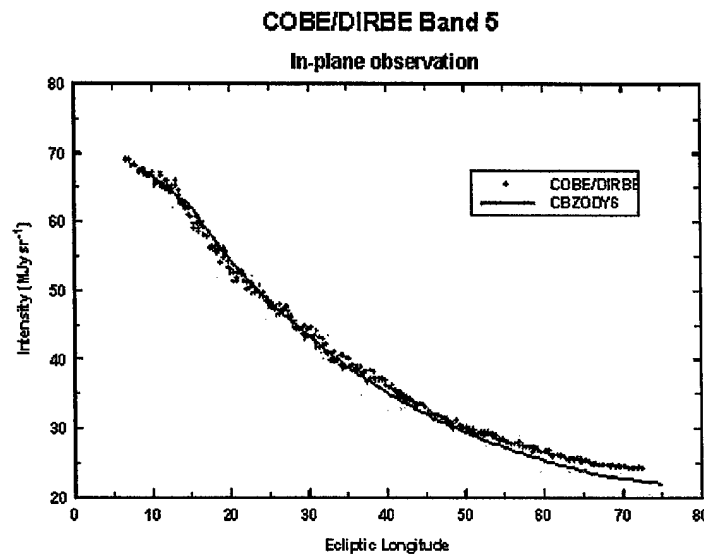
Figure 24: The averaged model versus weekly skymap. A fit to the data is obtained by averaging seven scans. However, uncertainties in the data make this an impractical solution.

2.8 In-Plane Comparisons

The COBE and IRAS data sets both suffered from the same limitation; namely, their observations were limited between 60° and 120° in solar elongation. However, over the course of 20+ years of zodiacal observations many measurements have been taken from balloon, small rocket, and other small satellite programs. Figures 25 and 26 show in-plane coverage from close to the Sun and extending nearly to the anti-solar point. In addition to the IRAS and COBE data, we have included Leinert and Grün's (1990) compilation of small rocket, balloon, and satellite data, and the Air Force's ZIP, MSX, and ELMS programs.

26

Figure 25 is a fit of the CBZODY model to 12μm datasets such as IRAS Band 1 and COBE Band 5. Doing this fit, it is was necessary to change the parameter set such that v=0.8. Figure 26 is a fit of the CBZODY model to 25μm datasets such as IRAS Band 2 and COBE Band 6. Doing this fit, it is was necessary to change the parameter set such that v=1.1. These unusual discrepancies were the in-plane dust density power law deviated from the Poynting-Robertson case were caused by the lack of color corrections being applied to the various datasets.

In-Plane Intensity
12 μm
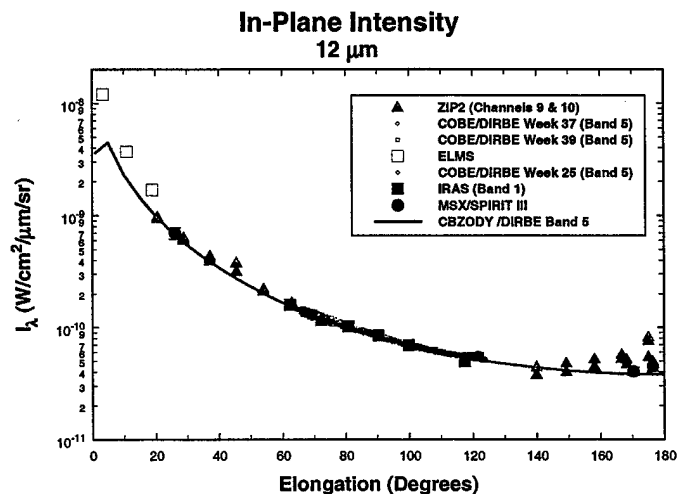
Figure 25: A compilation of 12μm datasets for ecliptic plane crossing. The solid curve is the CBZODY model prediction using the COBE/DIRBE Band 5 spectral response. Additional data are: ELMS; ZIP2 Channels 9 & 10; COBE/DIRBE Band 5 taken from three separate weekly average skymaps; IRAS Band 1 ecliptic plane crossing averages at five elongations; and two MSX datapoints.

In-Plane Intensity
25 μm
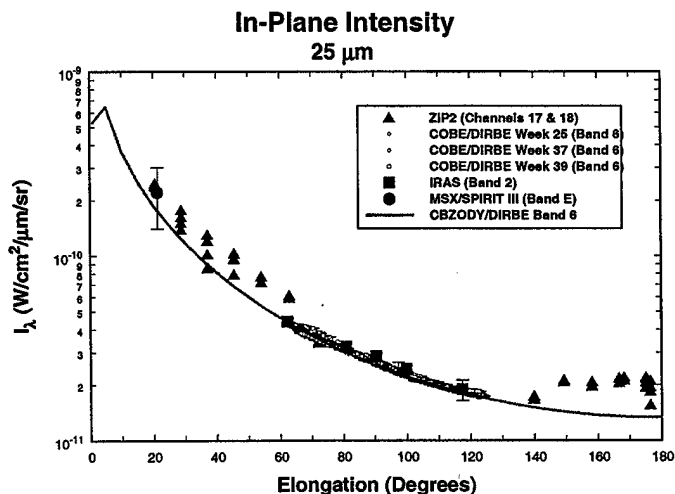
Figure 26: A compilation of 25μm datasets for ecliptic plane crossing. The solid curve is the CBZODY model prediction using the COBE/DIRBE Band 6 spectral response. Additional data are: ZIP2 channels 17 & 18; COBE/DIRBE Band 6 taken from three separate weekly average skymaps; IRAS Band 2 ecliptic plane crossing averages at five elongations; and one MSX datapoint.

Figures 27 and 28 show the results of fitting the CBZODY6 data to various datasets after color corrections were taken into account. For these plots, the dust density distribution followed Poynting-Robertson light drag and we set ν=1. To generate these plots a lunar mass distribution was assumed, however, the lunar mass distribution failed to reproduce the spectral plots as described in Section 2.9. Choices for the mass distribution are Lunar, Interplanetary, and P/Comet Halley. The lunar mass distribution has more small particles compared to the other two while the interplanetary distribution has a pronounced silicate feature near 9μm.
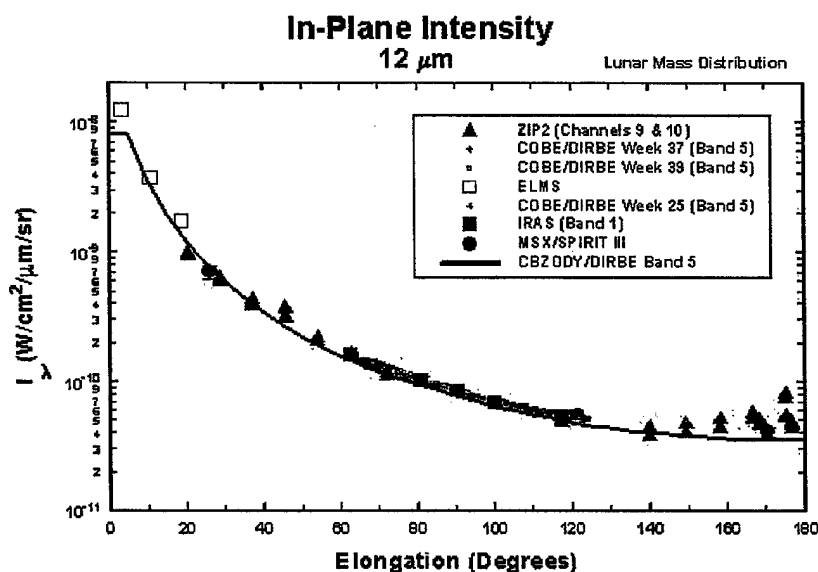
Figure 27: A 12μm fit to various datasets. This figure shows the CBZODY6 fit to various datasets which include ZIP2; ELMS; IRAS (Band 1); COBE/DIRBE (Band 5); and MSX/SPIRIT III (Bands A & C).
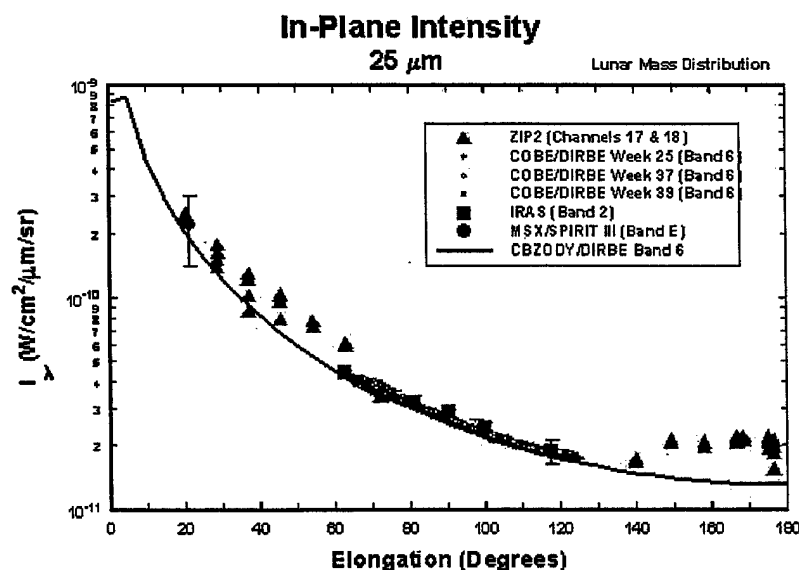
Figure 28: A 25μm fit to various datasets. This figure shows the CBZODY6 fit to various datasets which include ZIP2; IRAS (Band 2); COBE/DIRBE (Band 6); and MSX/SPIRIT III (Band E).

2.9 Characterization of the Dust Composition.

The initial dust particle composition used in the CBZODY code was astronomical silicate. Comparisons to datasets such as COBE and Infrared Space Observatory (ISO) quickly revealed that this was an inadequate model for the dust composition. We investigated varying particle mixtures for the zodiacal dust cloud. Figure 29 shows the results of using particle mixtures of astronomical silicate and graphite of varying proportions. Of primary concern was the fact that the astronomical silicate emissivity function under-predicted the flux for the COBE/DIRBE band 4 (4.9μm). We decided that the best fit was obtained by using a mixture of 65% astronomical silicate and 35% graphite with an interplanetary dust distribution. This ratio raised the contribution at band 4 but did not significantly alter the band 5 and band 6 flux. It also retains a silicate emission feature at 9μm. However, these changes require that the COBE dataset be rerun to obtain the best parameter fit.

Figure 30 show a direct comparison between Reach et al.'s (1996) ISO stare spectrum and the CBZODY6 model. Two model results are shown, astronomical silicate with a lunar dust distribution and a mixture of 70% astronomical silicate and 30% graphite with an interplanetary mass distribution. While neither model spectrum matches the ISO data, the 70/30 mixture has the benefit of increased intensity at short wavelengths. While at 15μm the lunar distribution shows a better match to the data, the two distribution merge near 20μm and become indistinguishable in COBE/DIRBE Band 6 (25μm).

Figure 31 shows the CBZODY fit to spectral data spanning 0.2 μm to 100 μm. This is a compilation of data from many different small rocket, balloon, and satellite data. Considering the data sets are taken decades apart with different calibration schemes, the agreement is quite good.

Figure 32 shows the effects of a 70% astronomical silicate and 30% graphite mixture on the overall spectral energy distribution. The 4.9μm region is enhanced compared to earlier figures.
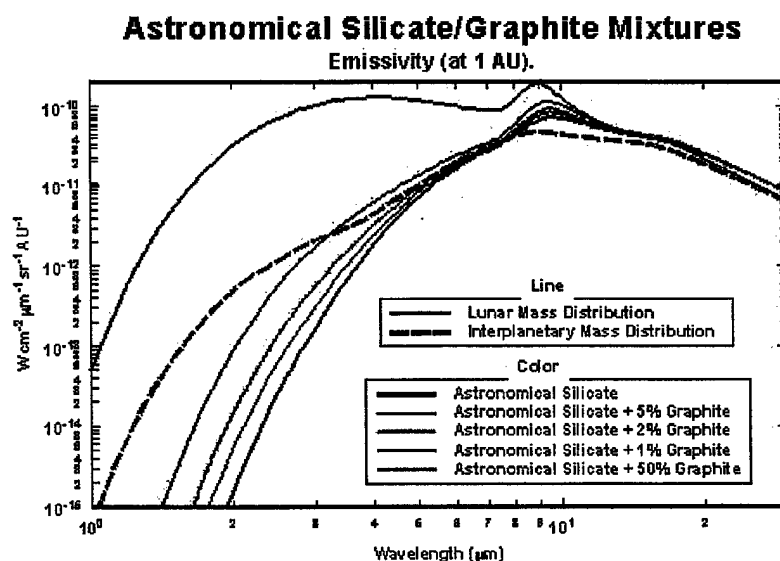
Figure 29: Zodiacal cloud particle mixtures. Different mixtures of astronomical silicate and graphite with two mass distributions.

CBZODY6 comparison to ISO Stare

Elongation = 104.3°

Iso Feb. 27,1998 2:33:07 PM
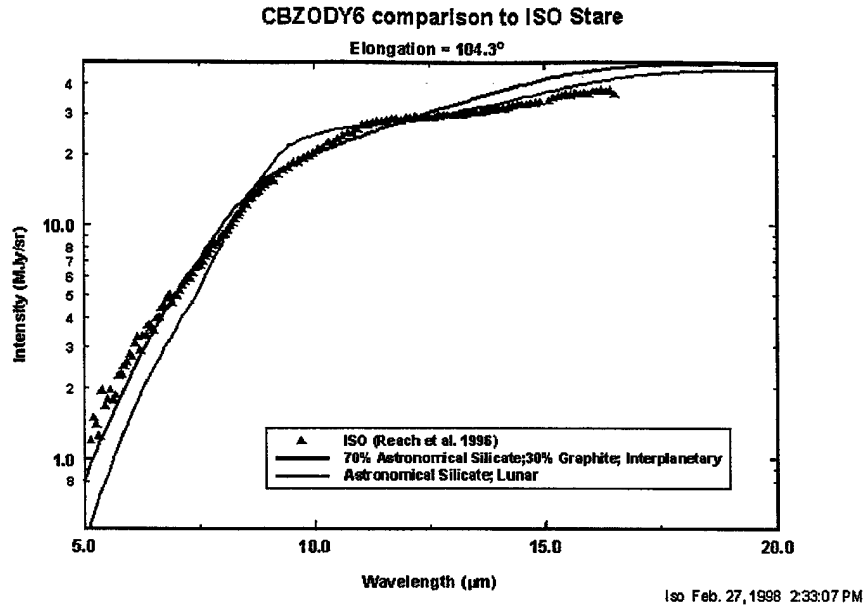
Figure 30: Comparison to ISO high spectral resolution data. The fits obtained using astronomical silicate and a lunar mass distribution and a 70/30 astronomical silicate/graphite mixture and an interplanetary mass distribution. The 70/30 mixture shows an improved fit at short wavelengths.

CBZODY Model to data comparison

Ecliptic Plane Crossing at e=90°
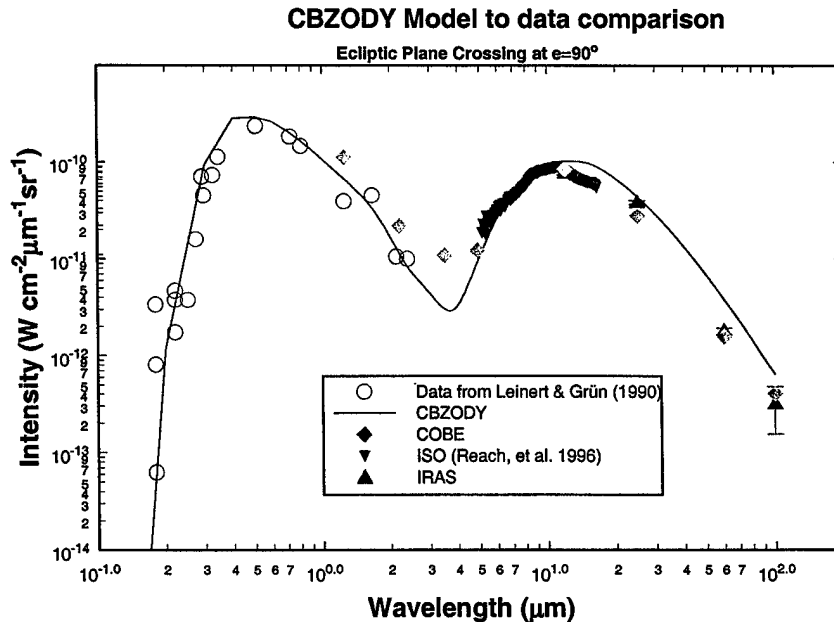
Figure 31: Spectral fit of the CBZODY model. The solid line is the CBZODY model prediction for the range of 0.1 to 100μm. Sources of data are COBE/DIRBE Bands 1 through 8, IRAS Bands 1 through 4, ISOPHOT data between 5 and 16μm (Reach et al. 1996), and various small rocket, balloon, and satellite data (Leinert and Grün, 1990).

30

70% Astronomical Silicate, 30% Graphite; Interplanetary Mass

Ecliptic Plane Crossing at e=90°

Spectral2 Feb. 28, 1998 1:43:49 PM
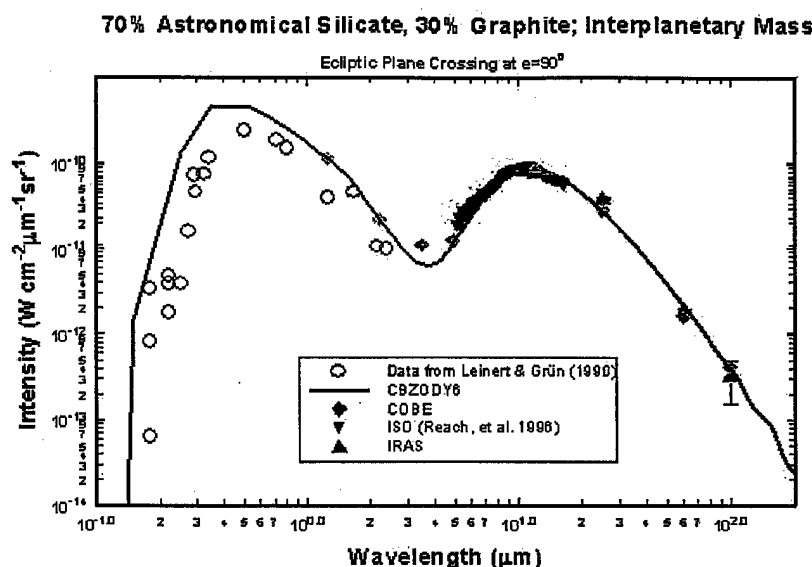
Figure 32: The spectral energy distribution for a 70% astronomical silicate 30% graphite interplanetary mixture. Note the increased flux at 4.9μm. compared to Figure 31.

2.10 Improvements to the CBZODY Dust Band Model.

To enhance the model we adopted the migrating band model of Reach et al. (1997). However, unlike Reach et al. we treat the bands as purely additive terms and do not perform Fourier filtering to obtain band profiles. As additive terms, Reach et al.'s original profiles are much too broad. Additionally, looking at the COBE pseudo-scans revealed that Reach's ascending nodes of the bands did not match the observed data. Originally, the seven band structures had ascending nodes of 86° and 92°. Since the ascending node is part of the dust density calculation, we set all ascending nodes to 0°. The ascending node of the dust cloud is used for the dust bands also. Likewise, some of Reach's band parameters were changed. Table 9 shows the original parameters used by Reach. Table 10 shows the parameters modified for the CBZODY6 code to enhance the fit compared to the observed data.

Table 9: Reach's original table of band parameters.

Parameter	Themis	Koronis	Nysa	Flora	Eos	Eunomia	Maria
$i_{latitudinal}$[1]	1.209	1.855	2.695	4.457	8.612	11.613	13.986
$i_{orbital}$[2]	0.82	0.82	0.82	0.76	0.76	0.76	0.76
n_0	0.25	0.43	0.4	0.8	1.0	0.26	0.22
$\delta\zeta$	1.219	1.978	2.624	3.570	9.184	12.388	14.905
v_i	0.318	0.079	0.370	0.533	0.109	0.094	0.050
p_i	4	4	4	4	4	4	4
R_0 (AU)	3	3	3	3	3	3	3
Ω	86°	86°	86°	86°	92°	92°	92°

[1] the latitudinal inclination is the observed displacement from the ecliptic plane in the sky.
[2] the orbital inclination is the orbit's tilt.

31

Table 10: The band parameters as currently used in CBZODY6.

Parameter	Themis	Koronis	Nysa	Flora	Eos	Eunomia	Maria
$i_{latitudinal}$[1]	1.209	1.855	2.695	4.457	8.612	11.613	13.986
$i_{orbital}$[2]	0.82	0.82	0.82	0.76	0.76	0.76	0.76
n_0	0.60	0.30	0.4	0.8	0.6	0.26	0.22
δ_ζ	1.219	1.978	2.624	3.570	9.184	12.388	14.905
v_i	1.272	0.316	1.480	2.132	0.436	0.376	0.200
p_i	4	4	4	4	4	4	4
R_0 (AU)	3	3	3	3	3	3	3
Ω	0°	0°	0°	0°	0°	0°	0°

[1] the latitudinal inclination is the observed displacement from the ecliptic plane in the sky.
[2] the orbital inclination is the orbit's tilt.

Reach et al. define the migrating band model number density function with a functional form of:

$$n(r,\zeta) = n_0 \frac{R_0}{r} e^{-\left(\frac{\zeta}{\delta_\zeta}\right)^6} \left[1 + \frac{1}{v_i}\left(\frac{\zeta}{\delta_\zeta}\right)^{p_i}\right]$$

Our modification to this is:

$$n(r,\zeta) = n_0 \frac{R_0}{r} e^{-\left(\frac{\zeta}{\delta_\zeta}\right)^{12}} \left[1 + \frac{1}{v_i}\left(\frac{\zeta}{\delta_\zeta}\right)^{p_i}\right]$$

where:

$$\zeta \equiv \frac{z}{r},$$

z = out of plane distance (AU), and

r = heliocentric, in-plane distance (AU).

The only change to the form is that the first exponent is changed from 6 to 12, which has the effect of narrowing the bands, thus decreasing the potential emission seen at high ecliptic latitudes. All other changes are reflected in changes to the band parameters. Figure 33 shows the two band profiles for a single band Eos.

Figures 34 and 35 show the two different number density functions for the Eos family. While both have similar structure, the version used in this report is narrower, producing less flux at the poles.
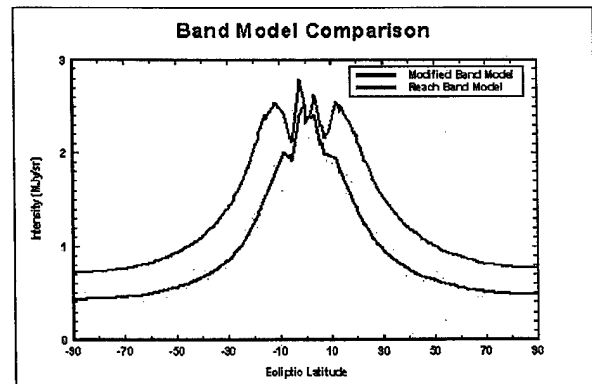
Figure 33: Comparison of the Eos band for modified band model and Reach's original model. The modified version shows a much narrower profile.

32

Number Density
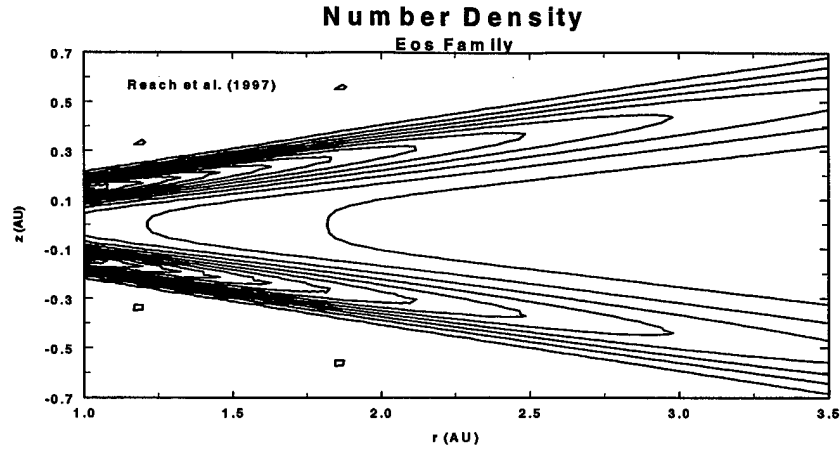
Eos Family

Figure 34: Reach model number density cross section. The number density of the Eos family is shown in the rz plane using the Reach et al. (1996) migrating band model.

Number Density
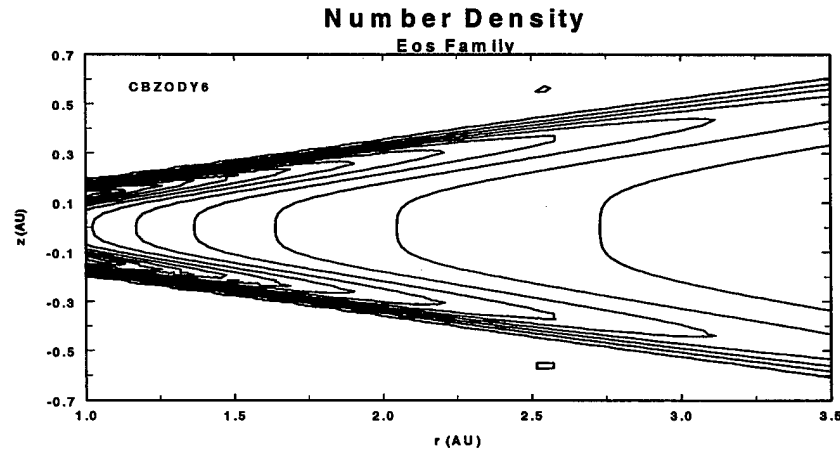
Eos Family

Figure 35: CBZODY number density cross section. The number density of the Eos family is shown in the rz plane using a modified form of the Reach et al. (1996) migrating band model.

2.11 Two-Plane Model and the Solar Ring

Table 11 gives the CBZODY parameters for a two-plane model. The transition region between planes is from 0.96 to 1.08 AU.

Table 11: CBZODY6 parameters determined from COBE/DIRBE CIO data.

	Inner Region	Outer Region
ν - power law	1	1
Γ (AU) - scale height	0.365	0.275
Ω - ascending node	86.391°	76.939°
i - orbital inclination	3.3°	2.9°
N_{0cloud} - (x 10^{-17} particles/cm^3)	1.41	1.82
N_{0bands} (x 10^{-17} particles/cm^3)	0.045	0.034

33

Figures 36 and 37 show the results of a simple smoothing technique developed under this project. These figures show a cross section through the rz plane. The original implementation (Figure 36) used a sharp discontinuity at the transition region that led to artifacts in the residuals. Our modification was to implement a smoother transition that begins at 0.96 AU and ends at 1.08 AU. There is a linear decrease (or increase) from the inner value to the outer value. The transition zone is thus 0.12 AU. Three values are separately modified in the transition zone: the HWHM (Γ); the dust cloud density normalization (N_{0cloud}); and the dust bands density normalization (N_{0band}).

An artifact of the smoothing can be seen in Figure 37. There is a density enhancement behind the orbit of Earth which represents a "Ring" of slightly enhanced density that completely surrounds the Sun.
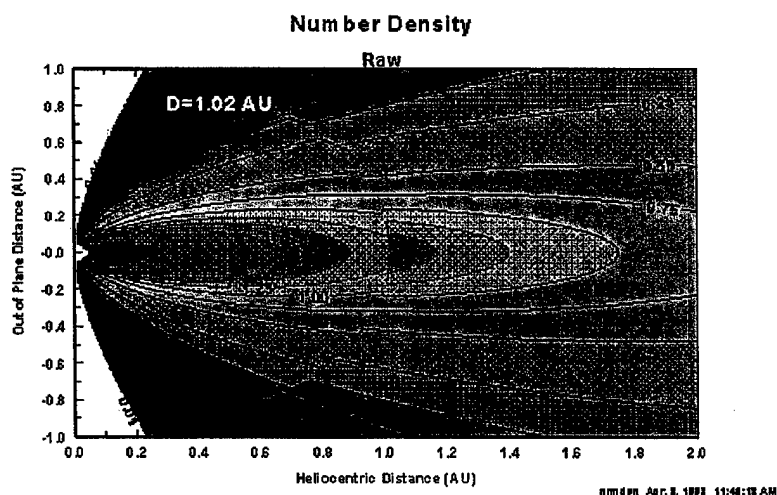
Figure 36: Dust number density cross section. A plot in the rz plane shown the dust density function. The break in the parameter set (two planes) is clearly visible at 1.02 AU.
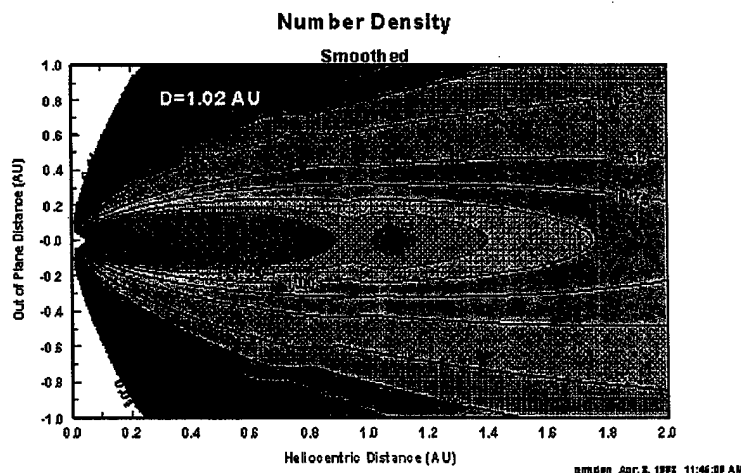
Figure 37: Smoothed dust number density cross section. A plot the same as Figure 36 after applying a smoothing function between 0.96 and 1.08 AU to lessen the discontinuity between planes. The dust enhancement between 1.0 and 1.2 represent a ring that completely encircles the Sun.

2.12 South Ecliptic Pole (SEP)

Figure 38 represents the model fits to the South Ecliptic Pole (SEP) with data taken from the COBE weekly sky average datasets (the pole is at a constant elongation of 90° and does not have problems like those discussed in Section 2.8). Bands 1 through 6 are represented. The model fits consist of two components, CBZODY and the SKY model (Cohen 1993). The SKY contribution is significant below 12μm. Bands 4, 5, and 6 are strongly influenced by the annual variations of the zodiacal cloud. The match at bands 4 and 5 show the influence of the 65/35 astronomical silicate/graphite mixture.

Figure 39 is another view of the SEP. All of the COBE SEP observations were averaged to obtain single values. In addition, MSX observations of the SEP were included.
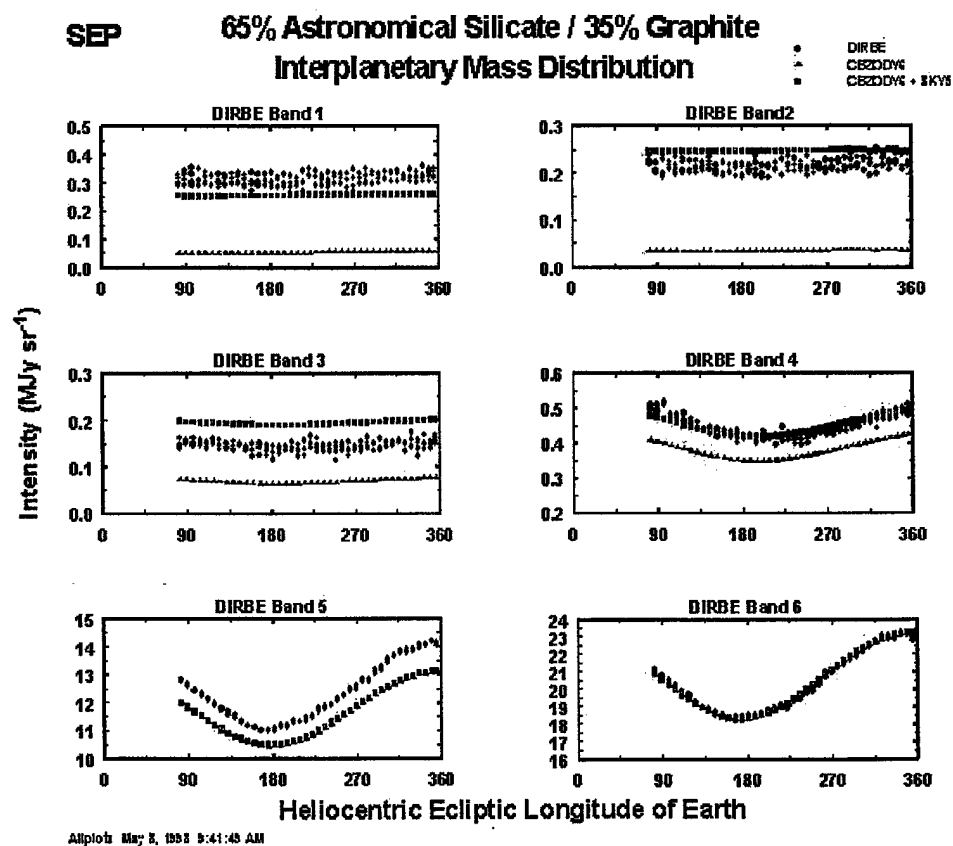
Figure 38: Model fits to the South Ecliptic Pole (SEP). We have included two components to the SEP flux, CBZODY6 and the SKY5 model. The stellar contribution is significant for bands 1 through 4.

35
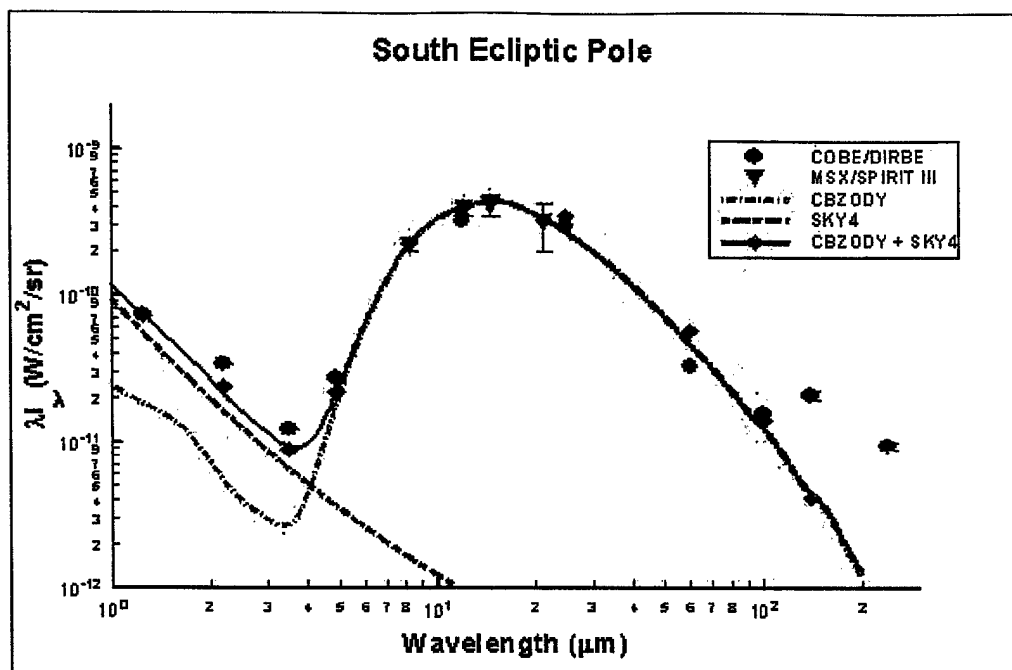
Figure 39: CBZODY and SKY4 over the DIRBE bands. The averaged COBE/DIRBE observations of the SEP compared to CBZODY6, SKY4, and a combined CBZODY/SKY model.

2.13 COBE CIO Data

In mid 1997, new COBE data products became available. Figure 40 is an example of the Calibrated Individual Observation (CIO) data. It is a volumous data product encompassing every piece of data taken, time ordered and calibrated. Each CIO file is around 50 MB and there is a file for each day of observation. Because of the COBE scan pattern, the entire sky was not covered daily. Small data gaps are seen over the entire sky. Since the data are time ordered and the location of each pixel is described in the data, it is a straight forward, but time consuming, chore to model every pixel individually.

Figure 41 shows an in-plane comparison of COBE CIO 90166 at four COBE/DIRBE bands; band 4 (4.9μm), band 5 (12μm), and band 6 (25μm). The in-plane comparison shows the validity of using the $1/r$ assumption for the in-plane dust density. The figure shows relatively good agreement. The small overestimation is attributable to composition assumptions and not to the density distribution.
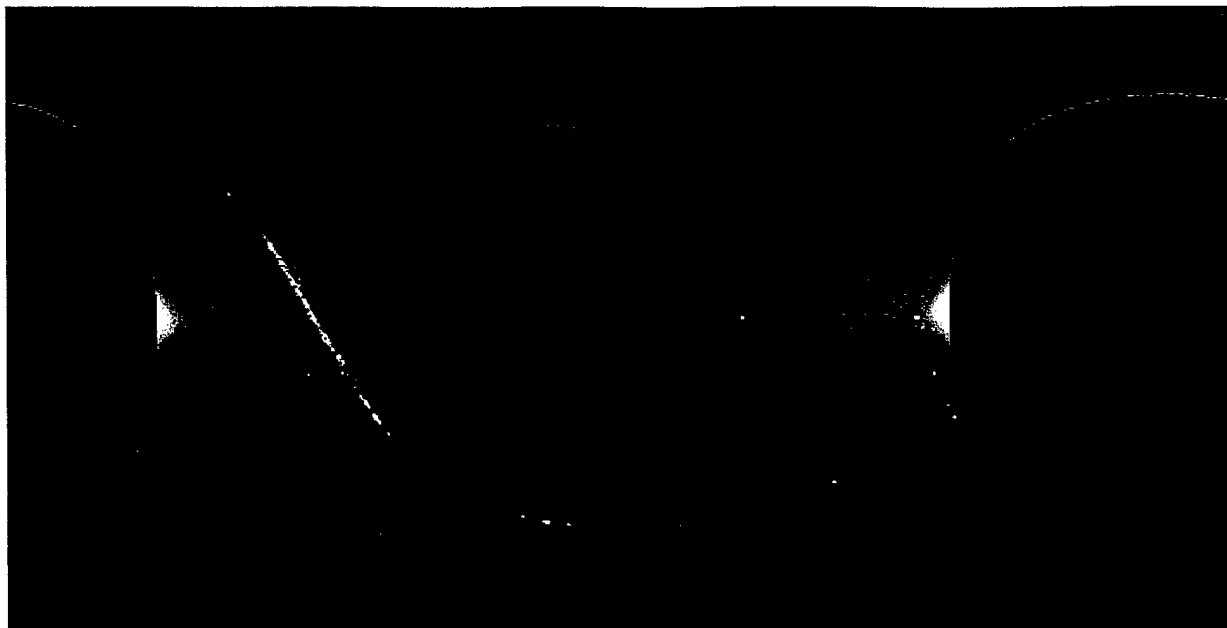
Figure 40: COBE/DIRBE Band 5 CIO 90100. Sample of one of the CIO daily datasets. Note the number of data gaps represented by the black dots over the entire image.
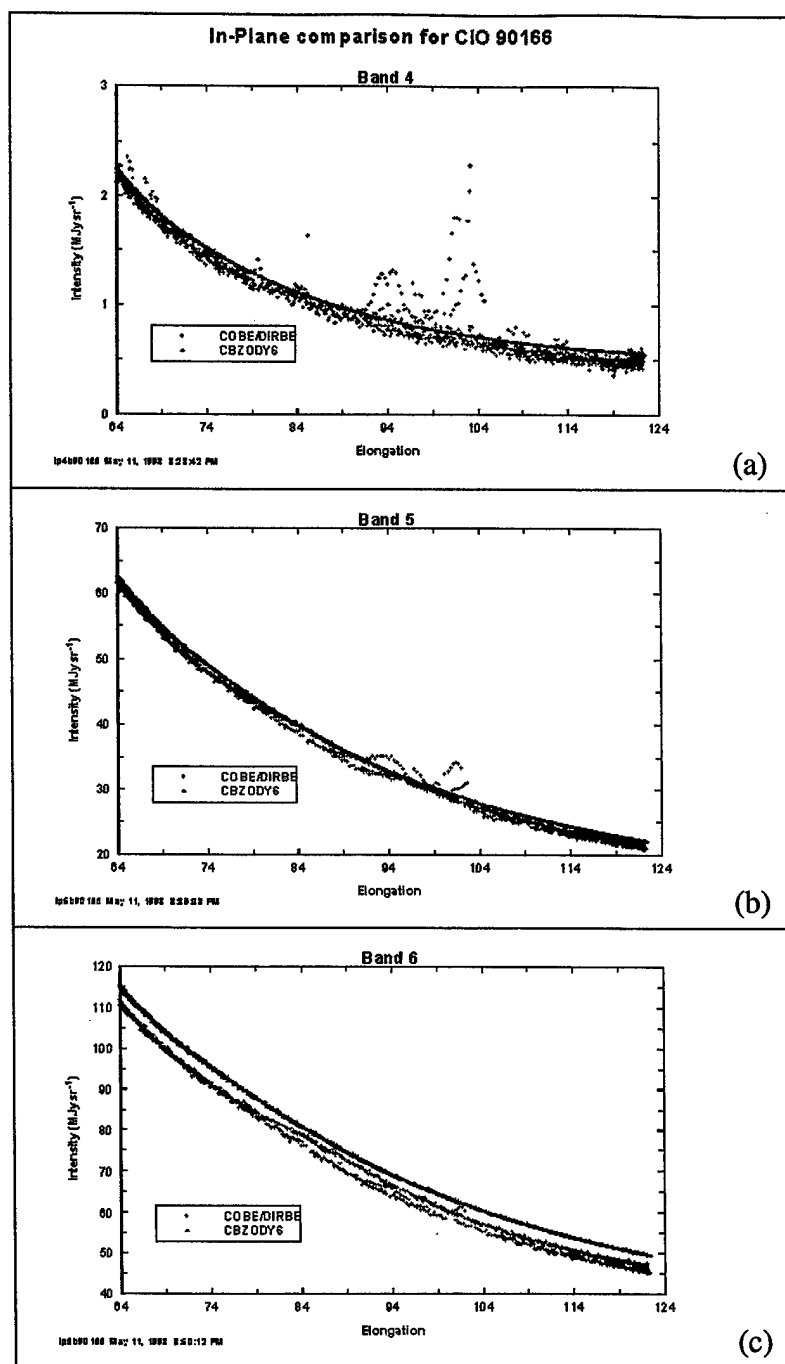
Figure 41: In-plane comparisons in three COBE/DIRBE bands. (a) Band 4, 4.9 μm; (b) Band 5; 12 μm; and (c) Band 6, 25 μm.

Figure 42 shows pseudo-scans similar to the IRAS pole-to-pole scans. The pole-to-pole scans show the out-of-plane dust density distribution. CBZODY6 uses a Lorenztian profile that shows an excellent agreement to the data.

Figure 43 shows residual plots from COBE/DIRBE bands 4, 5, and 6. The residuals are the sky image after the zodiacal has been removed. Some errors still remain in the band structure and need to be addressed in the future.
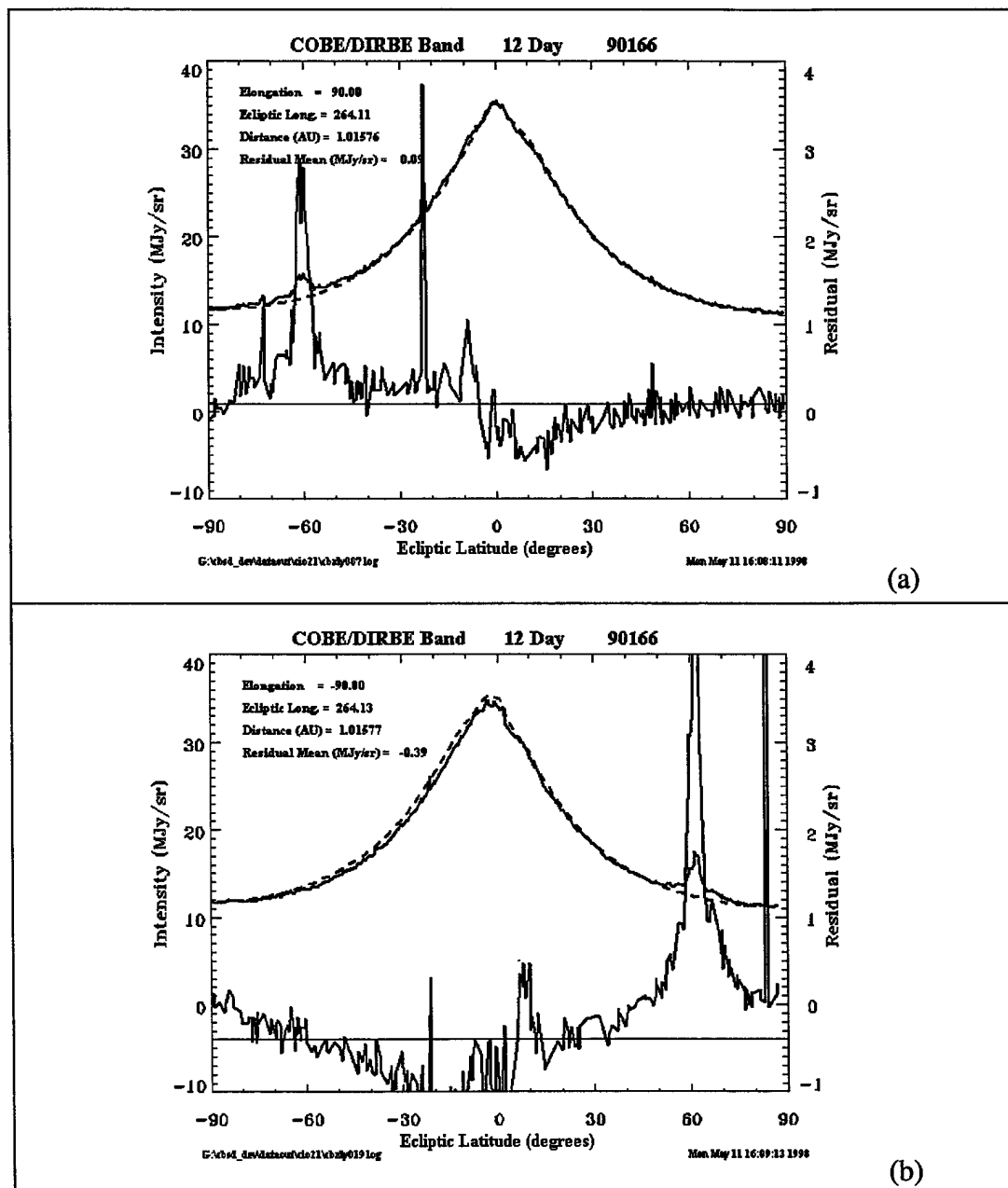
Figure 42: COBE pseudo-scans. These scans are taken from the COBE CIO data and mimic the IRAS pole-to-pole scans. Here the latitudinal profile can be observed. (a) Leading, (b) trailing.
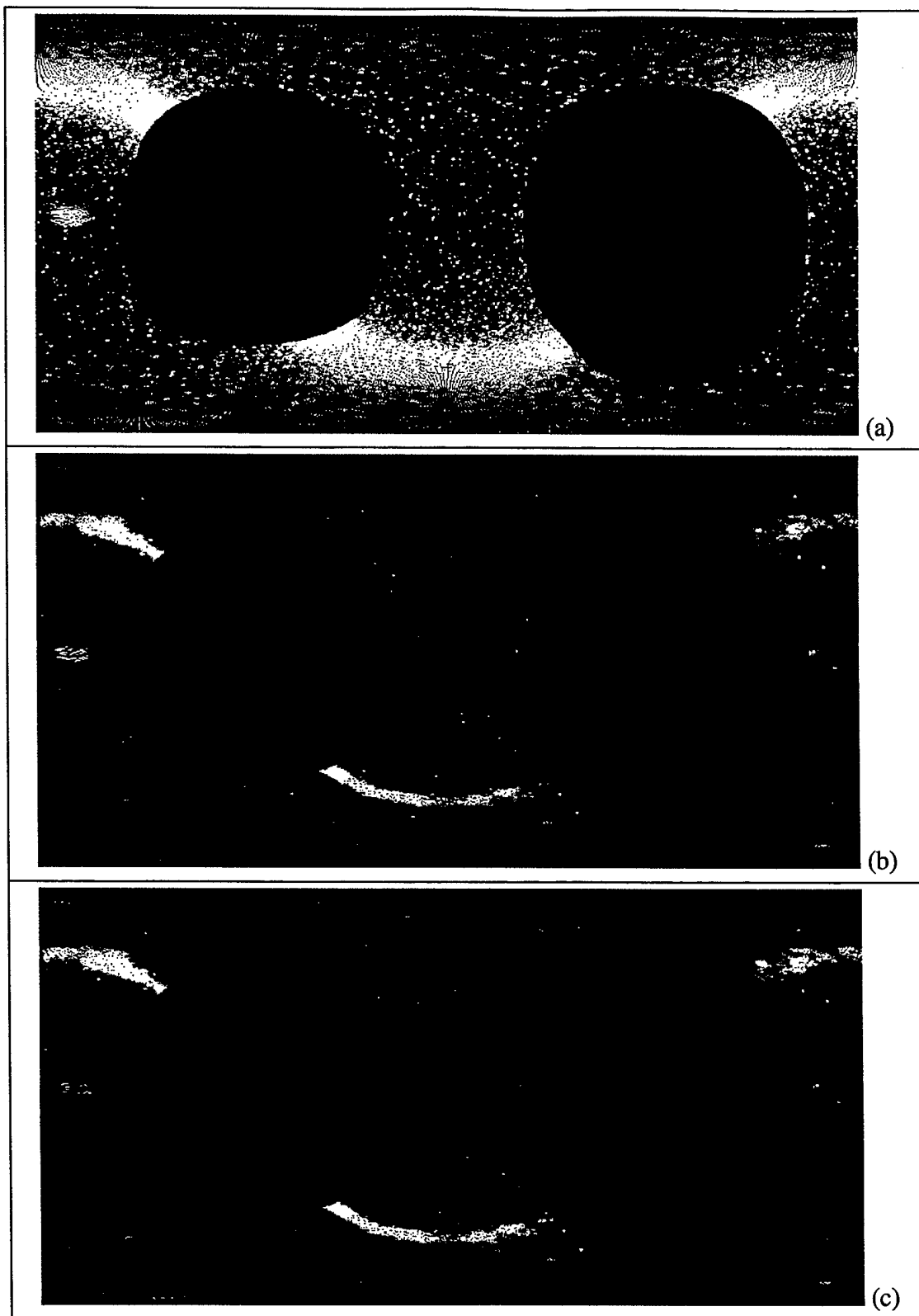
Figure 43: Residual plots for CIO 90166. (a) COBE/DIRBE Band 4. (b) COBE/DIRBE Band 5. (c) COBE/DIRBE Band 6. For all, white >5 MJy/sr and black < -5 MJy/sr.

2.14 Implementation of the ATLAS9 Solar Spectrum Model

In conjunction to the IMPS study, predictions of asteroid fluxes and magnitudes were being made. Slight discrepancies were found in the results. The primary cause seemed to be problems with the adopted solar spectrum. We had been using a Kurucz model run from his ATLAS8 code that contained a few hundred atomic and molecular lines. This was found inadequate. We have since adopted a solar spectrum of several million lines as shown in Figure 44. Table 12 shows the comparison between observed quantities and the ATLAS8 and ATLAS9 spectra. To properly match the observations, we applied the following correction to the spectral data:

$$K_\lambda \cdot 1.034 - 0.315\, Wcm^{-2}\mu m^{-1}sr^{-1}$$

This gives adequate agreement with observations as detailed in Table 12.
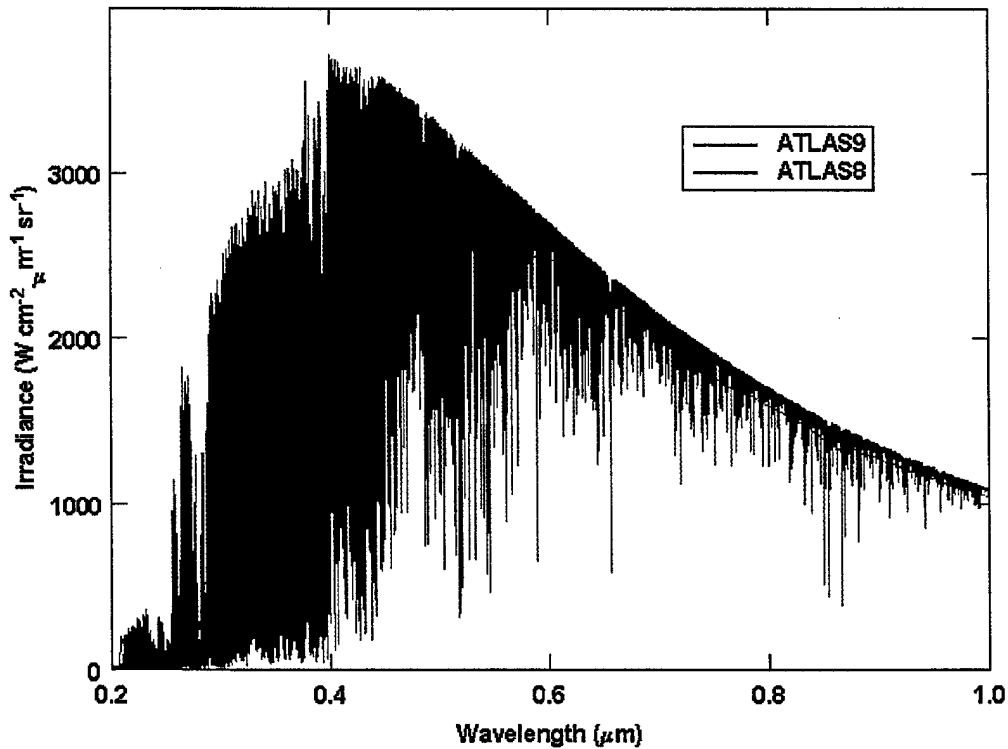
Figure 44: Solar spectrum comparison. The two solar spectra used in CBSD are shown. The older, ATLAS8, spectrum has only a few hundred spectral lines. In comparison the ATLAS9 spectrum has several million.

Table 12: A comparison of observations with predictions from ATLAS8 and ATLAS9.

	Reference Value	Kurucz (ATLAS9)	CBSD (ATLAS8)	CBSD (Renormalized ATLAS9) [1]
V	-26.762[a]	-26.726	-26.687	-26.762
Solar Constant (W/m²)	1373[b]	1369*	1383	1373
B-V	+0.65[c]	+0.663	+0.581	+0.663
U-B	+0.13[c]	+0.173	+0.09	+0.173
U-V	+0.78[c]	+0.836	+0.671	+0.836
V-R	+0.52[c]	+0.516	+0.502	+0.516
V-I	+0.81[c]	+0.894	+0.886	+0.895

[a] Campins, Rieke, & Lebofsky (1985)
[b] Neckel & Lab (1984)
[c] Allen, Astrophysical Quantities (1973)
* Kurucz (1999)
[1] $K_\lambda \cdot 1.034 - 0.315 Wcm^{-2}s^{-1}sr^{-1}$

2.15 CBZODY6 Phase Function

The CBZODY6 code has two choices for a scattering phase function; a Henyey-Greenstein function created by Hong (1985) or an expansion into Legendre polynomials of Murdock and Price (1985). Functionally these two are very different. Hong's function is:

$$\sigma(\theta) = 0.665 \cdot H(0.70,\theta) + 0.330 \cdot H(-0.20,\theta) + 0.005 \cdot H(-0.81,\theta)$$

$$H(g,\theta) = \text{Henyey} - \text{Greenstein phase function}$$

$$H(g,\theta) = \frac{1-g^2}{(1+g^2 - 2g\cos\theta)^{1.5}} ,$$

while Murdock and Price use:

$$\sigma(\theta) = \left\{ 1 + 1.30\cos\theta + 1.30\left(\frac{1}{2}(3\cos^2\theta - 1) \right) \right\}$$

Figure 45 compares the two phase functions. The Hong function is much steeper for short wavelengths and is the recommended phase function for most applications.
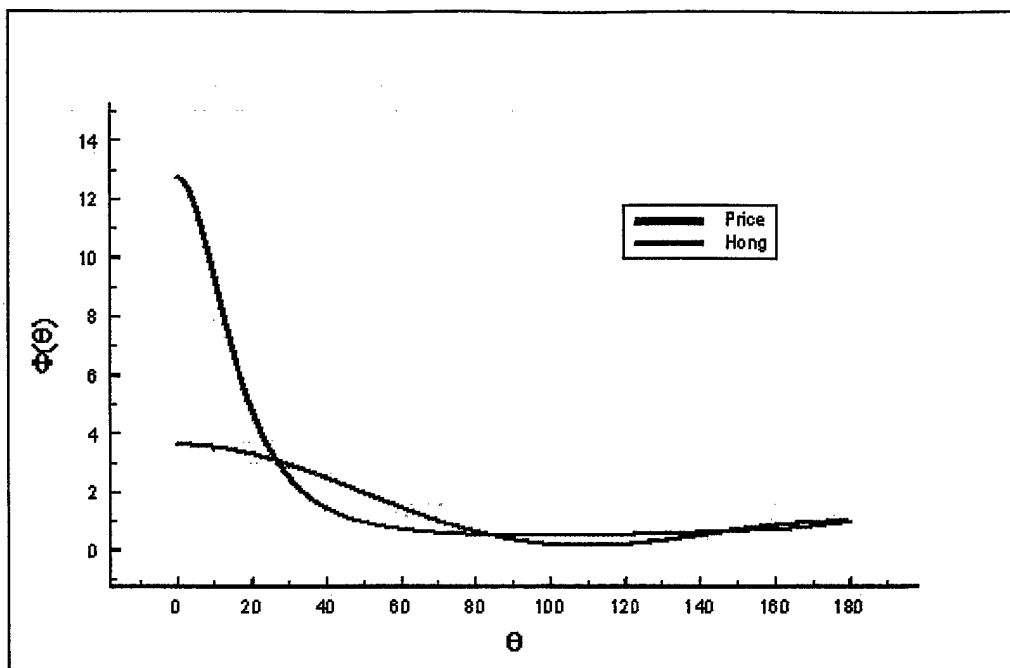
Figure 45: Phase functions. Comparison of the Legendre phase function of Murdock and Price (1985) (Price) and the Henyey-Greenstein phase function of Hong (1985) (Hong).

Figure 46 is an enlargement of the region $0 < \Phi(\theta) < 2$. It shows the strong upturn of backscattering around 180° ($\cos(\theta) = -1$), the antisolar point.
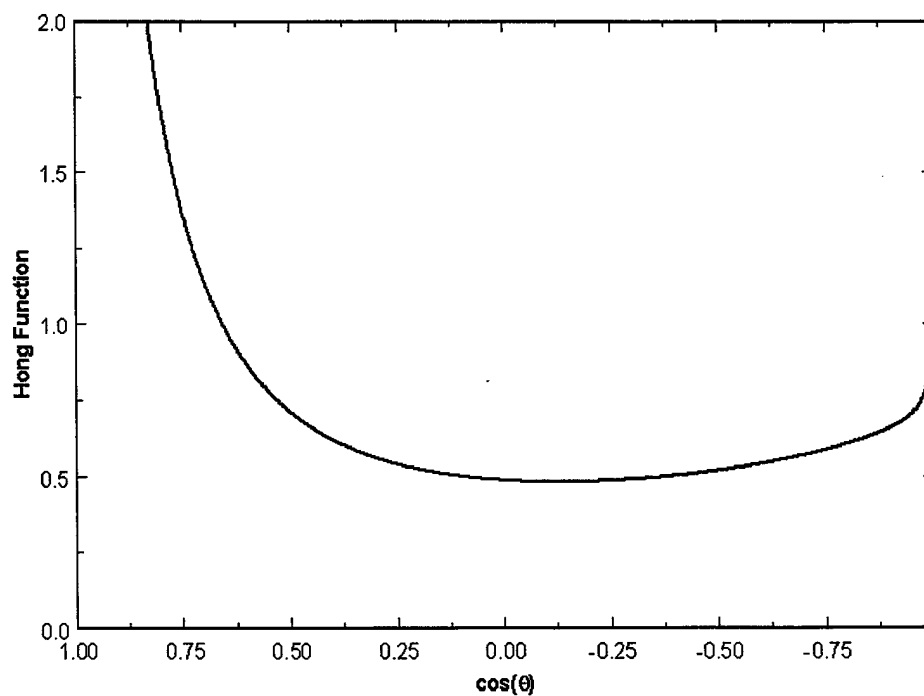
Figure 46: Hong Phase function: A zoomed image showing the backscatter at the antisolar point.

43

2.16 Earth Ring

Dermott et al (1994) also reported the Earth might be a shepherd of a Sun circular ring. We have included a Ring model similar to Reach et al. (1995). Our ring is the sum of two three-dimensional gaussians, one leading and one trailing the Earth. The ring model has been defined as a two 3-dimensional Gaussian clouds, one leading and one following the Earth in the same orbital plane. We define the leading cloud's position as:

$$\begin{pmatrix} x_l \\ y_l \\ z_l \end{pmatrix} = \begin{pmatrix} R_\oplus \cos(\ell_\oplus + \Delta\ell_{leading}) \\ R_\oplus \sin(\ell_\oplus + \Delta\ell_{leading}) \\ 0 \end{pmatrix}$$

where:

$R_\oplus$ = the heliocentric distance of the Earth

$\ell_\oplus$ = the heliocentric ecliptic longitude of Earth

$\Delta\ell_\oplus$ = the angular separation between the cloud and the Earth

Likewise for the following cloud:

$$\begin{pmatrix} x_f \\ y_f \\ z_f \end{pmatrix} = \begin{pmatrix} R_\oplus \cos(\ell_\oplus + \Delta\ell_{following}) \\ R_\oplus \sin(\ell_\oplus + \Delta\ell_{following}) \\ 0 \end{pmatrix}$$

We define the angle between the Earth-cloud centers and the vernal equinox:

$$\tan\alpha = \frac{y_o - y_{(l \, or \, f)}}{x_o - x_{(l \, or \, f)}}$$

with (x_o, y_o, z_o) being the observer's coordinates.

The position of a volume element, $(x_{los}, y_{los}, z_{los})$, relative to the center of the cloud is then:

$$\begin{pmatrix} x_v \\ y_v \\ z_v \end{pmatrix} = \begin{pmatrix} (x_{los} - x_{(l \, or \, f)})\cos\alpha + (y_{los} - y_{(l \, or \, f)})\sin\alpha \\ -(x_{los} - x_{(l \, or \, f)})\sin\alpha + (y_{los} - y_{(l \, or \, f)})\cos\alpha \\ 0 \end{pmatrix}$$

The number density is finally:

$$N = \frac{1}{r^v}\exp\left(-\frac{1}{2}\left(\frac{x_v}{\delta x}\right)^2\right)\exp\left(-\frac{1}{2}\left(\frac{y_v}{\delta y}\right)^2\right)\exp\left(-\frac{1}{2}\left(\frac{(z_{(l \, or \, f)} - z_{los})}{\delta z}\right)^2\right)$$

were we are using $(\delta_x, \delta_y, \delta_z)$ as the half-widths of the cloud. The size and density enhancements are parameters input through the cbzparms.dat file. At this time, we do not see the need for the inclusion of the ring. This is in part due to the inherent ring in the model. As shown in Section 2.11, the two-plane model introduces a ring just outside of Earth's orbit.

3. Validation

3.1 Parameter Sets

This section enumerates the final parameter set used in the deployment of the CBZODY6 code. Parameters are defined internally, in data statements, or in the CBZPARMS.DAT file, which was a convenient method of testing new parameters without recompiling the code.

3.1.1 CBZPARMS.DAT Parameter Set

Table 12 shows the current list of parameters in the CBZPARMS.DAT file. While this is an ASCII file, it is not to be edited by the users. These parameters signify the "best fit" to the ensemble of data presented. We have found that by adjusting the parameters it may be possible to improve the fit to a certain dataset, but this tends to worsen the fit to other datasets. These parameters represent our best estimate based on all the tradeoffs between datasets.

Table 12: Adopted parameters in CBZPARMS.DAT file.

```
nu         -- power index
        1.000000000000000
hwhm1      -- hwhm inner dust plane
        0.371
znode1     -- ascending node inner dust plane
        83.009
zincl1     -- inclination inner dust plane
        3.30
n0thm1     -- Normalization density, inner plane
        1.47
n0bnd1     -- Normalization density, bands, inner plane
        0.049
break1     -- break point between planes
        1.02
hwhm2      -- hwhm middle dust plane
        0.281
znode2     -- ascending node middle dust plane
        78.256
zincl2     -- inclination middle dust plane
        3.30
n0thm2     -- Normalization density, middle plane
        1.68
n0bnd2     -- Normalization density, bands, middle plane
        0.034
break2     -- break point between planes
        4.000000000000000
hwhm3      -- hwhm outer dust plane
        0.267000000000000
znode3     -- ascending node outer dust plane
        67.540000000000010
zincl3     -- inclination outer dust plane
        1.924000000000000
n0thm3     -- Normalization density, outer plane
        1.605000000000000
n0bnd3     -- Normalization density, bands, outer plane
        0.027524312293892
n0a2       -- scattering normalization        0.0070
        6.58e-13
albedo     -- dust albedo
        0.300000000000000
offset     -- DC offset
        0.000000000000000
sigma      -- time constant
        250.000000000000000
fscale     -- scale factor
        0.000000000000000
again      -- zero point gain
        1.000000000000000
ring_nrm -- leading and trailing ring Normilization density
        0.000000000000000        0.000000000000000
ring_ang -- leading and trialing ring-Earth separation (deg)
        2.090700000000000        4.480000000000000
ring_wl  -- leading ring characteristic widths (AU)
        0.354231000000000        0.018712000000000        0.074498000000000
ring_wt  -- trailing ring characteristic widths (AU)
        0.009725000000000        0.015477000000000        0.009284000000000
n0band     -- band parameters
  0.50000  0.20000  0.35000  0.75000  0.65000  0.30000  0.24000
n0bndsct -- band scattering
  1.0e-15
```

3.1.2 Band parameters

The final set of migrating band parameters used for the model validation is presented in Table 13. Figure 47 gives the latitudinal profiles of the dust associated with the 7 asteroid families.

Table 13: Modified migrating band parameters.

Parameter	Themis	Koronis	Nysa	Flora	Eos	Eunomia	Maria
$i_{latitudinal}$[1]	1.209	1.855	2.695	4.457	8.612	11.613	13.986
$i_{orbital}$[2]	0.82	0.82	0.82	0.76	0.76	0.76	0.76
n_0	0.50	0.20	0.35	0.75	0.65	0.30	0.24
δ_ζ	1.219	1.978	2.624	3.570	9.184	12.388	14.905
v_i	1.272	0.316	1.480	2.132	0.436	0.376	0.200
p_i	4	4	4	4	4	4	4
R_0 (AU)	3	3	3	3	3	3	3
Ω	86°	86°	86°	92°	92°	92°	92°

[1] the latitudinal inclination is the observed displacement from the ecliptic plane in the sky.
[2] the orbital inclination is the orbit's tilt.
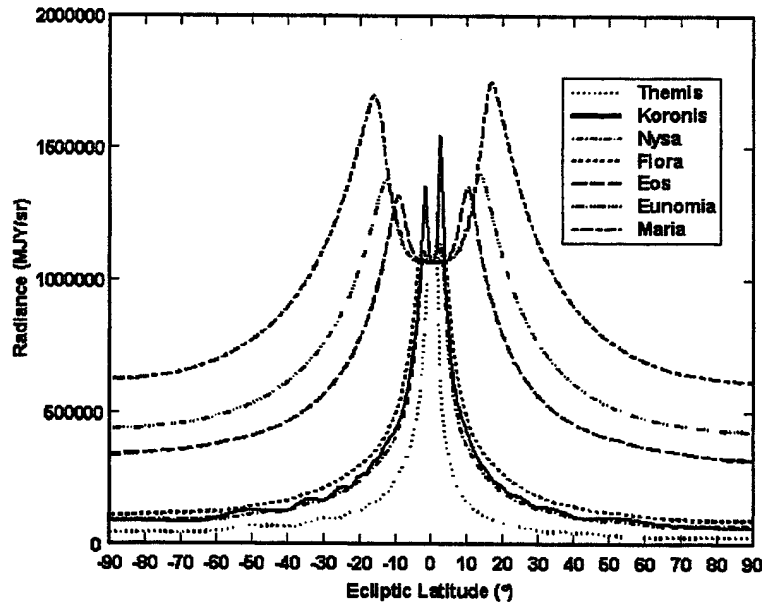
Figure 47: Latitudinal profiles of dust. Each of the seven dust families' profiles is shown for an elongation of 90°.

3.2 Results

CBZODY6 is a multi-spectral model capable of producing output between 0.2μm and 300μm. Any spectral response function may be used in that range. The precomputed volume emissivity function constrains the spectral resolution to either 0.01μm between 0.2 and 30μm, or 0.1μm between 0.2 and 300μm. The following sections detail comparisons between CBZODY6 and a variety of datasets and data types.

3.3 Reach et al. (1996) ISO Comparison

Reach et al. (1996) obtained a spectrum between 5 and 16.5μm using the Infrared Space Observatory (ISO) on 21 Jan 1996 and having a solar elongation of 104.3°. Their observation and the CBZODY6 fit to the data are shown in Figure 48. Reach et al. attempted to fit various constituent materials to the observation. They concluded that astronomical silicate with either an interplanetary or a lunar mass distribution had the best fit based on a reduced χ^2 goodness of fit. For our analysis, we found that a mixture of 65% astronomical silicate and 35% graphite provided an improved fit over astronomical silicate. For astronomical silicate we find a reduced χ^2 of 0.73, while the astronomical silicate and graphite mixture produced a reduced χ^2 of 0.41.

Overall, we conclude the fit to the data is quite good considering that the true chemical composition of the zodiacal dust is unknown. Attempts at single chemical compositions have proven to be inadequate. Our choice of graphite clearly shows and improvement in the short wavelength region of the ISO spectrum.

Between 10 and 16μm Figure 48 shows that neither astronomical silicate nor the astronomical silicate mixture can completely reproduce the observations. The search for a better match to the spectra will continue.

CBZODY6 comparison to ISO Stare

Elongation = 104.3°

Iso Jan 30, 2001 12:20:36 PM
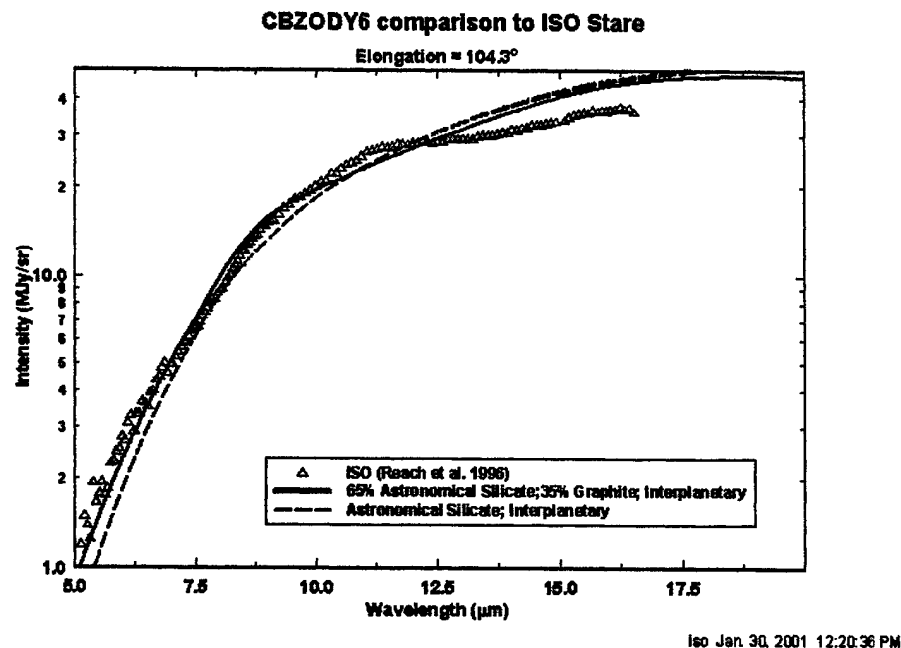
Figure 48: ISO spectrum of Reach et al. (1996). A comparison of the ISO spectrum compared to Astronomical Silicate and the Astronomical Silicate/Graphite mixture used in CBZODY6.

3.4 Briotta, et al. (1976) Small Rocket Data

At 10h 34m UT on 14 October 1975, a small rocket was sent aloft for observations of the zodiacal light (Briotta et al. 1976). A single observation in 12 channels at an elongation of 104° was obtained and is shown in Figure 49. This observation is very similar to the ISO observation obtained by Reach et al. This again shows the uncertainties in material composition of the zodiacal cloud.
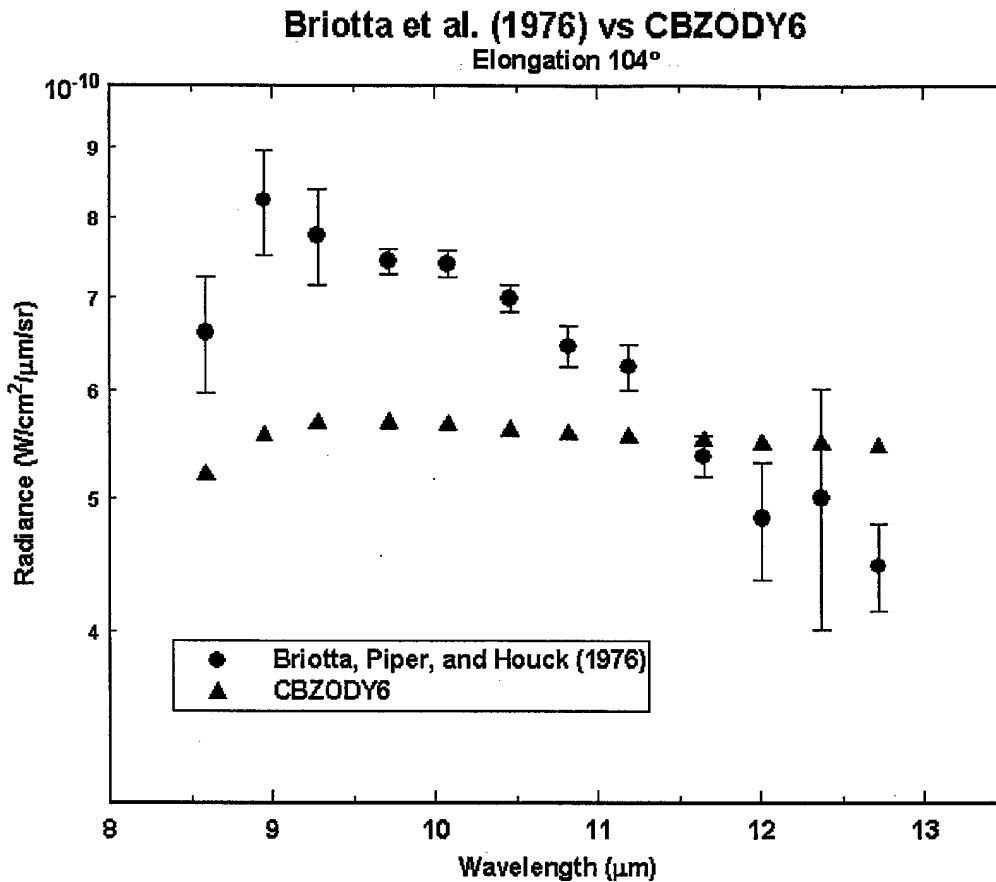
Figure 49: Spectral output of CBZODY compared to the spectrum obtained by Briotta et al. (1976). The CBZODY composition is 65% astronomical silicate and 35% graphite. There are discrepancies indicating that the true composition has not been determined.

3.5 Extended Spectral Comparisons

Figures 50 and 51 show the fit of the CBZODY6 model to a wide range of data covering visible to infrared ranges. The source of the visible data for these figures is the article of Leinert and Grün (1990). Leinert and Grün compiled several satellite and small rocket observations (Vela, Helios, etc.) and scaled them all to a 90° elongation. We have also included a single point from Leinert et al's (1997) sky brightness reference table at 0.5μm. Presumably, the satellite data were used to generate the latter table. The infrared data are from the IRAS, COBE, and MSX satellites. Figure 50 shows the spectral range from 0.2 to 30μm in spectral steps of 0.01μm. Figure 51 shows the extended range from 0.2 to 300μm in steps of 0.1μm.

Between 1 and 2μm we have overlap, and considerable variation, between the COBE data, Bands 1 (1.24μm) & 2 (2.4μm), and Leinert and Grün's dataset. We felt the COBE observations have been more carefully calibrated and hence are more trustworthy and we have given the COBE data a higher weight when performing the fit. As a result, as Figure 50 shows, the CBZODY6 model over-predicts the visible observations from Leinert and Grün by a

considerable amount. We can only speculate at a probable cause; calibration errors or, since the visible observations were all scaled to 90° elongation using an exponential law, the scaling law may not be exact.

The fits to the COBE, IRAS and MSX data are acceptable. As indicated by the ISO spectrum the 12 micron data or IRAS, COBE, and MSX will be slightly under predicted. There also seems to be calibration differences between COBE and IRAS at 25μm. Again, COBE data are considered of higher quality.

65% Astronomical Silicate, 35% Graphite
Interplanetary Mass Distribution

Ecliptic Plane Crossing at e=90°

Spectral2 Nov. 17, 2000 10:12:18 AM
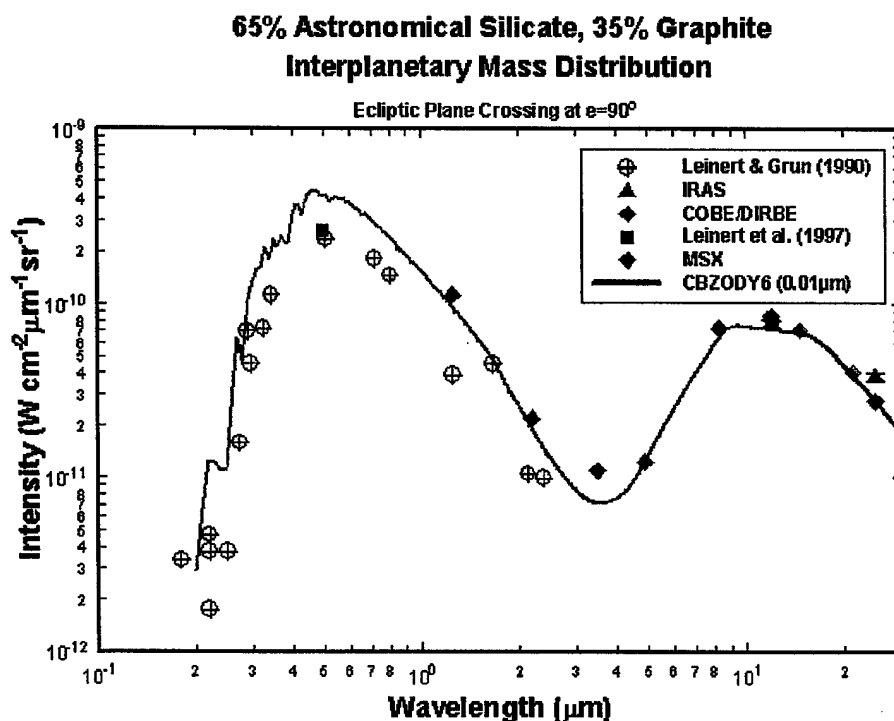
Figure 50: Zodiacal spectrum, solid line, compared to a variety of data sets for a 90° elongation. Between 1 and 3μm, discrepancies appear between the Leinert and Grün data and the COBE/DIRBE data. We chose to weight the COBE/DIRBE data more heavily in the fit.

Figure 51 is similar to Figure 50 except that it has a lower spectral resolution and an extended range. The lower spectral resolution leads to fewer spectral features in the scattered, visible, region of the spectrum. Figure 51 further shows that COBE bands 7 (60μm) and 8 (100μm) show reasonable agreement. Discrepancies are seen in Bands 9 (140μm) and 10 (240μm). This is expected since we have not included a cirrus (galactic dust) model.

50

**65% Astronomical Silicate, 35% Graphite
Interplanetary Mass Distribution**

Ecliptic Plane Crossing at e=90°

Legend:
- ⊕ Leinert & Grun (1990)
- ▲ IRAS
- ◆ COBE/DIRBE
- ■ Leinert et al. (1997)
- ◆ MSX
- —— CBZODY6 (0.1μm)
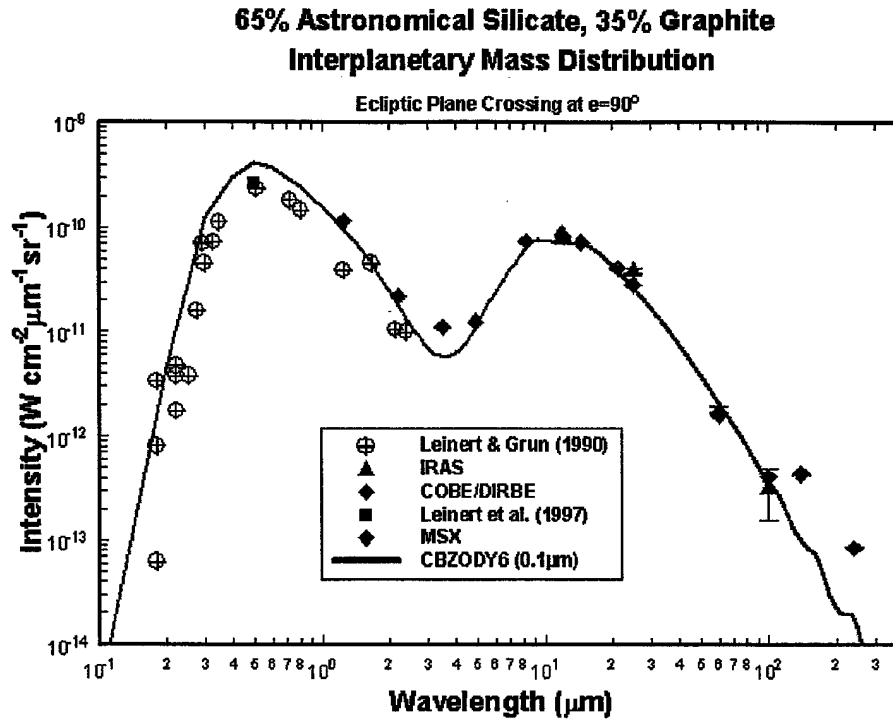
Spectral2 Nov. 17, 2000 11:58:19 AM

Figure 51: Similar to Figure 50 the zodiacal spectrum out to 300μm. The deviations at 140μm and 230μm between the model and COBE/DIRBE data are due to the lack of a galactic dust (cirrus) model and not errors in the zodiacal dust model.

3.6 Visible Zodiacal Table

Leinert et al. (1998) produced a table of zodiacal brightness for the visible, 0.50μm, their Table 37. That table, in units of 10^{-8} W m^{-2} sr^{-1} μm^{-1} has been reproduced in Table 14. However, assuming that Leinert et al.'s table was produced using the visible data of Figure 50 and 51, their table will be of lower quality than those produced by the CBZODY6 model which includes the higher quality COBE/DIRBE data. Table 15 is a listing of the solar elongation for each of the points in Table 14. We have reproduced tables similar to Leinert et al. in Tables 48, 49, 50, & 51. These tables give zodiacal brightness in units of 10^{-8} W m^{-2} sr^{-1} μm^{-1} for four time periods in the year: 21 March; 21 June; 21 September; and 21 December respectively. As expected, the brightness from CBZODY6 is higher than Leinert et al. at all positions.

Table 14: Zodiacal light brightness (Leinert et al. 1997) in units of 10^{-8} W m^{-2} sr^{-1} μm^{-1} for a wavelength of 0.50 μm.

β \ λ-λ₀	0°	5°	10°	15°	20°	25°	30°	45°	60°	75°	90°
0°				3140	1610	985	640	275	150	100	77
5°				2940	1540	945	625	271	150	100	77
10°			4740	2470	1370	865	590	264	148	100	77
15°	11500	67800	3440	1860	1110	755	525	251	146	100	77
20°	6400	4480	2410	1410	910	635	454	237	141	99	77
25°	3840	2830	1730	1100	749	545	410	223	136	97	77
30°	2480	1870	1220	845	615	467	365	207	131	95	77
35°	1650	1270	910	680	510	397	320	193	125	93	77
40°	1180	940	700	530	416	338	282	179	120	92	77
45°	910	730	555	442	356	292	250	166	116	90	77
60°	505	442	352	292	243	209	183	134	104	86	77
75°	338	317	269	227	196	172	151	116	93	82	77
90°	259	251	225	193	166	147	132	104	86	79	77
105°	212	210	197	170	150	133	119	96	82	77	77
120°	188	186	177	154	138	125	113	90	77	74	77
135°	179	178	166	147	134	122	110	90	77	73	77
150°	179	178	165	148	137	127	116	96	79	72	77
165°	196	192	179	165	151	141	131	104	82	72	77
180°	230	212	195	178	163	148	134	105	83	72	77

Table 15: Elongation of observation points in Table 14.

β \ λ-λ₀	0°	5°	10°	15°	20°	25°	30°	45°	60°	75°	90°
0°	x	5.00	10.00	15.00	20.00	25.00	30.00	45.00	60.00	75.00	90.00
5°	5.00	7.07	11.17	15.79	20.59	25.46	30.38	45.22	60.13	75.06	90.00
10°	10.00	11.17	14.11	17.96	22.27	26.81	31.48	45.86	60.50	75.23	90.00
15°	15.00	15.79	17.96	21.09	24.81	28.90	33.23	46.92	61.12	75.52	90.00
20°	20.00	20.59	22.27	24.81	27.99	31.61	35.53	48.36	61.98	75.92	90.00
25°	25.00	25.46	26.81	28.91	31.61	34.78	38.29	50.14	63.05	76.43	90.00
30°	30.00	30.38	31.47	33.23	35.53	38.29	41.41	52.24	64.34	77.05	90.00
35°	35.00	35.31	36.22	37.70	39.67	42.06	44.81	54.60	65.82	77.76	90.00
40°	40.00	40.26	41.03	42.27	43.96	46.03	48.44	57.20	67.48	78.56	90.00
45°	45.00	45.22	45.86	46.92	48.36	50.14	52.24	60.00	69.30	79.46	90.00
60°	60.00	60.13	60.50	61.12	61.98	63.05	64.34	69.30	75.52	82.56	90.00
75°	75.00	75.06	75.23	75.52	75.92	76.43	77.05	79.46	82.56	86.16	90.00
90°	90.00	90.00	90.00	90.00	90.00	90.00	90.00	90.00	90.00	90.00	90.00
105°	105.00	104.94	104.77	104.48	104.08	103.57	102.95	100.54	97.44	93.84	90.00
120°	120.00	119.87	119.50	118.88	118.02	116.95	115.66	110.70	104.48	97.44	90.00
135°	135.00	134.78	134.14	133.08	131.64	129.86	127.76	120.00	110.70	100.54	90.00
150°	150.00	149.62	148.52	146.77	144.47	141.71	138.59	127.76	115.66	102.95	90.00
165°	165.00	164.21	162.04	158.91	155.19	151.10	146.77	133.08	118.88	104.48	90.00
180°	180.00	175.00	170.00	165.00	160.00	155.00	150.00	135.00	120.00	105.00	90.00

Table 16: Zodiacal light brightness from CBZODY6 in units of 10^{-8} W m^{-2} sr^{-1} μm^{-1} for a wavelength of 0.50 μm for 21 March.

λ-λ₀ \ β	0°	5°	10°	15°	20°	25°	30°	45°	60°	75°	90°
0°	x	131810	15425	4497	1970	1095	706	307	190	138	120
5°	1020800	100230	15087	4521	1984	1100	708	306	189	138	120
10°	128890	46941	12262	4276	1957	1095	706	305	189	138	120
15°	38795	22341	8702	3691	1837	1063	694	302	188	137	120
20°	16710	11859	5976	2998	1644	1000	668	297	186	137	120
25°	8776	6948	4146	2375	1423	915	631	291	184	136	120
30°	5231	4415	2956	1873	1211	821	586	282	181	135	120
35°	3407	2997	2173	1487	1024	728	538	272	178	134	120
40°	2370	2142	1648	1194	866	642	490	262	174	133	120
45°	1735	1601	1285	975	737	566	444	250	170	132	120
60°	852	820	711	586	480	397	332	214	156	128	120
75°	534	530	482	416	354	303	263	185	145	126	120
90°	407	411	387	348	305	268	236	174	141	125	120
105°	371	379	365	336	302	269	241	178	143	125	120
120°	406	415	404	378	343	307	274	197	151	127	120
135°	536	548	532	497	448	396	346	230	163	130	120
150°	863	873	833	758	663	564	473	276	177	132	120
165°	1596	1580	1443	1238	1015	809	638	321	188	134	120
180°	2313	2246	1966	1602	1251	956	727	341	192	135	120

Table 17: Zodiacal light brightness from CBZODY6 in units of 10^{-8} W m^{-2} sr^{-1} μm^{-1} for a wavelength of 0.50 μm for 21 June.

λ-λ₀ \ β	0°	5°	10°	15°	20°	25°	30°	45°	60°	75°	90°
0°	x	134690	15091	4182	1747	937	591	251	154	110	94
5°	955290	107410	15511	4391	1823	969	606	253	155	110	94
10°	120560	50001	12764	4246	1846	988	616	254	155	110	94
15°	36273	23455	9069	3695	1758	976	615	254	155	110	94
20°	15615	12258	6204	3011	1585	928	600	252	154	109	94
25°	8194	7084	4279	2383	1377	854	572	248	152	109	94
30°	4880	4455	3029	1873	1172	769	534	242	151	108	94
35°	3175	2993	2210	1481	990	683	492	235	148	107	94
40°	2207	2122	1662	1183	835	602	448	226	145	107	94
45°	1615	1574	1286	960	708	530	406	217	142	106	94
60°	795	791	694	565	454	367	302	185	129	103	94
75°	503	503	457	390	326	274	233	157	119	101	94
90°	388	387	360	317	274	236	206	146	115	100	94
105°	357	355	334	301	266	233	206	148	116	100	94
120°	393	389	367	334	297	262	231	162	122	101	94
135°	523	513	481	435	384	334	288	187	131	103	94
150°	843	819	753	663	566	472	390	222	141	105	94
165°	1558	1486	1309	1086	866	676	524	257	149	106	94
180°	2255	2112	1784	1405	1065	795	594	271	151	106	94

Table 18: Zodiacal light brightness from CBZODY6 in units of 10^{-8} W m^{-2} sr^{-1} μm^{-1} for a wavelength of 0.50 μm for 21 September.

λ-λ₀ \ β	0°	5°	10°	15°	20°	25°	30°	45°	60°	75°	90°
0°	x	150480	16384	4357	1743	903	556	229	141	102	87
5°	997370	104520	15393	4294	1739	902	555	228	141	102	87
10°	125910	46630	12017	3971	1701	897	554	227	140	101	87
15°	37898	21734	8303	3363	1584	871	546	225	139	101	87
20°	16323	11417	5597	2691	1406	818	528	222	138	100	87
25°	8572	6643	3834	2106	1209	747	499	218	136	100	87
30°	5110	4198	2705	1644	1022	669	464	213	135	99	87
35°	3328	2833	1972	1293	859	591	426	206	132	98	87
40°	2315	2013	1483	1031	723	520	388	198	130	97	87
45°	1695	1494	1146	835	611	457	351	190	127	96	87
60°	832	748	616	489	390	316	261	163	116	93	87
75°	522	472	402	333	277	234	200	138	106	91	87
90°	397	362	316	270	231	199	174	126	102	90	87
105°	362	333	296	259	225	197	174	128	102	90	87
120°	396	367	330	292	256	224	197	140	107	91	87
135°	524	487	440	388	337	291	250	163	116	93	87
150°	842	785	701	604	508	420	345	196	125	94	87
165°	1557	1442	1240	1010	794	613	472	230	133	96	87
180°	2257	2066	1712	1327	992	733	543	245	137	96	87

Table 19: Zodiacal light brightness from CBZODY6 in units of 10^{-8} W m^{-2} sr^{-1} μm^{-1} for a wavelength of 0.50 μm for 21 December.

λ-λ₀ \ β	0°	5°	10°	15°	20°	25°	30°	45°	60°	75°	90°
0°	x	145780	16473	4612	1949	1054	668	285	176	131	112
5°	1053500	96329	14703	4348	1874	1024	654	282	175	130	112
10°	132940	43419	11377	3945	1789	994	639	278	174	130	112
15°	39997	20538	7887	3326	1646	949	620	273	172	129	112
20°	17220	10944	5355	2665	1456	884	592	267	170	128	112
25°	9038	6448	3700	2095	1251	804	556	260	168	128	112
30°	5384	4116	2636	1646	1060	719	515	252	165	127	112
35°	3504	2804	1940	1305	895	636	472	243	162	125	112
40°	2437	2011	1473	1049	757	561	429	233	158	124	112
45°	1784	1504	1150	856	644	494	389	223	155	123	112
60°	879	771	637	515	420	348	293	192	143	119	112
75°	557	501	430	363	308	265	231	166	132	116	112
90°	429	396	350	304	264	231	205	154	127	115	112
105°	396	372	338	300	265	234	209	157	129	115	112
120°	436	416	383	345	307	272	241	174	136	117	112
135°	579	559	518	466	411	358	311	206	147	119	112
150°	932	903	829	731	625	523	434	250	161	122	112
165°	1721	1652	1464	1222	979	767	597	296	173	124	112
180°	2490	2361	2017	1605	1227	922	692	318	178	126	112

3.7 Photometric Observations

An amateur astronomer obtained observations of the zodiacal cloud on the night of 6 March 2000 (Schmude 1999). He obtained 6 observations for each of the 7 points listed in Table 20.

Table 20: Schmude (1999) pointings for zodiacal light observations.

Point No.	R.A.	Dec
1	$2^h\,05^m$	+33.5
2	$1^h\,53^m$	+27.8
3	$2^h\,15^m$	+23.5
4	$2^h\,21^m$	+19.2
5	$2^h\,32^m$	+13.1
6	$2^h\,52^m$	+9.5
7	$2^h\,54^m$	+3.6

Schmude visually estimated that Point #4 was the brightest and that points # 1, 2, 6, and 7 were outside of the cloud. He averaged points 1, 2, 6, and 7 to obtain a sky background and used point #4 as sky + zodiacal. Table 21 is a summary of his observations.

Table 21: Schmude B, V, and B-V observations for 6 March 2000.

	Johnson B	Johnson V
Brightness (mag/sq. arc-sec)	22.37 ± 0.27	21.89 ± 0.42
B-V	0.48 ± 0.50	

To reproduce his observations with CBZODY6, we took the 7 pointings of Table 20 and ran the model for 0^h UT on 6 March 2000. Our results are shown in Table 22.

Table 22: CBZODY6 runs for the 7 points of Table 18.

R.A.	Dec	Ecl Long	Ecl Lat	Elong	Johnson B $\mathrm{W/cm^2/\mu m}$	Johnson V $\mathrm{W/cm^2/\mu m}$
33.500	31.250	40.850	19.532	57.387	1.0882E-13	1.1291E-13
27.800	28.250	36.169	15.151	52.065	1.5404E-13	1.5982E-13
23.500	33.750	39.388	9.393	54.220	1.7812E-13	1.8480E-13
19.200	35.250	39.284	4.873	53.706	2.0920E-13	2.1705E-13
13.100	38.000	39.838	-1.751	54.126	2.1547E-13	2.2355E-13
9.500	43.000	43.428	-6.668	57.942	1.6177E-13	1.6784E-13
3.600	43.500	42.150	-12.453	57.310	1.3136E-13	1.3629E-13

Table 23 shows the photometric parameters for the Johnson B and V bands used to convert the flux units to magnitudes. Using a pixel size of 0.8209 deg/pixel = 2955.25 arc-sec/pixel gives an area, in magnitude units, of 2.5 log (2955.25^2) = 17.353. Adding the area to the brightness in magnitudes gives a surface brightness in magnitudes per square arc-second.

Table 23: Johnson B & V photometric parameters.

	Johnson B	Johnson V
Center	0.44	0.55
Bandwidth	.098	.089
Flux at 0 mag (W/cm^2/μm)	6.61e-12	3.72e-12

Table 24 gives the results of averaging points 1, 2, 6, and 7 which is our representation of the sky background. Our contention is that each of Schmude's 7 observations contains a uniform sky background plus a varying zodiacal component. We can safely ignore true sky radiance since it is ultimately subtracted from the answer.

Table 25 further shows the contribution from point 4 [zodiacal] and the zodiacal-sky computation. Finally, the flux is converted to magnitudes and magnitudes/square arc-second.

Table 24: Point 4 brightness as computed by CBZODY6.

	Johnson B	Johnson V
Sky (Average of 1,2,6,7) (W/cm^2/μm)	1.390E-13	1.442E-13
Zodiacal (Point 4) (W/cm^2/μm)	2.092E-13	2.171E-13
Zodiacal - Sky (W/cm^2/μm)	7.020E-14	7.284E-14
Brightness (mag)	4.93	4.27
B-V	0.66	
Brightness (mag/sq. arc-sec)	22.29	21.62

We find B, V, and B-V are all within the quoted observational errors. CBZODY6 B is 0.08 magnitudes per square arc-second brighter than the observation. The V band is 0.27 magnitudes per square arc-second brighter. His error in B-V gives a range of values which includes Allen's reference value of +0.66 accepted range of B-V for the Sun 0.66.

Schmude's Point #5 actually has the highest zodiacal brightness, being closest to the ecliptic plane. The brightness for that point is given in Table 25. Note that since his sky measurements were not subtracted, the zodiacal light is over 1 magnitude brighter than his quotes.

Table 25: Zodiacal brightness for Point 5.

	Johnson B	Johnson V
Zodiacal (Point 5) (W/cm^2/μm)	2.1547E-13	2.2355E-13
Brightness (mag)	3.72	3.05
B-V	0.66	
Brightness (mag/sq. arc-sec)	21.07	20.41

Absolute ground based measurements of the zodiacal light are difficult to obtain. However, the zodiacal light is a measurable, not to mention visible to the naked eye, phenomenon which sensor systems must be aware of for proper operation.

3.8 Visible Imaging

On the evening of 5 April 1997 Marco Fulle climbed to the 750m mark on the volcanic island of Mt. Stromboli off the coast Sicily. He took the 3 minute photograph shown in Figure 52 (which also appeared in the January 2001 issue of Sky & Telescope). The image has several components:

- The image is looking west towards the horizon with the last few minutes of twilight visible as the bright yellow band.

- Below the twilight is the hard Earth

- Just above the twilight, bottom left of center, is the planet Mercury

- The stars are visible with the Pleiades prominent near the top left of center

- Comet Hale-Bopp is very noticeable to the right of center

- The zodiacal light is visible above the twilight

Figure 53 shows our effort to recreate this image using the components of CBSD and the Air Force Research Laboratory's atmospheric transmission model MODTRAN. The creation of the image took several steps. Since this is a horizon image, atmospheric attenuation is an important factor. Also, the sky radiance from twilight needs to be included.

1. The image was taken using Kodak Elitechrome 400 film. Using the Kodak data sheets, filter functions where derived for Yellow, Magenta, and Cyan forming layers. Since this is a reversal film, these correspond to Blue, Green, and Red with responses similar to the human eye.

2. Refraction was also found to be important and a simple refraction function was included in the CBSD codes (Meeus 1996, p56).

3. Using MODTRAN, we created a database of radiance and transmittance as a function of altitude for the date, time, and look angles associated with the image in each of the three bands.

4. The models CBAMP4 and CBSKY4 were run with the atmospheric attenuation found from MODTRAN.

5. A point spread function, simple circular with gaussian fall off, was used on the CBAMP4 and CBSKY4 images.

6. It was found that the atmospheric radiance as produced by MODTRAN extended 1.2° above the horizon (the Sun was 15.7° below the horizon for this image). This is contrary to the observation that shows Mercury, at an apparent altitude of 3.1°, still within the twilight. To compensate, the radiance database was extended by a simple extrapolation.

7. The model CBZODY6 was run with atmospheric attenuation and included the MODTRAN sky radiance (only one model needed the sky radiance). CBZODY6 was structurally closest to the requirements of a sky radiance model.

8. Finally, the images needed the application of the film's characteristic curve for the correct color balance. This proved to be difficult due to the lack of information on the low light level characteristics of this film. The published characteristic curve was used. However, the log intensity of the illumination for the characteristic curve ranges from −3.5 to 0 lux-seconds. The model predicated a range of −6 to −2 lux-seconds (wavelength dependence was included in the $W\text{-}cm^2$ to lux conversion). The solution was to use an empirical approximation of the characteristic curve (Lehmann and Häupl, 1986). We then included a linear extension for low illumination levels.

Figure 52: Image of the zodiacal light taken from Mt. Stromboli by Marco Fulle. On the evening of 5 April 1997, Marco Fulle took an image of the zodiacal light seen stretching from the horizon to the Pleiades. (© Marco Fulle, 1997, used with permission.)
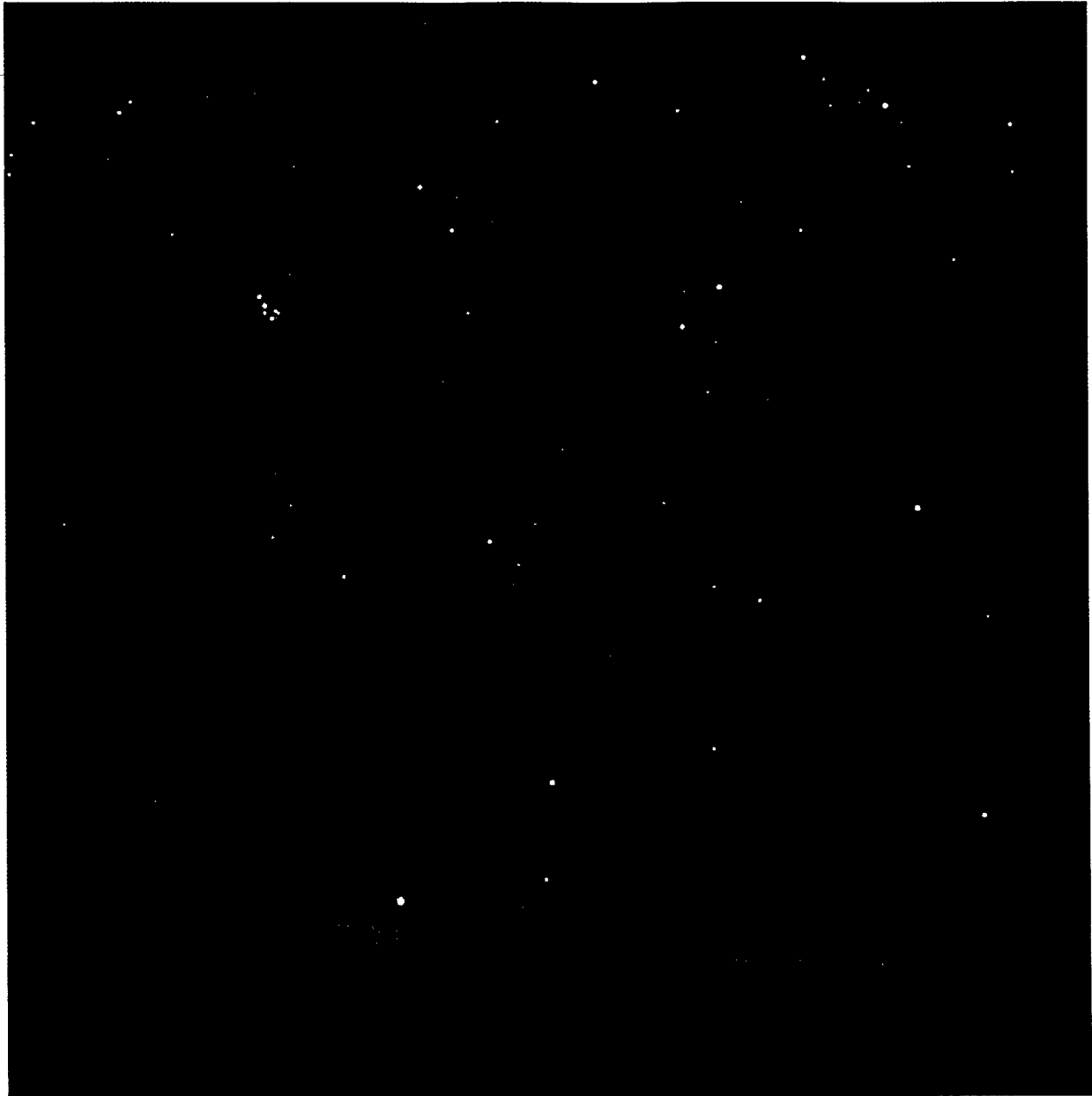
Figure 53: A CBSD and MODTRAN view of the same region as Figure 52.

We have come up with a final image that resembles, but is not identical to the observations:

- The contrast and color balance of the simulated image are very close to but do not exactly match the original. This is attributable to uncertainties in the shape of the characteristic curve.

- The sky radiance was used as a linear function with altitude above the horizon. No azimuthal dependencies were included and this clearly is a limitation.

- The overall shape of the zodiacal light shows more of an egg shape rather than a bubble. We attribute this to two possible causes; 1) the atmospheric attenuation is not as great as MODTRAN predicts; 2) the sky radiance extends even higher filling in the zodiacal structure. Figure 54 shows the shape of the zodiacal light without (a) and with (b) atmospheric attenuation. The unattenuated image shows a shape much closer to the observed image.

- Comets are not included in the CBSD simulation.

Figure 54: Single band atmospheric attenuation. a) CBZODY6 including refraction and twilight sky radiance from MODTRAN b) CBZODY6 refraction, twilight sky radiance, and attenuation (twilight sky radiance and attenuation from MODTRAN). Indications are that the atmospheric attenuation observed is much less than that predicted by MODTRAN.

3.9 COBE CIO Daily All Sky Coverage

The COBE/DIRBE CIO (Calibrated Individual Observations) are the complete set of observations obtained during the COBE mission. They have not been weekly averaged, as the skymap data have.

For our analysis, we took 38 CIO days distributed throughout the mission. For each day we ran a non-linear least squares routine for a set of 8 parameters; ascending node, inclination, HWHM, and normalization density for the two planes. We excluded the region of the image that contained the galactic plane. Figure 55 shows the percentage error for two typical days a) and b). In Figures 55 c) and d) the exclusion zone are overlaid. Since the galaxy is not regular, some regions of the plane do appear outside of the zone. We found this had very little effect on the fit results, however, it did occasionally affect the quoted standard deviation.
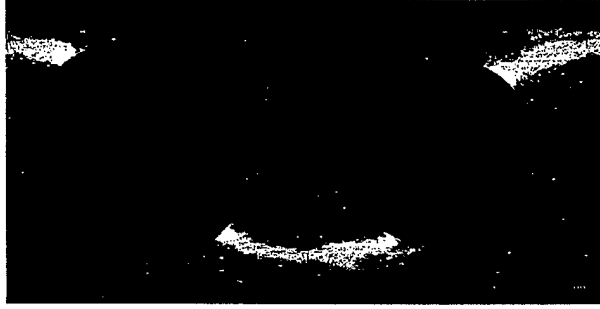
a) CIO 89365 percentage error

b) CIO 90263 percentage error
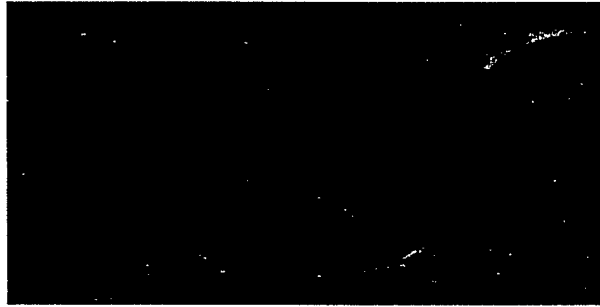
c) CIO 89365 percentage error with galactic exclusion zone shown

d) CIO 90263 percentage error with galactic exclusion zone shown

Figure 55: Location of the galactic exclusion zone. Note that the zone does not always exclude all galactic components. For all, white > 5% and black < -5%.

Table 26 shows the results of individually fitting 38 CIO datasets. This represents the best fit to that dataset for only Band 5. l is the mean solar longitude during the observation. The Mean Deviation (α) is defined as:

$$\alpha = 100 \times \frac{1}{N} \sum_i \left| \frac{d_i - x_i}{d_i} \right| \%$$

where d_i is the observed data value and x_i is the modeled data value. The subscripts 1 and 2 refer to the inner and outer plane respectively.

Table 27 shows the mean and standard deviations for 67 CIO datasets using the generalized parameter of the Table 12 set obtained from the fit in 3 COBE/DIRBE bands (4,5 and 6)

Table 28 is the mean of all observations. It represents our final error between CBZODY6 and the CIO data. Figure 56 shows the mean error plotted against the heliocentric ecliptic longitude of the Earth.

Figures 57, 58, and 59 show typical fits in COBE/DIRBE bands 4, 5, and 6 respectively. Each figure has 4 panes a) the original CIO data, b) the CBZODY6 fit, c) the residual, and d) the percentage error.

61

Table 26: Mean deviations for all NLS parameter fit CIO datasets for Band 5.

CIO	l (°)	α (%)	σ	Ω_1	Ω_2	i_1	i_2	Γ_1	Γ_2	N_1	N_2
89345	79.6	1.70	0.60	86.89	79.19	2.467	2.392	0.378	0.288	1.208	1.550
89346	80.2	1.69	0.77	85.85	79.05	2.600	2.332	0.379	0.288	1.205	1.553
89347	81.5	1.69	0.75	86.44	79.35	2.488	2.377	0.376	0.288	1.208	1.547
89348	82.4	1.68	1.15	85.83	79.03	2.489	2.376	0.376	0.287	1.208	1.547
89349	83.8	1.69	0.61	85.96	78.87	2.498	2.370	0.376	0.287	1.210	1.546
89350	84.3	1.71	1.10	85.37	78.89	2.553	2.377	0.381	0.284	1.201	1.557
89365	99.9	1.67	0.27	82.82	78.92	2.496	2.457	0.377	0.286	1.205	1.531
90005	104.5	1.72	11.43	84.17	76.01	2.772	2.344	0.385	0.280	1.192	1.551
90010	110.0	1.70	0.29	81.69	78.62	2.621	2.475	0.379	0.285	1.200	1.526
90020	120.0	1.71	16.32	77.43	77.40	2.317	2.380	0.372	0.282	1.215	1.524
90041	141.0	1.69	0.72	76.80	79.65	2.677	2.425	0.368	0.283	1.219	1.506
90050	151.2	9.17	0.64	83.59	75.95	2.946	2.444	0.375	0.283	1.198	1.504
90060	160.2	1.46	1.61	85.46	72.26	2.900	2.387	0.371	0.282	1.208	1.511
90071	171.2	1.33	5.01	90.98	71.04	2.989	2.417	0.369	0.281	1.222	1.515
90080	181.1	1.27	1.24	81.42	75.43	3.000	2.371	0.366	0.278	1.227	1.520
90100	200.1	1.28	8.12	93.48	85.05	2.706	2.269	0.388	0.275	1.188	1.533
90114	214.7	1.29	2.77	83.50	83.79	2.785	2.300	0.373	0.281	1.202	1.504
90115	215.7	1.30	1.56	82.89	83.47	2.792	2.311	0.372	0.281	1.204	1.502
90116	216.0	1.30	2.02	82.94	82.61	2.792	2.299	0.371	0.281	1.206	1.504
90118	217.1	1.53	27.72	78.80	82.90	2.667	2.234	0.351	0.276	1.250	1.506
90134	232.5	1.59	15.39	80.89	80.17	3.000	2.331	0.361	0.277	1.227	1.527
90135	233.8	1.62	19.84	80.92	79.58	3.000	2.286	0.362	0.272	1.226	1.548
90140	239.8	1.49	10.69	80.68	79.88	3.000	2.300	0.361	0.280	1.229	1.532
90145	244.2	1.63	25.10	80.52	79.35	3.000	2.328	0.350	0.277	1.249	1.534
90150	248.2	1.60	23.53	80.44	78.16	3.000	2.251	0.356	0.277	1.236	1.542
90166	264.0	1.54	14.20	81.81	78.89	3.000	2.392	0.366	0.279	1.208	1.550
90168	265.1	1.64	84.35	84.48	78.58	3.000	2.030	0.351	0.280	1.235	1.542
90175	272.1	1.53	10.36	82.62	77.93	3.000	2.523	0.366	0.286	1.209	1.541
90187	284.6	1.73	46.08	81.94	78.10	3.000	2.484	0.367	0.276	1.199	1.562
90199	295.6	1.61	13.92	80.99	77.47	2.978	2.633	0.367	0.284	1.202	1.556
90205	302.5	1.68	40.76	80.95	77.16	2.949	2.568	0.370	0.277	1.203	1.581
90212	307.8	1.77	18.87	78.89	76.04	2.888	2.570	0.377	0.276	1.193	1.599
90220	315.1	1.58	30.56	70.28	77.49	2.641	2.533	0.376	0.280	1.197	1.593
90235	330.2	1.60	70.42	78.78	75.25	3.000	2.439	0.379	0.277	1.204	1.624
90241	336.0	1.58	66.73	80.67	75.21	3.000	2.438	0.382	0.277	1.195	1.635
90245	338.2	1.47	29.42	83.29	76.38	3.000	2.489	0.375	0.281	1.201	1.620
90251	346.0	1.49	48.77	88.21	74.82	3.000	2.453	0.375	0.280	1.199	1.623
90263	356.9	1.62	147.59	95.66	75.80	3.000	2.409	0.384	0.271	1.188	1.662

Table 27: Mean deviations and standard deviations for all modeled CIO datasets in 3 bands using generalized parameter set.

Day	Solar Longitude	Band 4 α	Band 4 σ	Band 5 α	Band 5 σ	Band 6 α	Band 6 σ
89345	79.65	8.27	0.15	11.76	9.84	3.26	3.68
89346	80.18	8.21	0.16	11.67	9.39	3.2	3.44
89347	81.42	7.89	0.14	11.98	10.44	3.23	3.75
89348	82.46	7.91	0.14	12.01	10.83	3.2	3.59
89349	83.76	7.92	0.13	12.01	10.3	3.18	3.48
89350	84.28	8.07	0.19	12.17	10.8	3.15	3.86
89351	85.46	8.04	0.79	12.05	39.18	3.13	51.53
89360	95.00	8.56	0.11	12.67	10.75	3.08	3.27
89365	99.94	8.41	0.16	12.88	10.91	3.06	3.11
90005	104.51	8.2	0.24	13.27	22.44	3.08	35.71
90010	110.05	7.96	0.17	13.29	11.32	4.09	3.09
90015	115.47	8.3	0.39	13.34	13.71	3.15	6.73
90017	116.62	8.26	0.15	13.36	11.74	3.18	3.83
90020	120.05	8.63	0.24	13.53	27.24	3.19	53.66
90023	123.64	8.58	0.12	13.69	13.75	3.27	3.22
90025	124.71	8.57	0.13	13.86	14.87	3.36	3.46
90031	131.76	8.5	0.18	13.9	16.07	3.45	12.04
90035	135.82	8.89	0.57	13.94	42.06	3.64	63.25
90041	141.09	8.53	0.16	14.23	12	3.84	25.03
90045	144.92	8.97	0.44	14.68	19.95	3.98	44.1
90047	147.52	8.8	0.27	14.66	17.05	4	29.17
90050	151.27	9.41	0.19	24.02	11.75	38.89	16.48
90055	155.39	8.74	0.13	14.83	11.01	4.05	14.62
90060	160.16	8.79	0.27	14.49	11.18	3.94	31.09
90065	165.78	9.35	1.61	14.14	43.33	3.88	76.97
90071	171.15	8.5	0.16	14	13.6	3.8	20.41
90073	173.91	8.51	0.19	14.04	9.81	3.76	22.18
90075	175.93	9.08	0.47	13.93	46.6	3.79	105.32
90078	178.33	8.82	0.15	14.02	9.46	3.81	12.11
90080	181.21	9.16	0.54	14.08	9.53	3.8	33.8
90085	184.75	8.95	0.18	13.99	11.82	3.82	47.2
90090	191.41	8.78	0.18	13.94	8.84	3.81	26.09
90095	194.57	9.05	0.47	14.1	85.42	3.87	177.54
90100	200.06	9.32	1.51	14.36	17.17	3.91	44.8
90105	205.9	9.14	0.61	14.8	13.01	4.01	6.16
90114	214.82	9.69	0.4	14.66	14.62	3.9	7.5
90115	215.72	9.47	0.29	14.51	13.5	3.87	6.63
90116	216	9.34	0.38	14.51	13.98	3.88	6.34
90118	217.06	9.35	0.53	14.35	39.65	3.85	95.62
90127	225.83	8.88	0.41	13.88	27.22	3.73	74.9
90134	232.47	9.04	0.34	13.34	26.62	3.68	65.15
90135	233.73	9.56	0.34	12.69	29.22	3.63	71.66
90140	239.83	9.03	0.65	12.59	20.51	3.41	42.98
90145	244.23	9.1	0.27	12.64	34.95	3.41	114.64
90150	248.18	8.73	0.3	12.58	33.61	3.61	63.48

Table 27: (cont.)

Day	Solar Longitude	Band 4		Band 5		Band 6	
		α	σ	α	σ	α	σ
90155	254.48	8.65	0.65	12.71	28.28	3.19	63.66
90164	263.23	9.34	1.76	12.6	54.19	3.03	138.34
90165	263.78	9.19	0.24	12.47	19.32	2.96	33.83
90166	264.03	8.81	0.15	12.34	24.12	2.93	62.07
90168	265.1	8.82	0.52	12.35	94.79	2.95	80.61
90175	272.15	8.69	0.23	11.66	19.81	2.99	28.8
90180	278.35	8.8	0.16	11.83	34.43	3.01	112.96
90185	281.46	8.88	0.2	12.18	45.72	3.4	168.9
90187	284.71	8.93	0.23	12.23	56.41	3.41	208.35
90195	290.56	9.03	0.22	11.61	35.38	3.26	109.43
90199	295.45	8.93	0.15	11.24	23.12	3.21	58.2
90205	302.53	9.11	0.22	10.96	49.88	3.25	172.62
90212	307.56	9.98	0.32	10.48	27.14	3.35	72.83
90215	310.67	10.01	0.19	10.1	17.71	3.25	49.19
90220	315.22	10.13	0.21	9.94	37.99	3.36	127.97
90225	320.08	10.62	0.69	9.53	59.41	3.45	195.73
90235	330.41	10.07	0.34	9.37	76.77	3.42	321.63
90241	335.99	10.12	0.21	9.18	72.57	3.33	321.06
90245	338.14	9.85	0.22	9.14	34.66	3.27	147.07
90251	346.16	9.92	0.2	9.31	54.32	3.12	218.66
90255	350.78	9.77	0.28	9.16	79.38	3.06	334.3
90263	356.78	9.59	0.31	9.06	154.9	3.08	309.6

Table 28: Average of all mean deviations (the mean deviation of all modeled observations).

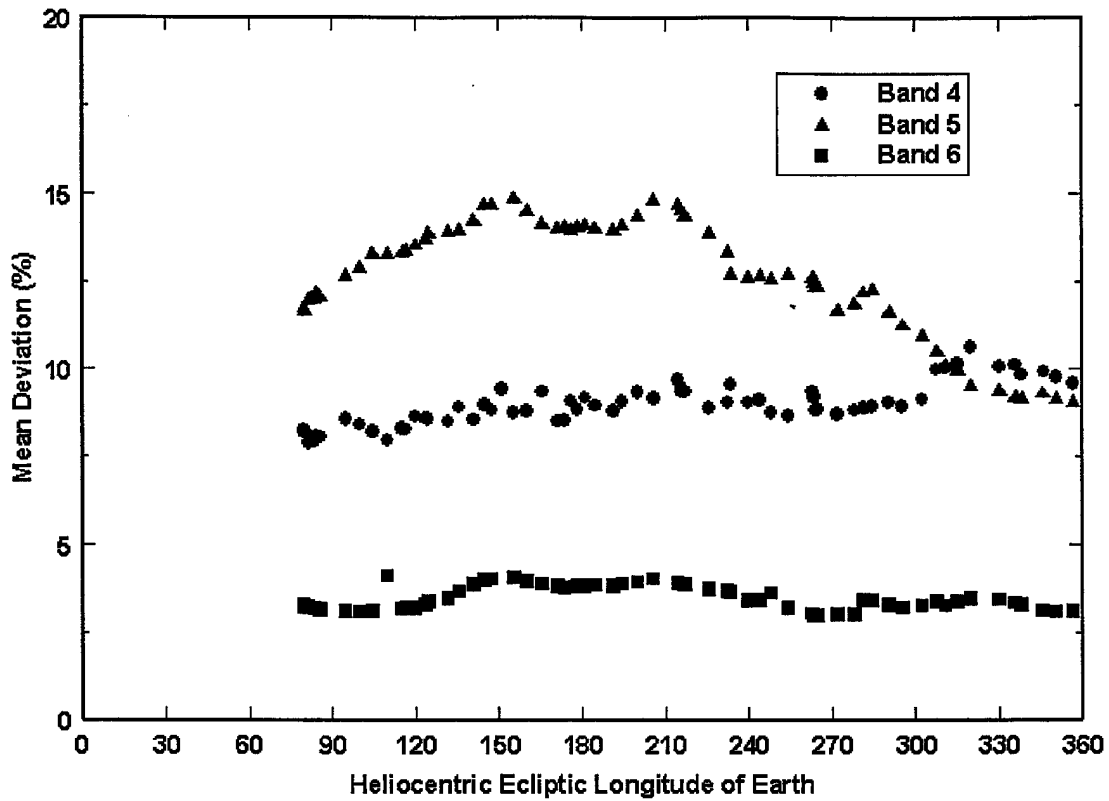| Band 4	Band 5	Band 6
9.0%	12.8%	4.0%

Figure 56: Mean deviation errors versus Heliocentric ecliptic longitude of Earth. The three COBE/DIRBE bands are plotted with the mean error for one CIO day versus heliocentric ecliptic longitude of Earth. Band 5 shows the highest deviation as expected from the fit to the ISO spectrum of Figure 48.
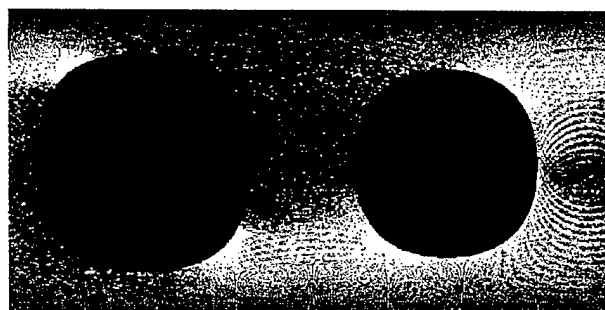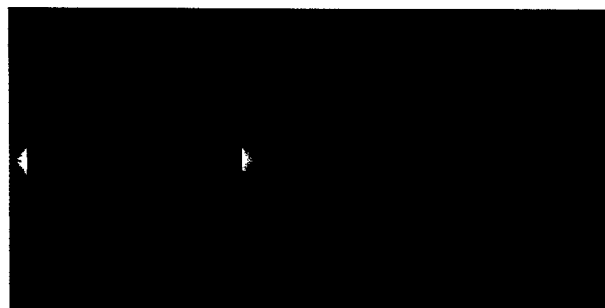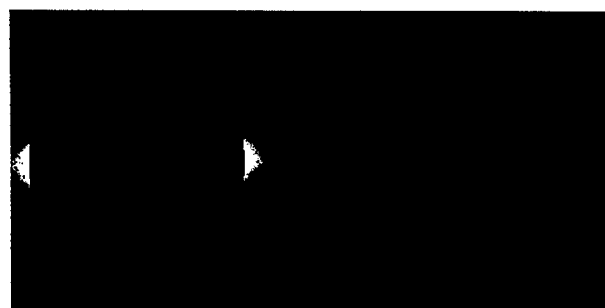
a) Data

b) Model
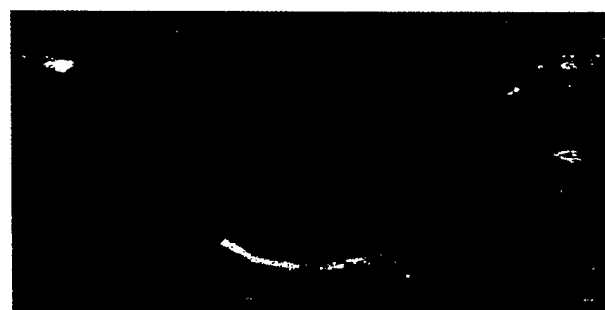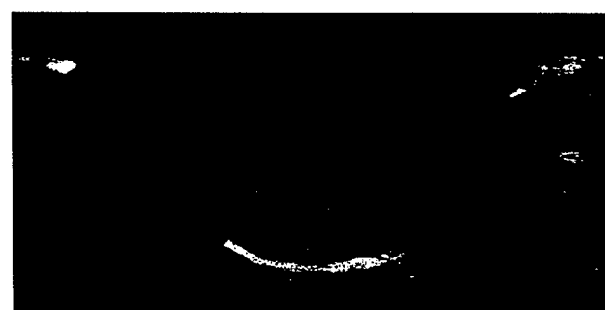
c) Residual

d) Percentage Error

Figure 57: Day 90005 Band 4. For Residual plots, white >5 MJy/sr and black < -5 MJy/sr. For Percentage Error plot, white >5% and black < -5%.

a) Data

b) Model

c) Residual

d) Percentage Error

Figure 58: Day 90005 Band 5 For Residual plots, white >5 MJy/sr and black < -5 MJy/sr. For Percentage Error plot, white >5% and black < -5%.

66

a) Data

b) Model

c) Residual

d) Percentage Error
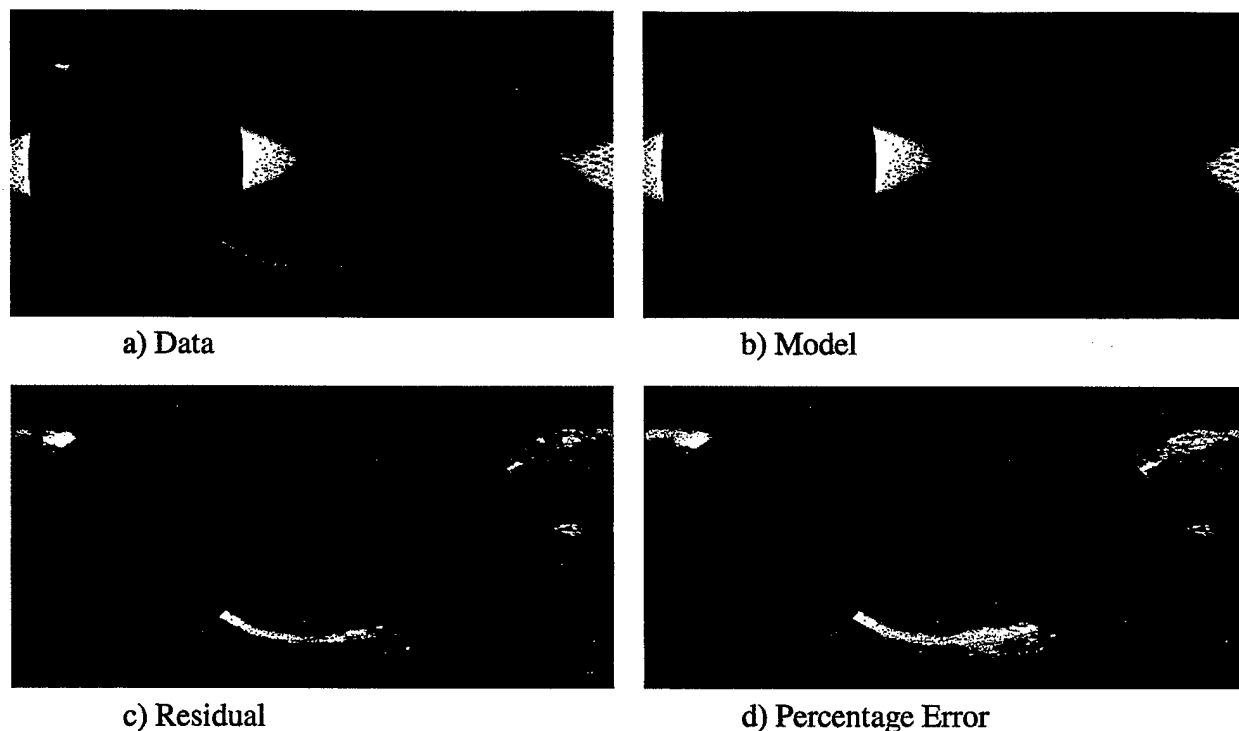
Figure 59: Day 90005 Band 6. For Residual plots, white >5 MJy/sr and black < -5 MJy/sr. For Percentage Error plot, white >5% and black < -5%.

3.10 South Ecliptic Pole (SEP)

During the COBE mission one of the early release products was observations of the South Ecliptic Pole (SEP). The initial data were 10 values representing the brightness seen in the 10 DIRBE bands. However, single values are insufficient to represent the zodiacal brightness, as the zodiacal light is a time-varying phenomenon. The poles of the ecliptic plane and the zodiacal cloud symmetry do not line up, which results in a slight sinusoidal variation of the brightness of the ecliptic pole. Figure 60 shows the COBE data (Band 1 through 6) for observations of the SEP using the weekly skymap data. We have plotted the brightness data versus the heliocentric ecliptic longitude of the Earth. Bands 1, 2, and 3 show little sinusoidal variations. However, bands 4, 5, and 6 show a strong sinusoidal component. We also noted that the brightness at the SEP in bands 1 through 4 is higher than CBZODY6 predictions. In conjunction with Martin Cohen (1999), we obtained his SKY5 estimates of the SEP brightness due to unresolved stellar point sources.
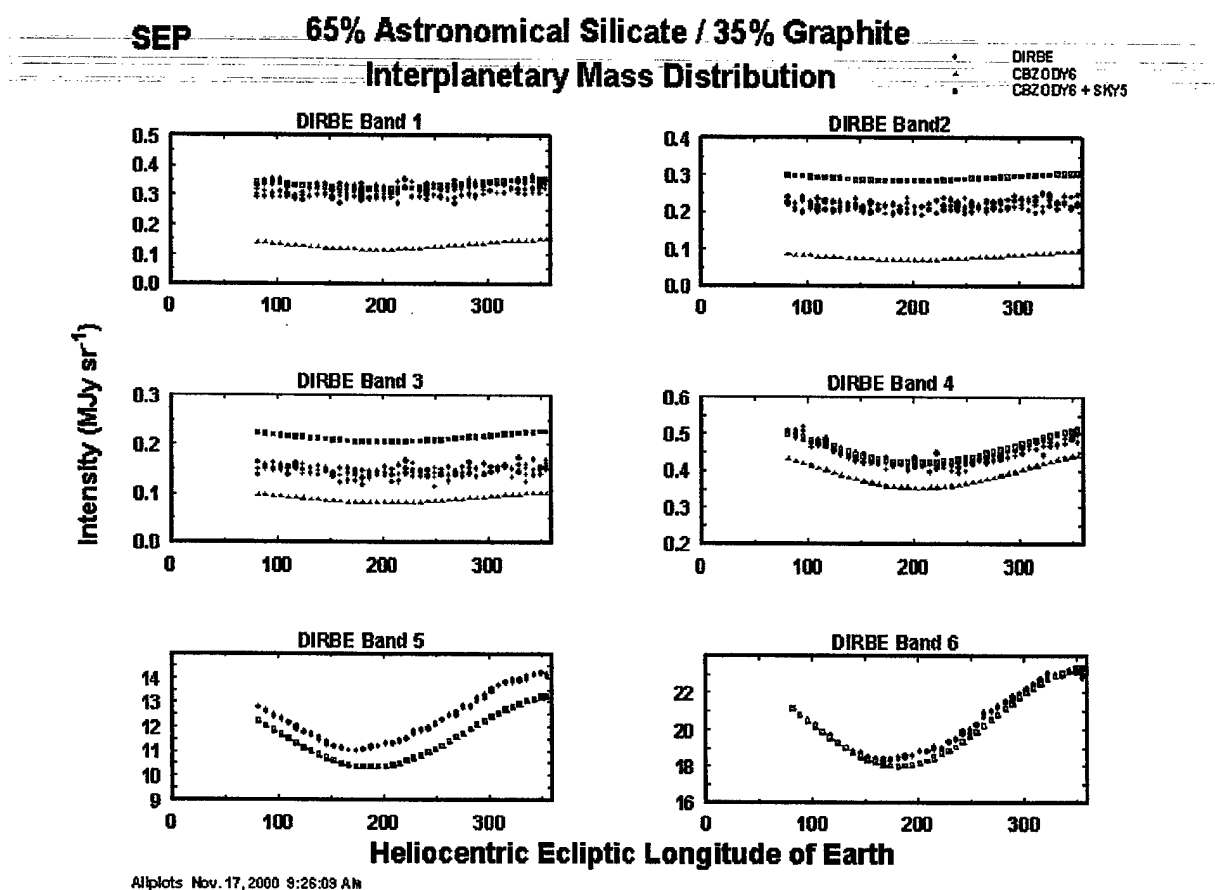
67

SEP   **65% Astronomical Silicate / 35% Graphite**
Interplanetary Mass Distribution

Figure 60: Final SEP fit. The six COBE/DIRBE bands compared to a CBZODY6 + SKY4 fit.

3.11 COBE CIO In-Plane Data

The in-plane data represent the zodiacal intensity in the ecliptic plane. The data of Figure 61 have been extracted from the COBE CIO data. Three of the COBE bands are shown, Band 4 (4.4μm), Band 5 (12μm) and Band 6 (25μm).

COBE/DIRBE Band 4
90005

a) 90005 Band 4

COBE/DIRBE Band 5
90005

b) 90005 Band 5

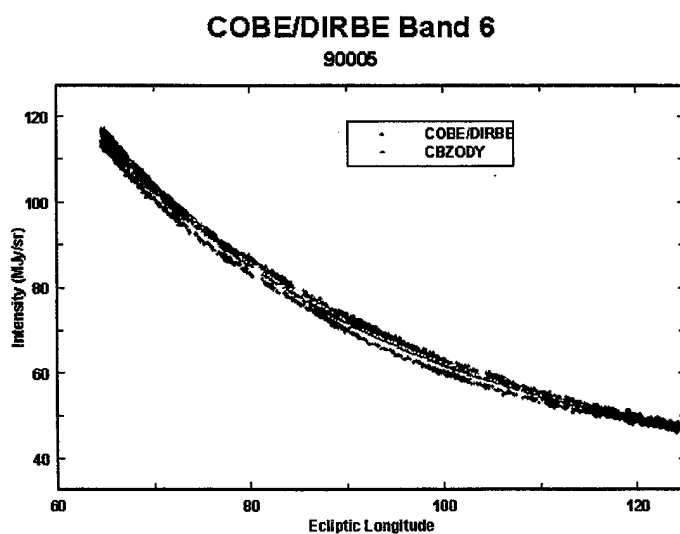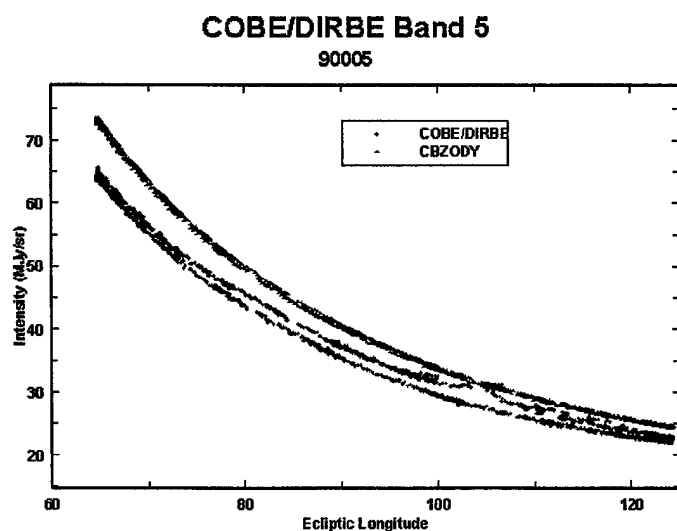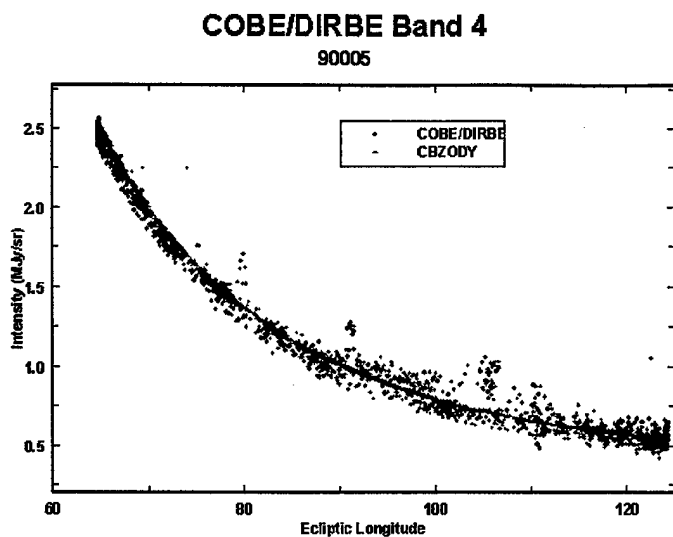## COBE/DIRBE Band 6
90005

c) 90005 Band 6

Figure 61: In-plane fits to the CIO data.

3.12 COBE CIO Psuedo-Scans

Figure 62 shows COBE pseudo-scans of constant elongation similar to IRAS Zodiacal Observation History File pole-to-pole scans. Again, the average parameter set has been used. These data are taken directly from the CIO data. One of the features of the CBZODY6 model is the Lorentzian out of plane density distribution. This feature does not show up well in other data plots.

In the plot, the solid line represents the COBE/DIRBE Band 5 (12μm) data. The dashed line is the CBZODY6 model. The residual is represented by the solid line near an intensity of 0.2 MJy sr^{-1}. The residual has been multiplied by a factor of 10 for clarity.
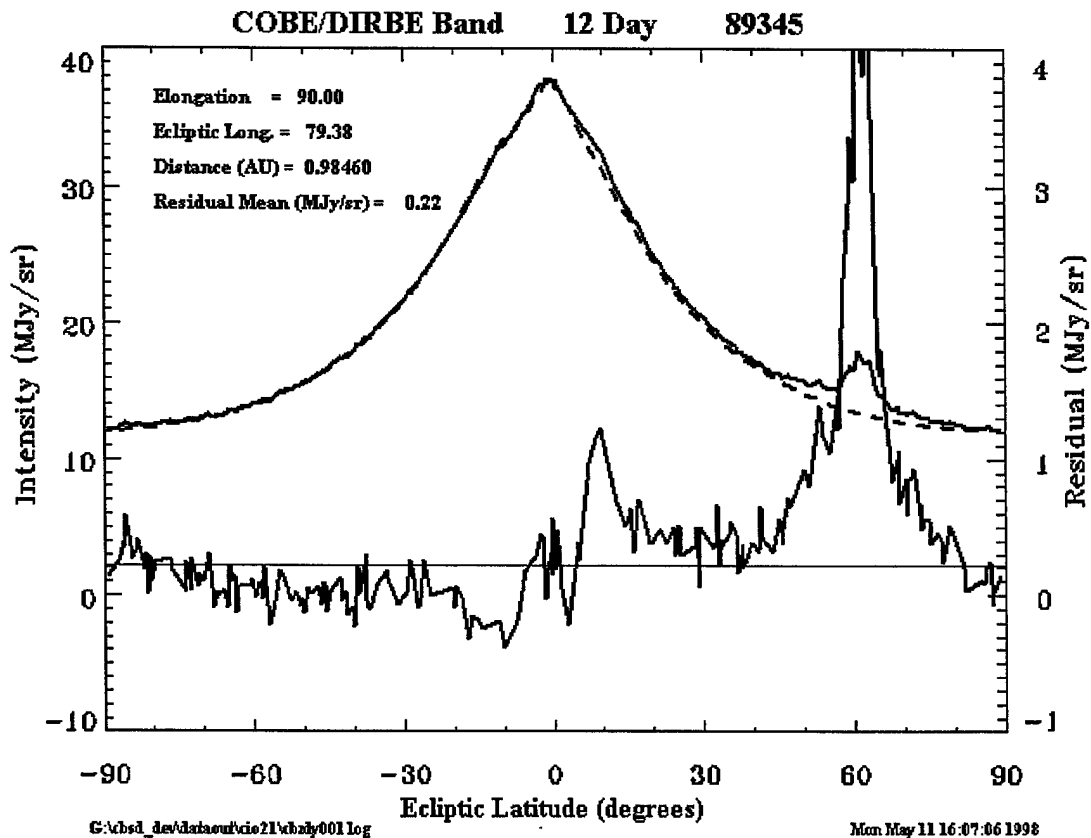

Figure 62: Pole-to-Pole pseudo-scans. Band 5 pole-to-pole pseudo-scans for leading and trailing scans.

70

4. Summary

The Air Force's CBSD code CBZODY6 accurately reproduces the spectrum and spatial (image) data of the zodiacal interplanetary dust cloud from 0.1 to 300μm. Spectral resolutions possible are limited to the spacing of the external volume emissivity database and are available at 0.1 or 0.01μm.

The CBZODY6 model simulations have been compared to IRAS, ZIP, MSX, COBE, and other small rocket and balloon data. The accuracy of the predicted flux can be stated to be within 10%.

There is still work that needs to be done with the CBZODY6 model. The composition of the dust cloud is poorly known. This limits the accuracy of the overall model.

One component of the zodiacal cloud model that has not been tested is the Gegenschein. The Hong (1985) function does have a strong backscatter component. While the Gegenschien has been visually observed and photographed we have not come across any observations that can directly test the CBZODY model. Therefore, backscatter should be tested in future versions of the CBZODY model.

While strides have been made to increase the execution speed of the model, two factors have changed. The speed of the average processor has increased markedly since the beginning of the program. At the same time, the complexity and expectation of the model has increased. Future development of CBZODY6 will have to stress efficiency while maintaining fidelity.

New datasets are being made available. The MSX zodiacal observations are now being made available. NASA's Project Stardust promises to return comet particles of Comet Wild-2 in 2006. The SIRTF mission, scheduled for launch in December 2001, is the next cryogenically cooled space observatory. SIRTF could provide further understanding of the zodiacal cloud such as small structure, time variability, and composition.

References

Beichman, C and Wheelock, S., (1993). *IPAC Newsletter*, Oct 1993.

Bennett, C. L. *et al.*, (1992). *COBE Preprint 92-08*.

Bohren, C.F. and Huffman, D.F. (1983). *Absorption and Scattering of Light by Small Particles*, (New York: Wiley).

Briggs, R. E., (1962). "Symposium: Astrometry I: The Steady-State Space Distribution of Meteoric Particles Under the Operation of the Poynting-Robertson Effect," *Astron, J.*, **67**, 710-723.

Briotta, D. A., J. A. Piper, and J. R. Houck, (1976). *Rocket Infrared Spectroscopy of the Zodiacal Dust Cloud*, AFGL-TR-76-0236 (AD A034 054).

Clark, F. O.; Torbett, M. V.; Jackson, A. A.; Price, S. D.; Kennealy, J. P.; Noah, P. V.; Glaudell, G. A.; Cobb, M, (1993). "The Out-of-Plane Distribution of Zodiacal Dust Near the Earth," *Astron. J.*, **105**, 976.

Cohen, M., (1999). Private communication.

Dermott, S. F., P. D. Nicholson, J. A. Burns, and J. R. Houck. (1984). "Origin of the Solar System Dust Bands Discovered by IRAS," *Nature*, **312**, 505

Dermott, S.F., P. D. Nicholson, J. A. Burns and J. R. Houck. (1985). "Properties and Interaction of Interplanetary Dust," in IAU Colloquium #85, (eds. R. H. Giese and P. Lamy) (D. Reidel Pub. Co.) p395.

Dermott, S.F., P. D. Nicholson, and B. Wolven. (1986). "Preliminary Analysis of the IRAS Solar System Dust Data," in *Asteroids, Comets and Meteors, II* (eds. C-I. Lagerkvist and H. Rickman), Uppsala, p583.

Dermott, S.F. *et al.*, (1994). *Nature*, 369, 719-723.

Duel, E. R. and Walker, *Astron. Astrophys.*, **81**, 207)

Deul, E. R., and Wolstencroft, R. D. (1988). *Astron. Astrophys.*, **196**, 277.

Draine, B. T. and Lee, H. M. (1984), *Ap. J.*, **285**, 89.

Durda, D. D., Dermott,S. F., and Gustafson B. Å. S. (1992). In *Asteroids, Comets and Meteors 1991*, (eds. A.W. Harris and E. Bowell), Flagstaff, p161.

Giese, R. H., and Kneißel, B. (1989). *Icarus*, **81**, 369.

Giese, R. H., Kneißel, B., and Rittich U. (1986). *Icarus*, **68**, 395.

Good, J. (1988). Unpublished IPAC Report.

Gustafson, B. Å. S. (1990), in Fall 1990 IRCB Review Meeting Minutes.

Gray, D. F. (1976). *The Observation and Analysis of Stellar Photospheres* (New York: Wiley).

Hauser, M. G.; Gillett, F. C.; Low, F. J.; Gautier, T. N.; Beichman, C. A.; Aumann, H. H.; Neugebauer, G.; Baud, B.; Boggess, N.; Emerson, J. P. (1984). "IRAS Observations of the Diffuse Infrared Background," *Astrophys. J.*, **278**, L15-L18.

IRAS Catalogs and Atlases, Explanatory Supplement. (1988), ed. C. Beichman, G. Neugebauer, H. J. Habing, P. E. Clegg, and T. J. Chester, (Washington, D.C.: GPO).

Kerker, M. (1969). *The Scattering of Light and other Electromagnetic Radiation*, (New York: Academic Press).

Lamy, P.L., Grün, E., and Perrin, J.M. (1987). *Astron. Astrophys.*, **187**, 767.

Lang, K.R. (1980). *Astrophysical Formulae*, (New York: Springer-Verlag).

Lienert, Ch. (1975). *Space Sci.Rev.*, **18**, 281.

Leinert, Ch., Richter, I., Pitz, E., and Plank, N. (1981). *Astron. Astrophys.*, **103**, 177.

Leiner, C., *et al.* (1998). *Astron. Astrophys. Supp.*, **127**, 1.

Lehmann, H. and W. Häupl (1986). *AAS Photo-Bul.*, **43**, 5.

Lienert, Ch. (1975). *Space Sci.Rev.*, **18**, 281.

Leinert, C. and E. Grün (1990). "Interplanetary Dust, in Physics and Chemistry in Space," in *Space and Solar Physics 20.* (eds. Schwenn R. and Marsch E. eds.) – Springer, Berlin, Heidelberg, p. 207.

Leinert, Ch.; Bowyer, S.; Haikala, L. K.; Hanner, M. S.; Hauser, M. G.; Levasseur-Regourd, A.-Ch.; Mann, I.; Mattila, K.; Reach, W. T.; Schlosser, W.; Staude, H. J.; Toller, G. N.; Weiland, J. L.; Weinberg, J. L.; Witt, A. N. (1998). "The 1997 reference of diffuse night sky brightness," *Astron. Astrophys. Supp.*, **127**, 1.

Low, F. J.; Young, E.; Beintema, D. A.; Gautier, T. N.; Beichman, C. A.; Aumann, H. H.; Gillett, F. C.; Neugebauer, G.; Boggess, N.; Emerson, J. P. (1984). "Infrared Cirrus - New Components of the Extended Infrared Emission," *Astrophys. J.*, **278**, L19-L22.

Meeus, J. (1996). *Astronomical Algorithms*, (William-Bell: Virginia).

Marsch, Physics of the Inner Heliosphere

Murdock, T. L., and Price, S. D. (1985). *Astron. J.*, **90**, 375.

Noah, P. V., "CBSD: The Celestial Background Scene Descriptor, Version 3.0 - Installation and User's Manual", Technical and Scientific Report - Number 3, June 1995

Price, S. D., (1988). *Optical Eng.*, **27**, 75.

Reach, W. T., (1988). "Zodiacal Emission. I - Dust Near the Earth's Orbit," *Astrophys. J.*, **335**, 468.

Reach, W. T., Franz, B. A., Weiland, J. L., Hauser, M. G., Kelsall, T. N., and Rawley, G., (1995). *Nature*, **374**, 521.

Reach, W. T., Franz, B.A., and Weiland, J. L., (1997). *Icarus*, **127**, 461-484.

Reach, W. T.; Abergel, A.; Boulanger, F.; Desert, F.-X.; Perault, M.; Bernard, J.-P.; Blommaert, J.; Cesarsky, C.; Cesarsky, D.; Metcalfe, L.; Puget, J.-L.; Sibille, F.; Vigroux, L. (1996), "Mid-Infrared Spectrum of the Zodiacal Light," *Astron. Astrophys.*, **315**, L381-L384.

Röser, S. and Staude, H.J. (1978). *Astron. Astrophys.*, **67**, 381.

Rowan-Robinson, M., Hughes, J., Vedi, K., and Walker, D. W. (1990), *M.N.R.A.S.* **11**, 1.

Schmude, R. W. Jr. (1999). "Photoelectric Magnitude Measurements of the Zodiacal Light," *IAPPP Communications*, **75**, 24.

Sykes, M. V. (1988). "IRAS Observations of Extended Zodiacal Structures," *Astrophys. J.*, **334**, L55.

Sykes, M. V. (1990). "Zodiacal Dust Bands - Their Relation to Asteroid Families," *Icarus*, **85**, 267.

Sykes, M. V., Greenberg, R., Dermott, S. F., Nicholson, P. D., Burns, J. A., and Gautier, T. N. (1989). "Dust Bands in the Asteroid Belt," in *Asteroids II*, eds. R. P. Binzel, T. Gehrels, and M. S. Matthews, (Tucson: U. of Arizona), p.336.

Wiscombe, W.J. (1980). *Appl. Optics*, **19**, 1505.

Wright, E. L., (1992) *COBE Preprint 92-12*.

van de Hulst, H. C. (1957), *Light Scattering by Small Particles* (New York: Wiley).